Abundance and Mixing State of Black Carbon across Atlantic Coastal and Remote Marine Surface Atmospheres

Dissertation zur Erlangung des Grades

‘Doktor rerum naturalium (Dr. rer. nat.)’

im Promotionsfach Chemie

am Fachbereich Chemie, Pharmazie, Geographie und Geowissenschaften

der Johannes Gutenberg-Universität in Mainz

Xihao Pan

geb. in Sichuan, China

Mainz, 2025

License

1. Berichterstatter: Prof. Dr. Ulrich Pöschl

2. Berichterstatter: Prof. Dr. Thorsten Hoffmann

Tag der mündlichen Prüfung: 11.12.2025

Declaration

I hereby declare that I wrote the dissertation submitted without any unauthorized external assistance and used only sources acknowledged in the work. All textual passages which are appropriated verbatim or paraphrased from published and unpublished texts as well as all information obtained from oral sources are duly indicated and listed in accordance with bibliographical rules. In carrying out this research, I complied with the rules of standard scientific practice as formulated in the statutes of Johannes Gutenberg University Mainz to insure standard scientific practice.

Xihao Pan

Mainz, 2025

Abstract

Black carbon (BC) is a strong absorber of solar radiation and a major contributor to climate warming. It is mainly produced by the incomplete combustion of fossil fuels, biofuels, and biomass. In the atmosphere, BC undergoes aging through condensation, coagulation, and multiphase reactions, during which it becomes coated with other aerosol components. These aging processes substantially enhance BC's light absorption and hygroscopicity, thereby influencing its direct radiative forcing and aerosol-cloud interactions. However, large uncertainties remain in assessing the climatic impacts of BC mixing state. A key reason is the limited understanding of BC mixing characteristics under real atmospheric conditions. Most existing studies have focused on continental environments, particularly near-surface observations. However, the diversity of BC mixing states across different environments poses challenges for constraining global models. For global climate models, observations of BC loading and mixing state over marine regions are especially important for characterizing remote environments and representing global averages. Nevertheless, available measurements over oceans remain scarce, particularly those concerning BC mixing state. As a result, our understanding of how the marine environment influences BC aging and mixing state remains very limited.

This thesis focuses on shipborne measurements of BC mass concentrations and mixing state over the Atlantic Ocean, conducted using a Single Particle Soot Photometer (SP2) aboard the research sailing yacht S/Y Eugen Seibold. The study investigates the key factors influencing BC loading and mixing state in marine environments. Based on an improved method for BC mixing-state retrieval, this work elucidates the aging processes through which freshly emitted BC externally attached to non-BC aerosols (e.g., sea salt) evolves into thickly coated BC during transport in humid marine atmospheres.

In Chapter 2, to enable rapid and scalable analysis of SP2 datasets collected in marine environments, the SP2 Parallel Accelerated Runtime Kit (SPARK) is developed in this thesis. It is a cross-platform toolkit designed for efficient and accurate analysis of large SP2 datasets. SPARK enhances data accuracy through improved numerical algorithms and ensures long-term data stability by automatically detecting and correcting instrument drifts such as laser misalignment, baseline shifts, and timing variations. Its parallel computing capabilities greatly accelerate data processing, allowing routine analysis of extensive campaign datasets. Moreover, its standardized and physically consistent retrievals of optical sizing and coating properties provide the analytical foundation for all subsequent chapters, ensuring consistent and high-precision characterization of BC mass, size, and mixing state across the Atlantic shipborne measurements.

In Chapter 3, this study examines the transformation of freshly emitted BC particles in marine atmospheres, which tend to attach to marine aerosols and subsequently form thickly coated core-shell structures under high relative humidity. Based on in-situ measurements from ten Atlantic Ocean cruises aboard the S/Y Eugen Seibold, this study compiled a comprehensive dataset (over 1120 hours of observations) of BC concentrations and mixing states across both

near-coastal and remote regions (10° N-60° N, 10° E-65° W). The results show that the background BC concentration over the Atlantic Ocean is approximately 100 ng m^{-3}, indicating a well-mixed marine atmosphere extending up to ~1000 km offshore. Non-core-shell BC particles dominate (>50%) in coastal regions, likely due to coagulation with marine aerosols. High humidity (>85%) further transforms BC associated with marine aerosols into thickly coated core-shell particles via hygroscopic growth. These findings provide new insights into BC behavior and transformation processes in marine environments.

In Chapter 4, this study reveals that regional transport in marine environments can produce highly aged BC particles with coating thicknesses of several hundred nanometers. In this work, shipborne measurements from seven cruises (over 660 hours of observations) conducted between June and August 2020 across the Northeast Atlantic (35-66° N, 30° W-10° E) were classified into two groups according to air mass origin: continental-dominated and marine-dominated. Comparisons between these two groups reveal that air masses originating from continental Europe increased BC loadings in the Atlantic marine atmosphere by tens to hundreds of ng cm^{-3}. Marine air masses, in contrast, favored the formation of aged BC with larger cores and thicker coatings, often reaching 100-200 nm. For BC particles emitted from Europe, coating growth in continental environments typically ranges from only a few to tens of nanometers (Laborde et al., 2013). Our observations demonstrate that BC transported through marine environments can reach highly aging levels, likely due to coagulation with marine aerosols (e.g., sea salt) and droplet formation at high humidity. This is consistent with the mechanisms proposed in Chapter 3. Our findings highlight the crucial role of marine environments in enhancing BC aging during regional transport and promoting the formation of thickly coated particles, which have important implications for the global climate system.

In summary, this thesis provides new insights into BC aging processes in the marine atmosphere and their implications for improving climate model representations of aerosol-radiation interactions. It addresses the current knowledge gap regarding how marine conditions shape BC mixing state, which is a key factor controlling its climate impact. Our results demonstrate that BC aging and mixing in marine environments are strongly influenced by coagulation with marine aerosols and high humidity, rather than solely by local emissions or condensation. These findings reveal previously unquantified marine pathways that would enhance BC light absorption and aerosol-cloud interactions. Ultimately, this thesis provides crucial observational evidence to inform and constrain the parameterization of BC mixing state and its associated radiative and microphysical effects in marine regions, thereby improving future climate modeling and predictions of BC's role in global climate change.

Zusammenfassung

Schwarzer Kohlenstoff (Black Carbon, BC) ist ein starker Absorber der solaren Strahlung und ein bedeutender Treiber der Klimaerwärmung. Er entsteht hauptsächlich bei der unvollständigen Verbrennung fossiler Brennstoffe, Biokraftstoffe und Biomasse. In der Atmosphäre altert BC durch Kondensation, Koagulation und Mehrphasenreaktionen, wobei er mit anderen Aerosolkomponenten beschichtet wird. Diese Alterungsprozesse verstärken BCs Lichtabsorption und Hygroskopizität erheblich und beeinflussen damit seinen direkten Strahlungsantrieb sowie Aerosol-Wolken-Wechselwirkungen. Die klimatischen Auswirkungen des BC-Mischungszustands sind jedoch mit großen Unsicherheiten behaftet. Ein wesentlicher Grund ist das begrenzte Verständnis der BC-Mischungseigenschaften unter realen atmosphärischen Bedingungen. Die meisten bisherigen Studien konzentrieren sich auf kontinentale Umgebungen, insbesondere auf bodennahe Beobachtungen. Die Vielfalt der BC-Mischungszustände in unterschiedlichen Umgebungen erschwert jedoch die Parametrisierung und Validierung globaler Klimamodelle. Für globale Klimamodelle sind Beobachtungen der BC-Beladung und des Mischungszustands über maritimen Regionen besonders wichtig, um abgelegene Umgebungen zu charakterisieren und globale Mittelwerte abzubilden. Dennoch sind verfügbare Messungen über den Ozeanen selten, insbesondere solche zum BC-Mischungszustand. Folglich ist unser Verständnis darüber, wie die maritime Umgebung die BC-Alterung und den Mischungszustand beeinflusst, sehr begrenzt.

Diese Dissertation konzentriert sich auf schiffsgestützte Messungen der BC-Massenkonzentrationen und des Mischungszustands über dem Atlantik, durchgeführt mit einem Single Particle Soot Photometer (SP2) an Bord der Forschungssegelyacht S/Y Eugen Seibold. Die Studie untersucht die Schlüsselfaktoren, die BC-Beladung und den Mischungszustand in maritimen Umgebungen beeinflussen. Auf Basis einer verbesserten Methode zur Bestimmung des BC-Mischungszustands beschreibt diese Arbeit die Alterungsprozesse, durch die frisch emittierter BC, der äußerlich an nicht-BC-Aerosole (z. B. Meersalz) angelagert ist, während des Transports in feuchten maritimen Atmosphären zu stark beschichtetem BC wird.

In Kapitel 2 wird zur schnellen und skalierbaren Analyse von in maritimen Umgebungen erhobenen SP2-Datensätzen das SP2 Parallel Accelerated Runtime Kit (SPARK) entwickelt. Es handelt sich um ein plattformübergreifendes Toolkit zur effizienten und genauen Analyse großer SP2-Datensätze. SPARK erhöht die Datenqualität durch verbesserte numerische Algorithmen und gewährleistet die langfristige Stabilität der Daten, indem Instrumentdrifts wie Laser-Fehljustierungen, Basislinienverschiebungen und zeitliche Versätze automatisch erkannt und korrigiert werden. Die Parallelisierung beschleunigt die Datenverarbeitung erheblich und ermöglicht die routinemäßige Analyse umfangreicher Kampagnendatensätze. Darüber hinaus bilden standardisierte und physikalisch konsistente Retrieval-Verfahren zur optischen Größenbestimmung und zu Beschichtungseigenschaften die analytische Grundlage für alle folgenden Kapitel und gewährleisten eine konsistente, hochpräzise Charakterisierung von BC-Masse, -Größe und -Mischungszustand über die schiffsgestützten Atlantikmessungen hinweg.

In Kapitel 3 untersucht diese Studie die Transformation frisch emittierter BC-Partikel in maritimen Atmosphären, die dazu neigen, sich an marine Aerosole anzulagern und anschließend bei hoher relativer Luftfeuchte stark beschichtete Kern-Schale-Strukturen (core-shell) zu bilden. Basierend auf In-situ-Messungen während zehn Atlantikfahrten an Bord der S/Y Eugen Seibold wurde ein umfassender Datensatz (über 1120 Beobachtungsstunden) der BC-Konzentrationen und Mischungszustände in sowohl küstennahen als auch abgelegenen Regionen (10° N–60° N, 10° E–65° W) zusammengestellt. Die Ergebnisse zeigen, dass die Hintergrund-BC-Konzentration über dem Atlantik ungefähr 100 ng m^{-3} beträgt, was auf eine gut durchmischte maritime Atmosphäre hinweist, die sich bis etwa 1000 km von der Küste entfernt erstreckt. BC-Partikel ohne Kern-Schale-Struktur überwiegen (>50 %) in Küstenregionen, wahrscheinlich aufgrund der Koagulation mit marinen Aerosolen. Hohe relative Luftfeuchte (>85 %) transformiert BC, das mit marinen Aerosolen assoziiert ist, durch hygroskopisches Wachstum weiter zu stark beschichteten Kern-Schale-Partikeln. Diese Befunde liefern neue Einblicke in das Verhalten und die Transformationsprozesse von BC in maritimen Umgebungen.

In Kapitel 4 zeigt diese Studie, dass regionaler Transport in maritimen Umgebungen stark gealterte BC-Partikel mit Beschichtungsdicken von mehreren hundert Nanometern hervorbringen kann. In dieser Arbeit wurden schiffsgestützte Messungen von sieben Fahrten (über 660 Beobachtungsstunden), die zwischen Juni und August 2020 über dem Nordostatlantik (35–66° N, 30° W–10° E) durchgeführt wurden, nach der Luftmassenherkunft in zwei Gruppen eingeteilt: kontinental bzw. maritim dominierte Gruppen. Vergleiche zwischen diesen beiden Gruppen zeigen, dass aus dem kontinentalen Europa stammende Luftmassen die BC-Beladung in der marinen Atmosphäre des Atlantiks um Dutzende bis Hunderte ng cm^{-3} erhöhten. Maritime Luftmassen förderten dagegen die Bildung gealterten BCs mit größeren Kernen und dickeren Beschichtungen, die häufig 100–200 nm erreichen. Für aus Europa emittierte BC-Partikel liegt das Beschichtungswachstum in kontinentalen Umgebungen typischerweise nur im Bereich von wenigen bis einigen Dutzend Nanometern (Laborde et al., 2013). Unsere Beobachtungen zeigen, dass BC, der durch maritime Umgebungen transportiert wird, ein sehr hohes Alterungsniveau erreichen kann, wahrscheinlich aufgrund von Koagulation mit marinen Aerosolen (z. B. Meersalz) und Tropfenbildung bei hoher Feuchte. Dies stimmt mit den in Kapitel 3 vorgeschlagenen Mechanismen überein. Unsere Ergebnisse unterstreichen die entscheidende Rolle maritimer Umgebungen bei der Verstärkung der BC-Alterung während des regionalen Transports und der Förderung der Bildung stark beschichteter Partikel, die wichtige Implikationen für das globale Klimasystem haben.

Zusammenfassend liefert diese Dissertation neue Einblicke in die BC-Alterungsprozesse in der maritimen Atmosphäre und deren Bedeutung für die Verbesserung der Darstellung von Aerosol-Strahlungs-Wechselwirkungen in Klimamodellen. Sie adressiert die bestehende Wissenslücke darüber, wie maritime Bedingungen den BC-Mischungszustand prägen, der ein Schlüsselfaktor für seine Klimaauswirkungen ist. Unsere Ergebnisse zeigen, dass BC-Alterung und -Mischung in maritimen Umgebungen stark durch Koagulation mit marinen Aerosolen und hohe Feuchte beeinflusst werden und nicht ausschließlich durch lokale Emissionen oder Kondensation. Diese Befunde offenbaren bislang nicht quantifizierte maritime Pfade, die die Lichtabsorption von BC und Aerosol-Wolken-Wechselwirkungen verstärken können. Letztlich liefert diese Dissertation

entscheidende beobachtungsbasierte Evidenz, die die Parametrisierung des BC-Mischungszustands und seiner damit verbundenen strahlungs- und mikrophysikalischen Effekte in marinen Regionen informiert und verbessert und dadurch die zukünftige Klimamodellierung sowie Vorhersagen zur Rolle von BC im globalen Klimawandel verbessert.

Contents

Chapter 1 Introduction

1.1 Black Carbon: definition, properties, and climate effects

1.1.1 Definition and terminology

Atmospheric aerosols are solid or liquid particles suspended in the atmosphere, ranging from a few nanometers to tens of micrometers in diameter. These particles influence climate through various mechanisms. Most aerosols cool the atmosphere, but black carbon (BC) warms it. Among atmospheric aerosols, BC occupies a unique position as the strongest light-absorbing component (IPCC, 2013; IPCC, 2021). BC also reduces visibility, degrades air quality, and impacts human health (Ni et al., 2024; Seinfeld and Pandis, 2006).

BC aerosol is defined based on four key physical properties: (1) high light absorption efficiency per unit mass, with a mass absorption cross section exceeding 5 $m^2 g^{-1}$ at 550 nm; (2) refractory nature, with vaporization temperature near 4000 K; (3) insolubility in water and organic solvents, and (4) aggregate morphology composed of small carbon spherules (Bond and Bergstrom, 2006). This combination distinguishes BC from other atmospheric carbonaceous particles.

Different techniques use distinct operational terminology to define 'light-absorbing carbonaceous' that are similar to BC (Petzold et al., 2013; Pöschl, 2005). The term soot is similar to BC but it generally refers to particles originating from the incomplete combustion of hydrocarbon fuels, describing their source mechanism (Petzold et al., 2013). Thermal-optical analysis separates elemental carbon (EC) from organic carbon (OC) through stepwise heating protocols (Cavalli et al., 2010; Chow et al., 2007), while optical methods quantify equivalent black carbon based on assumed mass absorption cross-sections (Petzold et al., 2013). Brown carbon (BrC) exhibits stronger absorption in the ultraviolet and blue wavelengths compared to BC's relatively uniform absorption across the visible spectrum (Andreae and Gelencsér, 2006; Laskin et al., 2015). Refractory black carbon (rBC) is defined by its ability to maintain structural integrity up to ~4000 K. It can be distinguished and quantified using the laser-induced incandescence (LII) method (Melton, 1984; Schwarz et al., 2006; Stephens et al., 2003).

BC forms when combustion lacks sufficient oxygen for complete conversion to CO_2. Carbon-rich precursors (e.g., acetylene, C_2H_2; polycyclic aromatic hydrocarbons, PAHs) nucleate into molecular clusters of 1-2 nm, which collide and fuse into chain-like aggregates within milliseconds (Bond and Bergstrom, 2006; Petzold et al., 2013). At combustion temperatures exceeding 1500°C, thermal annealing transforms these aggregates into ordered sp^2-bonded carbon structures (Andreae and Gelencsér, 2006). This sp^2-hybridized, graphene-like carbon structure gives BC a strong capacity to absorb visible and near-infrared light - its delocalized π-electrons make BC a highly efficient light absorber in the atmosphere (Bond et al., 2013; Jacobson, 2001; Liu et al., 2020; Ramanathan and Carmichael, 2008).

Once emitted, BC undergoes an atmospheric life cycle that includes near-source mixing, boundary-layer export and convective lofting, chemical and physical aging (coating growth and

restructuring), and eventual removal by wet and dry deposition (Bond et al., 2013). Most ambient BC resides in the aerosol accumulation mode, where lifetimes are long and health relevance is high (Janssen et al., 2011; Kirrane et al., 2019). Typical residence times in the troposphere are several days to about a week, but can extend to weeks or longer when BC is lofted into the free troposphere or lower stratosphere, where scavenging is less efficient (Samset et al., 2014; Schwarz et al., 2017). This persistence, coupled with strong absorption, underlies BC's role as a potent climate-warming agent. These foundations set up how BC perturbs climate through radiative forcing pathways (section 1.1.2) and specifically focuses on mixing state as the microphysical link between aging, optics, and removal (section 1.2).

1.1.2 BC climate effects

Aerosols influence climate through aerosol-radiation interactions (ARI) and aerosol-cloud interactions (ACI) (IPCC, 2021). ARI covers direct radiative interactions and rapid atmospheric adjustments (e.g., temperature profiles, stability changes); ACI captures aerosol effects on cloud microphysics. BC contributes to both (schematized in Fig. 1.1): aged/coated BC can act as cloud condensation nuclei (CCN), potentially increasing droplet number and cloud albedo (Bond et al., 2013; Cappa et al., 2012), while semi-direct effects arise when absorption-driven heating reduces cloudiness by stabilizing the column, evaporating droplets, or altering temperature profiles (Koch and Genio, 2010; Li et al., 2022). Due to BC's strong light-absorption capacity, its direct radiative impacts tend to dominate its net climate effect while quantifying its climate forcing is challenging and remains highly uncertain. The IPCC Fifth Assessment Report (2013) estimated the global BC direct radiative forcing (DRF) (1750–2011) at roughly +0.40 W m^{-2} (with a range of about +0.05 to +0.80 W m^{-2}). Bond et al. (2013) estimated a +0.71 W m^{-2} (range +0.08 to +1.27 W m^{-2}) for industrial-era BC direct forcing. A useful approximation for BC DRF is (Schulz et al., 2006b):

$$DRF_{BC} = \mathrm{E} \times \mathrm{L} \times \mathrm{AFE} \times \mathrm{MAC_{BC}} \tag{1.1}$$

where E [g m^{-2} s^{-1}] is the global BC emission rates, L [s] is the atmospheric lifetime of BC, $\mathrm{MAC_{BC}}$ [m^2 g^{-1}] is the mass absorption cross-section, AFE [W m^{-2} AAOD^{-1}] is the absorption forcing efficiency (Liu et al., 2020; Schulz et al., 2006b). The product $\mathrm{E} \times L \times \mathrm{MAC_{BC}}$ yields BC absorption aerosol optical depth (AAOD), which is measurable through ground-based sun photometers, satellite retrievals, and aircraft-based measurements (Dubovik and King, 2000; Holben et al., 2001).

Inventory uncertainty arises from emission factors, activity data, and source mix, therefor affect the E. Global BC emissions from bottom-up inventories are estimated at 7.5 Tg yr^{-1} with large uncertainties (2-29 Tg yr^{-1}) (Bond et al., 2013; Klimont et al., 2017; Wang et al., 2014b). Open biomass burning, episodic fire seasons can raise E sharply on regional scales, for example, the 2017 Pacific Northwest wildfires lofted ~0.1–0.3 Tg total aerosol (BC ~2–3%) directly into the stratosphere (Khaykin et al., 2020; Peterson et al., 2018; Torres et al., 2020).

After emission, transport and vertical placement control both the lifetime L and the absorption forcing efficiency AFE. Long-range transport can carry BC across ocean or continentals (e.g., biomass burning smoke from Asia to North America and from African to South America) (Hadley et al., 2007; Holanda et al., 2020). Deep convection such as pyro-convection can rapidly inject BC into the upper troposphere and episodically the lower stratosphere (Ditas et al., 2018; Ma et al., 2024; Peterson et al., 2018; Yu et al., 2019). At such altitudes, BC residence can extend from days to months, and per-mass forcing efficiency AFE can be ~5–10 times higher than near the surface (Samset and Myhre, 2011).

Wet scavenging dominates the global sink through activation into as CCN or ice-nucleating particles (INP) and subsequent rainout or washout. Dry deposition via gravitational settling is relatively more important in low-precipitation regions (deserts, polar areas). Once deposited on snow and ice, BC darkens the surface and produces a distinct, regionally important positive forcing separate from its atmospheric effects (Bond et al., 2013).

The mass absorption cross-section MAC_{BC} links microphysics to optics and is governed primarily by the aging that occurs during transport. Condensation and coagulation add inorganic and organic material to BC cores, and humidity cycling can restructure aggregates via capillary forces (Pagels et al., 2009; Zhang et al., 2008); together these processes alter refractive-index contrast and morphology in ways that can either enhance or moderate bulk absorption. Uncertainty in this optical term projects linearly into absorption and hence into forcing. The term mixing state—the degree to which BC exists as externally mixed bare aggregates or internally mixed, coated particles—as the summary descriptor of this evolution; its detailed treatment, including quantitative ranges and measurement approaches, is deferred to section 1.2 (Adachi et al., 2010; Bond et al., 2013; Cappa et al., 2012; China et al., 2013).

In summary, uncertainties in BC forcing estimation arise from its atmospheric lifecycle. Section 1.2 will therefore introduce BC's mixing state and its climatic relevance, as it is a key to bridging the gap between BC's micro-scale processes and macro-scale climate forcing.

1.2 Mixing state of black carbon

The mixing state describes how BC and non-BC species are distributed within individual particles and across the particle population (Riemer et al., 2019). Within a particle, BC may be bare or partially to fully coated; morphologies include near core-shell, patchy or offset coatings, or multiple small BC inclusions embedded in non-BC material (Adachi and Buseck, 2008). Across the population, composition spans externally mixed (nearly pure BC) through thinly and thickly coated BC to BC-free particles (Bond et al., 2013). The amount of coating (by coating thickness, absolute shell thickness or the shell-to-core diameter ratio) is often used to quantify the mixing state. At the population level, distributions of coating thickness capture the heterogeneity of BC mixing and indicate how BC interacts with radiation and clouds, since optical and microphysical responses emerge from particle-scale diversity (Fierce et al., 2020; Lack and Cappa, 2010).

1.2.1 Pathways to internal mixing: aging

Freshly emitted BC is typically externally mixed, hydrophobic, and highly fractal agglomerates of nanometer-scale spherules. With atmospheric processing, BC transitions from bare aggregates to partially and then thickly coated particles—often with progressive structural compaction (Fig. 1.1). This evolving mixing state controls how BC interacts with radiation and clouds and, ultimately, its atmospheric residence time (Adachi and Buseck, 2008; Bond and Bergstrom, 2006; Petzold et al., 2013).

Three broad, frequently discussed pathways can drive the transition toward internal mixing, with efficiencies that vary by environment and particle size (Riemer et al., 2019; Seinfeld and Pandis, 2006). (1) Condensation/partitioning: oxidation of SO_2/NO_x/VOCs and multiphase chemistry supply sulfate, nitrate, and secondary organics that condense onto BC; this pathway strengthens with higher precursor abundance and oxidant levels, is accelerated at high RH via aqueous uptake, and is temperature-sensitive (cooler air favors partitioning of semi-volatile nitrate and some organics) (Pagels et al., 2009; Seinfeld and Pandis, 2006; Zhang et al., 2008). (2) Coagulation/attachment: collisions with pre-existing particles (e.g., inorganics, organics, sea salt) embed BC within mixed particles or attach BC at their surfaces; this pathway intensifies at high number concentrations, under turbulence, and for smaller BC cores, which diffuse and collide more efficiently (Riemer et al., 2019; Seinfeld and Pandis, 2006). (3) Restructuring by humidity and heat: repeated humidification–evaporation and cloud processing generate capillary forces that compact aggregates and redistribute inclusions toward more optically coupled arrangements; mild thermal histories can further densify structures. Timescales depend on mechanism and environment. In photochemically active, polluted boundary layers—and/or at high RH where aqueous uptake and cloud cycling are frequent—condensation-dominated aging proceeds within hours, whereas in cleaner or remote air where coagulation and intermittent cloud processing dominate, aging can take multiple days (Peng et al., 2016; Riemer et al., 2019; Seinfeld and Pandis, 2006).

As coatings accumulate and compositions become more hygroscopic, BC-containing particles tend to activate at lower supersaturation. This activation enhances their entry into cloud cycles and increases wet scavenging, and this generally shortens atmospheric lifetime. Under typical cloud supersaturations (~0.1-1%), accumulation-mode particles (~0.1–0.3 μm) are most likely to activate because only modest growth/coating is needed to cross CCN thresholds for such size ranges (Bond et al., 2013; Petters and Kreidenweis, 2007). Nucleation scavenging is selective: larger and/or more thickly coated BC-containing particles are preferentially removed, while small BC cores are efficiently removed when embedded in larger hygroscopic hosts formed via coagulation (Bond et al., 2013; Riemer et al., 2019).

1.2.2 BC mixing state and coating “lensing”

Coatings on BC cores can amplify light absorption via the “lensing effect”: a relatively transparent shell focuses light into the absorbing core and, together with aggregate

compaction, increases the MAC_{BC} (Bond et al., 2013; Fuller et al., 1999; Lack and Cappa, 2010). In the context of section 1.1, a larger MAC_{BC} increases the ARI warming by BC. The absorption enhancement of (E_{abs}) increases with coating thickness up to a moderate shell-to-core ratio (assuming spheric shape). Lensing effect is stronger for non-absorbing coatings (e.g., sulfate, most secondary organics) and is weaken when coatings are light-absorbing (brown carbon) or when aggregates remain highly porous (Fierce et al., 2020; Lack and Cappa, 2010). Consequently, the same average coating mass can yield different MAC_{BC} depending on how coating distributions map onto morphology and composition, and on the humidity history that drives compaction (Bond et al., 2013; Riemer et al., 2019).

There is ongoing debate about the magnitude and ubiquity of absorption enhancement. Cappa et al. (2012) found small ensemble-average E_{abs} enhancements in California outflow despite substantial coatings and showed that idealized core-shell assumptions can overpredict lensing for realistic particle populations. Subsequent works reached similar conclusions (small E_{abs}) and explicitly highlighted the sensitivity to mixing-state heterogeneity (Cappa et al., 2019). Other studies, especially in polluted, rapidly aging plumes, report larger absorption enhancement consistent with thicker coatings and partial compaction, whereas regional outflow and free-tropospheric observations often show moderate values—smaller than many model or chamber simulations (Cappa et al., 2019; Peng et al., 2016; Zhang et al., 2018a). Taken together, the literature indicates that enhancement depends on environmental conditions and source/aging regime: rapid condensation in urban haze can drive large E_{abs}, while diluted outflow and the free troposphere more often exhibit modest values (Liu et al., 2017; Zhang et al., 2023).

In polluted boundary layers, condensable vapors can form thick coatings within hours. However, dilution, boundary-layer dynamics, and variability in core size limit the generalizability of these conditions. As air is transported to regional outflow and the free troposphere, repeated humidification and cloud cycling compress carbon aggregates. Simultaneously, wet removal preferentially depletes the thickest-coated, most CCN-active particles (Bhandari et al., 2019; Zhang et al., 2008). Consequently, the ensemble-mean E_{abs} remains small to moderate, even when measurable coatings are present. Models that assume uniform core-shell particles may overestimate enhancement, while representing distributions of shell-to-core ratios and morphologies aligns predictions more closely with field constraints (He et al., 2015; Wang et al., 2023a; Zhang et al., 2016).

Overall, the relationships between enhancement and mixing state depend jointly on where BC ages and how it is observed and modeled. Section 1.2.3 examines the spatial heterogeneity of mixing state and the measurement limits that shape reported coating–enhancement relationships—motivating paired near-source and remote-ocean observations for forcing-relevant constraints.

1.2.3 Spatial variability of BC mixing state and its forcing implications

The mixing state varies systematically with proximity to sources, chemical environment, and meteorology: near combustion sources BC is often externally mixed or only thinly coated, limited time for condensation and cloud processing and with frequent hetero-coagulation / attachment in high-number environments. With transport and photochemical processing, condensation of sulfate/nitrate/secondary organics and humidity-driven restructuring move the population toward internally mixed states, while size-dependent wet removal selectively depletes the thickest-coated, most CCN-active particles (Buffaloe et al., 2014; Cappa et al., 2014; Cheng et al., 2012; Subramanian et al., 2010; Taketani et al., 2016; Zanatta et al., 2018). These patterns are observed across urban, outflow, and marine/remote environments and are consistent with field constraints on vertical profiles and aging rates. Spatial heterogeneity in BC mixing state maps directly onto the terms in the DRF estimates: coatings and morphology regulate MAC_{BC} via lensing (and thus E_{abs}); increased hygroscopicity/CCN activity shortens BC lifetime in humid, cloudy boundary layers via selective wet removal; and vertical placement during transport (e.g., export/lofting) raises AFE aloft so that smaller masses can exert outsized radiative influence (Bond et al., 2013).

Close-to-source measurements (roadside and stack/ship-exhaust transects, urban supersites, and aircraft plume intercepts) constrain the initial conditions for aging—source-resolved core-size distributions and early condensation/coagulation rates. Remote environment measurements at remote environments, by contrast, constrain the contribution of aging, transport, providing forcing-relevant closure along the source-to-sink pathway. For example, remote ocean provides globally relevant constraints on BC mixing state and its climate effect. Because oceans cover ~70% of Earth's surface, the marine boundary layer is comparatively quasi-uniform, repeatable, and meteorologically well characterized relative to continental boundary layers; it is also far from direct emission sources. As continental outflow transitions to remote marine air, BC experiences multi-day photochemical processing and repeated humidity/cloud cycles that promote coating growth and aggregate compaction, while selective scavenging removes the most CCN-active, thickly coated particles. This natural evolution—from near-source to regional outflow to remote marine—distills the coupled effects of aging, wet removal, and transport that control population-mean MAC_{BC} and E_{abs}, and thus the AAOD term in section 1.1.2 (Bond et al., 2013).

1.3 Black Carbon Measurement: Evolution, Applications, and Challenges

The climate effects and uncertainties discussed in Section 1.2 highlight the need for accurate, comprehensive BC measurements to constrain forcing estimates. As noted earlier in section 1.1, each measurement method defines 'black carbon' in its own operational way, depending on whether it measures carbon content, light absorption. Thus, BC measurement techniques have evolved from bulk analyses to optical and single-particle methods to capture different aspects of BC (Petzold et al., 2013).

1.3.1 Historical development of BC measurement techniques

BC has been quantified by bulk carbon analyses and by optical measurements that infer mass from absorption. Thermal-optical analysis emerged as a primary technique for quantifying carbonaceous aerosols in the 1980s-1990s. This analysis separates organic carbon (OC) from elemental carbon (EC) through stepped heating in controlled atmospheres (Cavalli et al., 2010; Chow et al., 2007). While thermal-optical analysis became standard, it suffers from method-dependent EC/OC splits and cannot resolve mixing state. Filter-based optical methods developed concurrently, defining BC through its light-absorbing properties. Instruments like the Aethalometer, Particle Soot Absorption Photometer (PSAP), and Multi-Angle Absorption Photometer (MAAP) quantify absorption by drawing aerosol-laden air through a filter and measuring the resulting light attenuation (Coen et al., 2010). Volatility tandem DMAs (V-TDMAs) can infer aerosol mixing state from size-resolved shrinkage during heating, but because the refractory residue after heating includes BC together with other non-volatile material, a V-TDMA alone cannot chemically distinguish BC from non-BC components (Zhang et al., 2016, 2023). These techniques suffer from artifacts related to filter loading effects, scattering corrections, and interference from other absorbing species (Lack et al., 2014).

Despite extensive deployment, these techniques share fundamental limitations. They cannot resolve particle-level heterogeneity controlling optical properties, mixing state distributions determining hygroscopicity, or morphological variations affecting absorption enhancement (Petzold et al., 2013). Climate models require these microscale properties to reduce forcing uncertainties. As demonstrated in Section 1.2, these particle-level properties - especially mixing state and distribution - drive much of the uncertainty in estimates of BC's climate forcing.

1.3.2 The Single Particle Soot Photometer: principle, validation and application

The Single Particle Soot Photometer (SP2) quantifies individual BC particles using LII (Stephens et al., 2003). It employs a continuous-wave 1064 nm Nd:YAG laser to heat particles to incandescence (~4000 K), which allows direct measurement of refractory BC mass. Simultaneously, the instrument infers particle size (assuming a BC density) and determines each particle's coating thickness and mixing state. A detailed technical introduction and the data processing methodology to the SP2 is provided in Chapter 2.

Key technical developments and validations expanded SP2 capabilities over the past decades. Moteki & Kondo (2007) introduced the "lag-time" analysis, which examines the delay between the scattering peak and the incandescence peak. This delay allows classification of individual BC particles as either bare/thinly coated (short lag) or thickly coated (long lag), essentially a binary indicator of single-particle mixing state. Sedlacek et al. (2012) used this lag-time approach to identify "non-core-shell" BC morphologies, where the BC core attaches to the particle surface rather than being fully encapsulated in the center. These cases are indicated by a negative lag-time in the SP2 signal. Such particles have distinct optical properties that may not be captured by traditional core-shell models (see Section 1.2.2).

Quantifying coating thickness proved challenging because particle evaporation begins before the BC incandesces, causing the scattering signal to deviate from the ideal Gaussian beam profile. Moteki & Kondo (2008) developed a physical model to describe the time-dependent scattering cross-section of a particle as it passes through the Gaussian laser beam, enabling reconstruction of the full scattering signal. Gao et al. (2007) modified the detector setup with a four-quadrant photodiode to track each particle's position within the laser beam. This additional positional information helped constrain the Gaussian fit of the scattering signal. This work introduced Leading-Edge-Only (LEO) fitting to reconstruct the full scattering signals of particles within the Gaussian laser beam before thermal perturbation, enabling determination of coating thickness. This hardware modification has since been incorporated into later SP2 instruments. The LEO-fit is now a widely accepted method for retrieving mixing-state information (introduced in Chapter 2 and applied in the SP2 data processing toolkit development in Chapter 3).

The ongoing improvements to the SP2 reflect an iterative development process: each enhancement of the instrument has revealed new complexities that spurred further innovation. Since its origin as a laboratory prototype, the SP2 has been deployed on every continent to improve understanding of BC's global distribution, its mixing-state variability, and its role in climate forcing.

1.3.3 SP2 measurements and limitations

Schwarz et al. (2006) provided the first ambient atmospheric validation of the SP2 during research flights (from the boundary layer up to the lower stratosphere). They found that individual BC particle masses ranged roughly from 3 to 300 femtograms, and ~40% of the measured particles showed evidence of internal mixing. Since then, the SP2 has been deployed in a wide range of environments – from pristine polar regions to polluted megacities, in stationary observatories as well as on ships and high-altitude aircraft – demonstrating its broad utility.

The SP2 quantifies BC mass concentrations across many orders of magnitude – from ~2 ng m^{-3} in the Arctic summer atmosphere (Jurányi et al., 2023; Schulz et al., 2019) to over 20 µg m^{-3} in polluted megacities (Gong et al., 2016; Liu et al., 2019; Yang et al., 2022). These urban studies have revealed distinct source signatures: fresh traffic emissions typically show small BC cores (60-80 nm) with thin coatings, while aged biomass burning particles have larger cores (80-130 nm) with thicker coatings. Cappa et al. (2014) and Buffaloe et al. (2014) measured BC emission factors from ship plumes, finding predominantly uncoated BC particles in fresh marine exhaust; Ditas et al. (2018) documented wildfire smoke injection into stratosphere with BC concentrations averaging over 20 (and up to 100) times background levels, and particles covered by thick coatings. Zhang et al. (2018) retrieved BC mixing state at a polluted urban Beijing site, showing that polluted conditions promote rapid aging and thicker coatings, enhancing light absorption. Moteki et al. (2014) identified "attached-type" BC particles in Tokyo, where BC cores adhered to the surface of other particles rather than embedded within them. Similarly, Sedlacek et al. (2012) applied the lag-time analysis to distinguish non-core-shell BC morphologies. In remote regions such as the Tibetan Plateau and European Arctic, Wang et al.

(2014) and Zanatta et al. (2018) demonstrated that substantial fractions of BC particles become thickly coated during long-range transport due to atmospheric processing.

In practice, however, long-term and mobile field, deployments (ships, aircraft, remote sites, etc.) operate under unstable environmental conditions—platform motion, swings in pressure/temperature/humidity, and occasional power interruptions—that can shift laser capacity and detector response, introduce timing offsets and baseline drift, and create data gaps. Unstable conditions can compromise data quality. As a result, the data processing at these conditions requires the parameterization of signal waveforms and environmental changes. These realities motivate a robust, broadly applicable solution based on a deeper theoretical understanding of SP2 principles. Chapter 2 presents this theoretical framework in detail.

1.4 Research objectives and overview

Understanding the climatic impact of BC requires knowledge of how its atmospheric loading and mixing state evolve throughout its life cycle—from emission to removal. These properties determine how BC interacts with radiation and clouds, yet both are influenced by diverse and dynamic atmospheric processes. To study these effects, it is essential to obtain broad coverage, in situ observations spanning source regions, transport pathways, and remote background air. Marine regions are globally important yet under-observed, especially for particle-resolved mixing state. However, most field campaigns are limited to either near-source or background regions, providing snapshots rather than continuous coverage along the transport continuum. As a result, how BC's loading and mixing state evolve during long-range transport remains poorly constrained.

Single-particle-resolved BC measurements are valuable because BC mixing state is heterogeneous across particles and sizes, while population averages may obscure key optical and microphysical behaviors at particle level. The SP2 is widely deployed for this purpose, but its long-term and mobile operations (ships, aircraft, remote sites) face unstable conditions—platform motion, pressure/temperature/humidity swings, and intermittent power—that can shift laser alignment and detector baselines, introduce timing offsets, and create data gaps. Besides, retrieving particle-level properties from SP2 datasets remains computationally demanding and time consuming. Existing SP2 data-processing routines often rely on manual steps and in-house programming, leading to high numerical uncertainty and significant computational overhead at the campaign scale.

To overcome these technical limitations, this thesis addresses the following technical objectives:

(1) to enhance SP2 data-processing efficiency especially for long-term campaigns, reducing the SP2 data analyzing burden;
(2) to improve retrieval accuracy and stability under field conditions, as significant computational barriers exist in SP2 data processing, and the instrument exhibits highly environment-sensitive artifacts that may introduce uncertainties;

To advance the scientific understanding of marine BC and reduce uncertainty in its climate impacts, this thesis aims:

(3) to characterize episodic influences on BC in the oceanic environment (e.g., wildfire smoke intrusions, discrete shipping plumes), determining how such events perturb loading and mixing state relative to background marine processing and transport-regime effects;
(4) to establish a broad Atlantic observational baseline and map coastal-to-remote gradients in BC loading and mixing state, identifying primary environmental drivers such as vessel traffic density, distance from shore, relative humidity, and BC sizes;
(5) to determine the drivers and pathways through which the marine environment shapes BC aging process and mixing state across regions, to quantify their relative contributions;

To accomplish these objectives, the thesis is organized as follows (Fig. 1.2):

Shipborne observations were made with a Single Particle Soot Photometer (SP2) aboard the research sailing yacht S/Y Eugen Seibold (measurement platform), and all raw SP2 waveforms data were processed with the SP2 Parallel Accelerated Runtime Kit (SPARK) (data-processing routine), which converts signals to particle-resolved BC mass, mass-equivalent core size, optical total particle size, coating thickness and lag-time with automated drift corrections and parallelized throughput. This platform–toolkit together fulfils the technical objectives (1) and (2) by enabling accurate, scalable, and reproducible retrievals across multi-week marine campaigns. Building on these processed products, Chapter 3 delivers the Atlantic baselines proposed by (objective 4), a characteristic marine background (~100 ng m^{-3}) and coast-to-remote gradients in loading and mixing state—while quantifying key environmental controls (emission sources, humidity) and documenting episodic perturbations such as discrete shipping plumes (objective 3). Chapter 4 then applies trajectory-based regime separation (continental-dominated vs marine-dominated transport) to attribute mechanisms and pathways (objective 5), suggesting that coagulation with marine aerosol and high-RH/cloud cycling drive the formation of thickly coated (with coating thickness 100-200 nm) core–shell BC during over-ocean transport, and further examining wildfire-smoke episodes (objective 3). Ultimately, this thesis provides campaign-scale, particle-resolved observational constraints that inform and constrain the parameterization of BC loading and mixing state in marine environments, thereby improving future climate modeling and predictions of BC's role in global climate change.

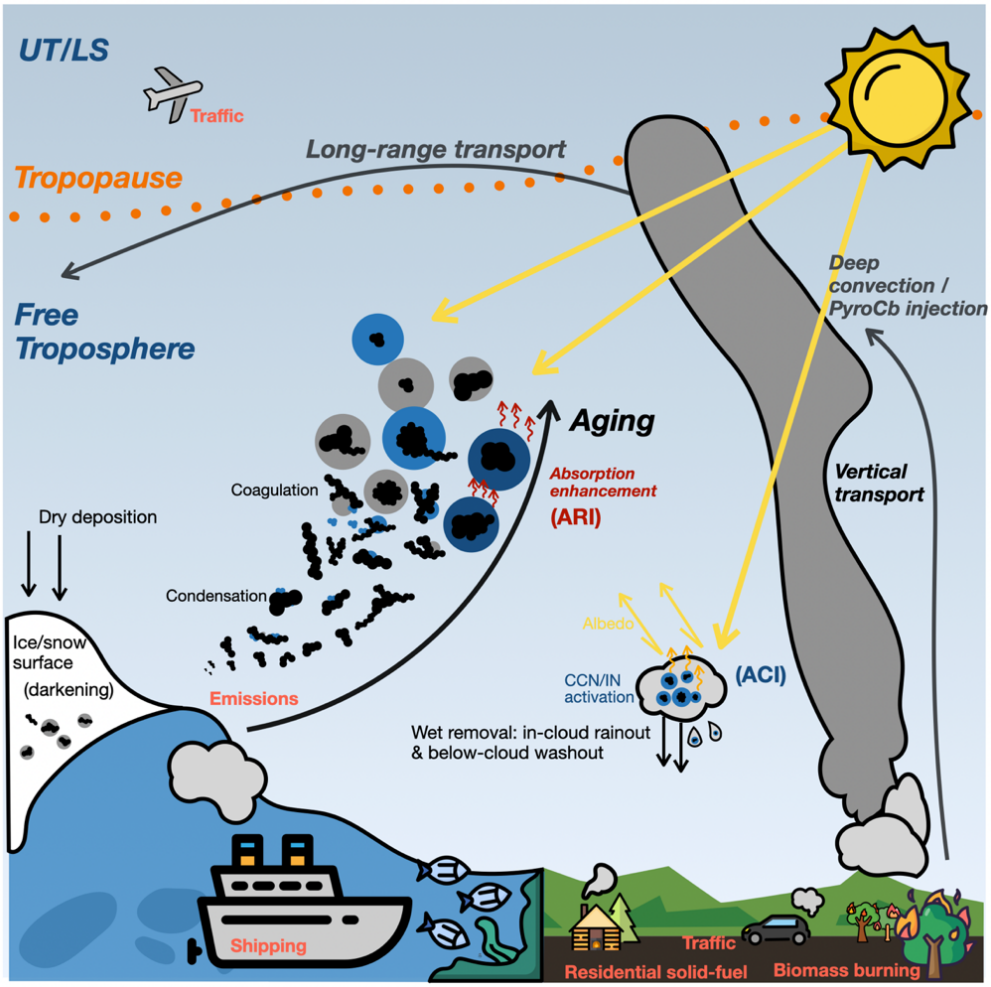

Figure 1.1. Conceptual schematic of the atmospheric lifecycle and climate effects of black carbon (BC). Emissions from combustion are transported and lofted; particles age by condensation, coagulation, and restructuring, evolving from fresh aggregates to attached-type and internally mixed (core-shell) forms. BC absorbs sunlight (ARI), with efficacy enhanced above clouds/bright surfaces, influences clouds via CCN/IN activation (ACI), and is removed by wet and dry deposition, including snow/ice darkening.

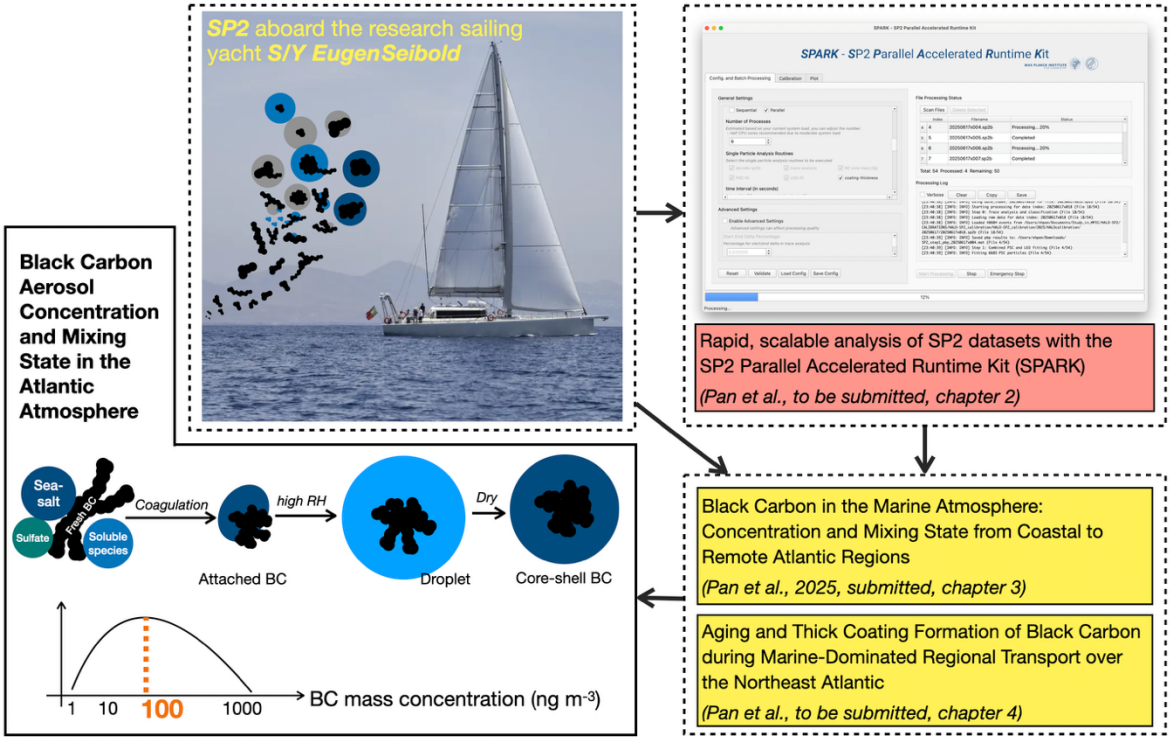

Figure 1.2. Structure and key findings of this thesis, arrows indicate the workflow from observations to processing to scientific outputs. Dashed boxes denote the components in this thesis: the shipborne measurement platform (SP2 aboard the research sailing yacht S/Y Eugen Seibold) and the SP2 Parallel Accelerated Runtime Kit (SPARK) used for rapid SP2 data processing. The solid-line box summarizes the conceptual framework for marine BC loading and aging. The colored boxes denote the chapters.

Chapter 2 Rapid, scalable analysis of SP2 datasets with the SP2 Parallel Accelerated Runtime Kit

This work is to be submitted as Pan et al. (2025):

Pan, X., Ma, N., Zhang, Y., Su, H., and Cheng, Y.: Rapid, scalable analysis of SP2 datasets with the SP2 Parallel Accelerated Runtime Kit, Atmospheric Measurement Techniques, to be submitted, 2025

I am the first-author of this work and my contribution to this work includes improving the numerical algorithms, writing the code, benchmarking the toolkit's performance, making the figures and tables, discussing the results, interpretation and drafting the manuscript.

The following text, figures, and tables quoted (within “”) from page 15 to page 42 are the same as the manuscript which is cited on page 14.

“

Abstract

The SP2 is widely deployed on ships, aircraft, and at remote sites, but long-term field operation introduces variable pressure, temperature and humidity that shift laser alignment and detector baselines and thereby increase uncertainty in per-particle retrievals. Processing SP2 data under these conditions requires waveform parameterization and environmental corrections. Besides, long term campaigns can produce very large SP2 raw dataset—often from gigabytes to terabytes. In practice, however, the SP2 data-processing approaches are either in-house script developed by research groups, either plug-ins layered onto commercial software. These tools often lack automation, scalability, and parallel processing, so campaign scale datasets remain slow and resource intensive to analyze.

To address these shortcomings, this work developed the SP2 Parallel Accelerated Runtime Kit (SPARK), a cross-platform, configurable processing toolkit that converts raw SP2 waveforms into per-particle properties at campaign scale per-particle properties and time-aggregated products at campaign scale. It builds on the principle of how the SP2 utilizes laser-induced incandescence (LII) to measure particle-resolved mass and mixing-state information (section 2.1). The features of this toolkit are presented in section 2.2. The end-to-end workflow is presented in section 2.3 with focusing on several optimizations Gaussian fitting routine with an analytical Jacobian to characterize the laser, a closed-form leading-edge-only (LEO) fit for undistorted BC scattering. The parallel implementations are introduced in section 2.4, the benchmarks and validations are in section 2.5.

2.1 Theoretical foundations of SP2

The SP2 heats refractory BC in a focused 1064 nm laser and records their response as scattering and incandescence waveforms. Under typical SP2 conditions, BC is heated at rates exceeding 3×10^{8} K s^{-1} within ~10 µs and reaches incandescence temperatures of 3700-4300 K (Moteki and Kondo, 2010). During the heating, non-refractory material evaporates at lower temperature (typically < 1000 K), so coating loss occurs before BC incandescence. This temporal separation can be used to infer mixing state (from when scattering changes) and BC mass (from the incandescence amplitude) (Moteki and Kondo, 2007; Schwarz et al., 2006).

2.1.1 Energy balance in LII

BC particle temperature evolution during LII follows an energy balance (Liu and Snelling, 2007; Michelsen et al., 2007; Schulz et al., 2006a). As shown in Fig. 2.1, under SP2 operation conditions, the dominant mechanisms are (Michelsen et al., 2015):

$$\frac{dU_{int}}{dt} = Q_{abs} - Q_{rad} - Q_{cond} - Q_{sub} + Q_{Additional} \tag{2.1}$$

where U_{int} represents the particle internal energy and the Q terms represent the dominant energy transfer pathways (Fig. 2.1). Q_{abs} is the absorptive heating, the dominate heating pathway during LII; Q_{rad} is the thermal radiation emission, Q_{sub} is the evaporative cooling during carbon sublimation, Q_{cond} the conductive cooling. Additionally, the residual term $Q_{Additional}$ collects minor processes such as oxidation, structural annealing, and thermionic emission, which together contribute less than 5% to the energy budget under typical SP2 flow conditions and laser fluences (Bambha and Michelsen, 2015; Liu and Snelling, 2007; Michelsen et al., 2015; Schulz et al., 2006a).

At the initial heating stage (particle temperature T < 2000 k), the Q_{abs} provides the sole energy input, the heated BC particle starts emitting thermal radiation Q_{rad} (roughly $\propto T^5$). Between 2000-3000 K, conductive cooling Q_{cond} remains the primary cooling pathway (Michelsen et al., 2015), Q_{rad} also increases rapidly due to its T^5dependence. Above 3500 K, Q_{cond} begins to contribute significantly, capping the particle's temperature at ~4000 K. At this point, vapor-pressure equilibrium prevents further heating, marking the point of incandescence and the occurrence of the LII peak (Bambha and Michelsen, 2015; Michelsen et al., 2015).

2.1.2 From the LII energy balance to SP2 implementation

The SP2 implements LII physics by coupling a well-characterized temporal irradiance profile to a four-channel optical/detection system. A continuous-wave 1064 nm Nd:YAG laser (TEM_{00} mode) produces a Gaussian spatial intensity:

$$I(r) = I_0 \exp\left(-\frac{2r^2}{w^2}\right) \tag{2.2}$$

Where I_0 is the peak irradiance and w ~0.2 mm is the significant waist. A laminar aerosol stream carries particles perpendicular to the beam at around ~48 m s^{-1} (under standard operation condition), yielding a temporal profile for each particle transit (Moteki and Kondo, 2007),

$$I(t) = I_0 \exp\left[-\frac{(t-\tau)^2}{2\sigma^2}\right] \tag{2.3}$$

where τ is the moment when the particle passes through the beam center (maximum intensity), and σ represents the temporal width (~3-4 μs). This σ emerges from the ratio of the beam diameter to the particle velocity: a wider beam or slower flow extends the interaction time, while narrower beams or faster flows compress it (Moteki and Kondo, 2008).

During the incandescence progress, absorptive heating (Q_{abs}) dominates initially, driving temperature upward until balanced by radiative losses (Q_{rad}) and sublimation cooling (Q_{sub}),

stabilizing around ~4000 K (Michelsen et al., 2007; Moteki and Kondo, 2007). The detected incandescence signal $S_{\mathrm{inca}}(t)$ integrates emitted thermal radiation across wavelengths and angles, expressed as (Moteki and Kondo, 2007, 2010):

$$S_{inca}(t) = \frac{\pi}{4} d_m^2(t) \int_{\Delta\Omega} \int_0^{\infty} Q_{abs} \cdot P_e(T(t), \lambda) \cdot \eta(\lambda)\, d\lambda\, d\Omega \tag{2.4}$$

Here, $P_e(T(t), \lambda)$ is Planck's emission function at instantaneous particle temperature, and $\eta(\lambda)$ represents the wavelength-dependent sensitivity of the detection system (e.g., SP2 detectors' filter transmissions and detector quantum efficiencies). Q_{abs} depends on particle size, morphology, complex refractive index, and orientation angles relative to laser polarization and detection geometry (Michelsen et al., 2015; Moteki et al., 2010; Moteki and Kondo, 2010).

Under typical SP2 conditions (BC particles <500 nm and a detection wavelength of 1064 nm), the Rayleigh approximation applies, simplifying the absorption efficiency to (BOHREN and HUFFMAN, 1983; Michelsen et al., 2015; Moteki and Kondo, 2010):

$$Q_{abs} = \frac{4\pi d_m}{\lambda} \mathrm{Im}\left\{\frac{m^2 - 1}{m^2 + 2}\right\} \tag{2.5}$$

This simplified form reveals the key relationship underlying SP2 measurements: Q_{abs} proportional to the BC mass equivalent diameter d_m, inversely proportional to wavelength λ, and dependent on intrinsic absorption capacity via Im $\left\{\frac{m^2-1}{m^2+2}\right\}$. The refractive index term remains nearly constant for atmospheric BC (Bond and Bergstrom, 2006). Moteki & Kondo (2007) confirmed experimentally that organic coatings do not alter the BC core incandescence signal, validating this approximation. Further, Moteki & Kondo (2010) demonstrated a linear LII-to-mass relationship in the Rayleigh domain, with deviations emerging only for larger particles or compact morphologies.

When BC particles with volatile coatings experience this laser heating, the temperature rise triggers sequential evaporation of coating materials (section 2.1.1). Initially, as particles enter the low-intensity beam area, they scatter laser light without experiencing significant heating. This elastic scattering produces a signal $S_{\mathrm{scat}}(t)$ that relates directly to the particle's optical properties:

$$S_{\mathrm{scat}}(t) = s \cdot I(t) \cdot \Delta C_{scat}(t) \tag{2.6}$$

where s represents an instrument-specific calibration constant that accounts for detector sensitivity, optical transmission efficiency, and electronic gain factors. The term $\Delta C_{scat}(t)$ denotes the differential scattering cross-section integrated over the detector's collection solid angle, quantifying how much laser light the particle scatters toward the detectors (Moteki and Kondo, 2008). For particles that remain unchanged during beam transit, maintaining constant size and refractive index, the ΔC_{sca} remains constant, causing the scattering signal to closely

mirror the Gaussian laser intensity profile. In these cases, the scattering signal essentially follows the Gaussian laser intensity profile. This behavior allows one to determine the particle's initial optical diameter by comparing the signal to Mie theory predictions (Gao et al., 2007; Moteki and Kondo, 2008). The details are presented in section 2.3.

2.2 Features of SPARK

As detailed above, the SP2 uses optical detectors to measure how individual aerosol particles interact with its laser beam. The instrument records high-frequency scattering and incandescence signals, which are digitized and stored directly as raw binary waveforms—high-resolution time series capturing each particle's detailed optical response. Rather than directly outputting physically meaningful parameters (such as particle mass, size, or coating thickness), the SP2 provides these raw waveform data as its final data products. To efficiently process such waveforms, a specific workflow is developed in this work, namely the SP2 Parallel Accelerated Runtime Kit (SPARK).

SPARK is implemented in Python and distributed as a standalone executable for Windows, macOS, and Linux. All required libraries are bundled to prevent version conflicts and ensure consistent cross-platform performance. Numerical computations use NumPy and SciPy, non-computational components (data I/O, logging, error handling, parallel orchestration) rely on Python's standard libraries.

SPARK supports both serial and parallel execution. Parallelization is fully integrated (see section 2.4) and can be enabled via the GUI or a configuration file (Appendix B). The toolkit provides both graphical user interface (GUI) (Fig. 2.2) and a command-line interface (CLI). Both interfaces share a common configuration file to ensure consistent, reproducible settings; a complete parameter list is given in Appendix B.

Users can start runs from the GUI or by pointing the CLI to a config file, on a laptop or through high-performance computing (HPC) clusters. SPARK processes the raw signal traces from the SP2 instrument and organizes its outputs into two categories:

(1) Per-particle results. Each event is classified as BC-containing or purely scattering (PSC). For BC events, outputs include rBC core mass, optical diameters (core size and total size), coating thickness (when applicable), and scattering/incandescence amplitudes. PSC outputs include optical diameters and scattering amplitudes.

(2) Aggregated summaries. Individual results are grouped over user-defined intervals (minutes to hours) to produce time-resolved metrics (e.g., BC mass concentration, PSC number concentration) and statistics (median/mean/variance of coating thickness). These outputs enable downstream analysis and visualization.

2.3 SP2 Data Processing Workflow in SPARK

The SP2 integrates four optical channels that capture different aspects of particle-laser interactions. Two avalanche photodiodes (APDs) monitor elastic light scattering at the laser wavelength (1064 nm), where one detector measures total scattering intensity (denoted as “SC” hereafter) while the other is configured as a two-element avalanche photodiode (TEAPD, denoted as “SP” hereafter). The scattering channel employs long-pass optical filtering (transmitting only $\lambda > 850$ nm) to exclude potential incandescence signals that would contaminate the elastic scattering measurement (Moteki and Kondo, 2007). Two photomultiplier tubes (PMTs) capture thermal emission in distinct bands (broadband ~350-800 nm; red narrow ~630-800 nm) for mass-sensitive incandescence and color-ratio thermometry.

The SP2’s final data product is a stream of binary waveforms: eight traces (high/low-gain pairs for four optical channels) sampled at 2.5 MHz for every detected particle. Each channel provides ~100 samples, so a single event contains ~800 samples plus per-event metadata (status flags, timestamps, etc.). A typical raw file records ~50,000 particle events—about 80 MB—and multi-week deployments routinely accumulate terabytes which makes long-term data management and processing operationally challenging. The toolkit first reads each raw file as a 16-bit big-endian stream and extracts metadata (timestamps, event counts, channel counts, points per record, channel flags, saturation flags) (Droplet-Measurement-Technologies, 2022b). For each channel’s waveform, a baseline is computed from the first samples (default 10, configurable), then three features are derived: baseline-subtracted peak intensity, time-of-peak, and waveform width. These features drive classification and subsequent fits; all amplitudes used later are baseline-subtracted (Ditas et al., 2018; Droplet-Measurement-Technologies, 2022b, a).

The overall workflow of SPARK follows the basics of the existing established frameworks (PSI SP2 Toolkit v4.116): (1) event pre-processing and classification (PSC vs BC); (2) fit PSC scattering signals with a Gaussian to recover the instantaneous beam profile and timing parameters used later; (3) reconstruct undistorted BC scattering on the leading edge, optionally using the dual-channel constraint; and (4) convert incandescence to mass, then retrieve core size and coating thickness via Mie Theory (BOHREN and HUFFMAN, 1983). Section 2.3.1 introduces the PSC Gaussian fit; section 2.3.2 describes LEO for BC scattering; section 2.3.3 details optical sizing/coating retrievals.

2.3.1 Scattering signals of PSC particles

A non-absorbing particle traversing the beam produces a Gaussian-shaped scattering pulse whose time dependence reflects the transit-time irradiance defined in section 2.1.2 (Moteki and Kondo, 2008). To recover the instantaneous beam profile for each data segment, this toolkit every PSC scattering waveform to a Gaussian function (Gao et al., 2007; Moteki and Kondo, 2007):

$$g(t_i; A, \mu, \sigma) = A_{PSC} \cdot \exp\left(-\frac{(t_i - \mu)^2}{\sigma^2}\right) + w_i, i = 1,2,\cdots 100 \quad (2.7)$$

where t_i is time (sampled at 0.4 µs intervals over 100 samples), A_{PSC} is the scattering amplitude (proportional to the particle's scattering cross-section in the laser beam), μ is the Gaussian center (i.e., time of peak intensity), and σ is the Gaussian width set by the particle transit time and the beam profile. The term w_i is time-dependent and accounts for small, systematic deviations of the measured waveform, e.g., baseline shifts and/or minor optical-alignment asymmetries. Previous studies treated the baseline offset as a constant offset (Gao et al., 2007; Metcalf et al., 2012).

In practice, omitting w_i from the fitting does not bias convergence of A_{PSC}, μ and σ, the w_i is therefore obtained after the Gaussian fit as the residual between the measured trace and the fitted Gaussian. For a perfect Gaussian-shaped signal, $w(t_i)$ would be zero at any t_i. Figure S2.1 demonstrates how real scattering signals depart slightly from the ideal Gaussian shape. Although these departures are small and the fitter minimizes residuals regardless, they can become non-negligible for BC scattering reconstructions that rely on very few leading-edge samples (see section 2.3.2); carrying w_i forward helps characterize and correct such shape imperfections.

The PSC fitting also derives the cross-to-center delay, $\Delta t_{SP} = \mu - t_{SP}$ where t_{SP} is the split-position determined by the notch in the two-element avalanche photodiode (TEAPD) detector (Gao et al., 2007), as shown in Fig. 2.4. Because the notch location and the beam center μ are both optically fixed, Δt_{SP} is also expected to be fixed and is independent of t_{SP} under stable operating conditions and is therefore can be used to shape the laser beam shape for downstream use in BC-particle analysis (section 2.3.2) (Gao et al., 2007).

In this toolkit, we exploit the empirical relationship between the recorded t_{SP} and particle scattering ability—represented here by PSL size. As shown in Fig. 2.5, larger PSLs (stronger scatterers) tend to appear later in the 100-point time window (larger t_{SP}), whereas smaller PSLs (weaker scatterers) yield smaller t_{SP}. Because the sample airflow is fixed (well-controlled laminar flow, 0.12 L min^{-1}) and PSLs in the 0.2–1 µm range move at uniform velocity, transit-speed differences are unlikely (Moteki and Kondo, 2007; Seinfeld and Pandis, 2006). A more plausible explanation for this relationship is the SP2's amplitude-based trigger: recording begins when the signal crosses a fixed count threshold. Because the saved 100-point snippet is anchored to that trigger and always includes the same number of pre-trigger samples, a stronger scatterer reaches the threshold farther out on the leading edge (earlier in real time), so more of the pre-center portion of the pulse is captured before the split; the split (and center) therefore appear later in the saved window (Schwarz et al., 2022). Weaker scatterers reach the threshold closer to the beam center, so less pre-center time is captured and the split falls earlier in the record. Thus, stronger scatterers trigger earlier on the front edge of signal, and their split (and center) appear later in the 100-point record (larger t_{SP}); weaker scatterers trigger closer to the center and produce smaller t_{SP}.

This particle scattering ability-dependent shift also influences the baseline w_{i}, which varies systematically with t_{SP} and therefore can be parameterized as $w_{\mathrm{i}}(t_{SP})$. Figure 2.6 shows the $w_{\mathrm{i}}(t_{SP})$ grouped by t_{SP}, exhibit, the shape and magnitude of $w_{\mathrm{i}}(t_{SP})$ evolve with the t_{SP}. This allows the toolkit to estimate a $w_{\mathrm{i}}(t_{SP})$ profile as a function of t_{SP} prior to knowing the scattering amplitude, to further correct the laser beam shape deviations.

In practice, the fitted σ can drift over time (due to flow oscillation, optical misalignment, etc). For instance, in an airborne campaign, reducing the SP2's sample flow (due to the altitude changes) from 128 cm^3 min^{-1} to 112 cm^3 min^{-1} can shift the σ ~10% (0.4 µs steps; Fig. 2.7). In this toolkit, σ is updated at short, user-defined intervals to track such drift.

To efficiently process large datasets—often involving hundreds of millions of PSC particles—this toolkit implements a custom Levenberg–Marquardt least-squares fitter with an analytical Jacobian. The Jacobian matrix provides exact derivatives of the Gaussian fit function, guiding the optimizer directly toward the minimum and avoiding costly numerical differentiation at each iteration (Boyd and Vandenberghe, 2004; Virtanen et al., 2020). Benchmarking on ~60000 ambient PSC scattering signals (identical convergence criteria: relative parameter change $<10^{-6}$, max 300 iterations) shows that, compared to the conventional finite-difference Jacobian approach, the analytical Jacobian reduces the number of iterations by a factor of five and shortens runtime by approximately 30% (Figure S2.2). The numerical implementation of this routine is provided in Appendix A. Once convergence, the fit returns the best-fit values of A_{PSC}, μ and σ for each PSC signal, defining the laser beam profile $g(t_i)$ under current conditions, $w(t_i)$ is extracted as the residual after fit convergence (Appendix A).

At this stage, the laser-beam profile can be determined for downstream BC reconstruction, with accounting for (1) small, time-dependent baseline/optical-alignment deviations captured by $w_{\mathrm{i}}(t_{SP})$ and (2) slight width shifts in σ due to flow or minor alignment changes.

2.3.2 Reconstruction of the BC scattering signals

BC-containing particles interact strongly with the SP2 laser beam due to their high absorptivity. As they heat up, coating on BC particles can vaporize or undergo phase transitions (e.g., melting or fragmentation), leading to changes in their size and scattering cross-section (Bambha and Michelsen, 2015; Michelsen et al., 2015). As a result, their scattering signals deviate from the Gaussian shape expected for non-absorbing particles (Moteki et al., 2014; Moteki and Kondo, 2007). Estimation of the mixing state of BC-containing particles therefore requires reconstruction of their undistorted scattering signals.

The LEO-fit method reconstructs the scattering amplitude of BC-containing particles by fitting a Gaussian function to the earliest, unperturbed portion of the particle's scattering signal (Gao et al., 2007). The Gaussian shape (i.e., μ_{BC}, σ, and the t_{SP}-dependent weighting function $w_{\mathrm{i}}(t_{SP})$) is derived by fitting PSC particles (section 2.3.1), therefore only the amplitude A_{BC} needs to be solved, the model becomes linear in A_{BC} (Gao et al., 2007). In our implementation, we avoid

iterative curve-fitting algorithms and instead use a closed-form solution for this linear least-squares amplitude fit (see Appendix A for details) to improve efficiency.

Selecting the leading-edge window requires balancing bias (from early heating/evaporation) against variance (signal-to-noise ratio, SNR and sample count). A common practice is to set the last fit sample at an amplification factor of 20–30 (i.e., fit down to 5–3.3 % of the peak laser intensity), which keeps the window safely on the unheated front (Gao et al., 2007; Metcalf et al., 2012). Going earlier (e.g., ~3.3 %) would further minimize evaporation bias but reduces SNR and may leave too few valid points, especially for small particles; going later increases SNR but risks including portions already affected by heating. Recent studies emphasize both sides of this trade-off: Laborde et al. (2012) set the LEO upper bound 2 µs before the earliest incandescence time—i.e., a more conservative cutoff than the commonly used ~3.3 % of peak laser intensity and justified its reliability, while Naseri et al. (2024) identify that for some thickly coated or highly volatile particles, even a ~3.3 % threshold can be too late—such particles may begin evaporating before the SP signal can reliably determine position, so they are excluded from LEO altogether.

To address the issues above, the SPARK toolkit adopts two strategies:

(1) Providing better constraining for the fitting by validate laser beam geometry (μ_{BC}, σ and $w_{\mathrm{i}}(t_{SP})$) used for the amplitude fit, as already introduced in section 2.3.1.

(2) Use the scattering signal from SP channel for the LEO-fit, then place it on the SC scale with a stable ratio. Both SC and SP detectors (APDs) observe the same 1064-nm elastic-scattering event; they differ only by an instrument-specific gain ratio $R_{SP/SC}$, which is derived from undistorted PSC signals fitting. Choosing SP channel for the LEO-fit because it delivers higher SNR than SC channel: the SP is operated as a position-sensitive, differential (split-and-invert) detector and is naturally tuned with higher analog gain so that the particle position can be robustly detected. In addition, with its long-pass filter of visible light, which background (e.g., Rayleigh/stray light) and yields cleaner signals (Schwarz et al., 2015).

This strategy is verified by applying LEO fit from both SP and SC signals on PSL and ambient PSC particles, as described in section 2.5.2, the SP-based LEO fit provides higher accuracy and lower variability. Yuan et al., (2020) also reported narrower single-particle spreads (tighter 10th/90th percentiles) when using SP signals for LEO than using SC signals. We also tested the sensitivity of $R_{SP/SC}$, Fig. 2.8 shows the $R_{SP/SC}$ obtained from 2 different instruments, e.g., ~4 in one and ~40 in another. Although the absolute ratio is instrument-dependent, $R_{SP/SC}$ is highly stable within each instrument and is particle size independent.

2.3.3 Retrieving the particle sizes, mixing state and coating thickness

After processing the SP2 signals as described above, the toolkit determines particle size metrics and BC mixing state. For PSC particles, each particle's calibrated scattering peak intensity is

converted to an optical-equivalent particle diameter D_{PSC} based on Mie theory, assuming a homogeneous sphere of known refractive index RI_{PSC} and using PSL calibration. Figure 8 shows Mie calculations based on commonly used (see Appendix B for a comprehensive list) refractive index assumptions.

Both the calibration parameters and refractive index are user-specified inputs provided via the configuration file or GUI. These Mie-based sizes retrieval methods are well-standardized in existing SP2 data analysis (Ditas et al., 2018); here, we present the integrated, automated implementation within the SPARK toolkit.

For each BC-containing particle, the toolkit first computes a lag-time as the difference between the peak of the scattering signal and the peak of the incandescence signal (Moteki and Kondo, 2007; Sedlacek et al., 2012). This lag-time reflects the particle's thermal response and is a qualitative indicator of mixing state: short lags suggest bare or thinly coated BC (external mixed), while longer lag-times indicate thick coatings (internal mixed). The toolkit outputs the lag-time per particle and corresponding statistical. The application of the lag-time is presented in the next Chapter 3 and 4.

In addition to the lag-time, the toolkit retrieves two diameters for each BC particle (assuming a spheric core-shell structure): the BC core diameter (D_{core}) and the total optical diameter (D_{total}). The coating thickness (CT) is then derived: $CT = (D_{total} - D_{core})/2$. The calculation proceeds as follows: First, convert the incandescence signal to BC mass using user-provided calibration curves (assuming a spherical core density), then compute D_{core} from that mass and density. Next, using the reconstructed scattering amplitude A_{BC} (from the LEO-fit) and known D_{core}, interpolate a precomputed Mie lookup table relating scattering cross-section to D_{total}. These lookup tables are parameterized by D_{core}, core/coating refractive indices (RI_{core} and $RI_{coating}$), and core density. All required lookup tables (based on common combinations of RI_{core} and $RI_{coating}$) are bundled with the toolkit. Users may select the appropriate table, or customize inputs (e.g., refractive indices, core density) via the GUI or CLI to match their measurement conditions.

2.4 Parallel computing strategies in SPARK

SPARK can process SP2 datasets of any size in serial or parallel mode. In serial mode, all steps run sequentially on a single core with minimal overhead—ideal for small datasets or standalone use (Fig. 2.9, left panel). In parallel mode, the toolkit uses process-based parallelism (multiple independent worker processes) rather than multi-threading. This approach bypasses Python's Global Interpreter Lock (GIL) and is better suited for CPU-intensive SP2 processing. An automated resource-tuning feature estimates the optimal number of worker processes based on dataset size, available CPU cores, and current system load, maximizing throughput without requiring users to configure parallel settings manually.

Two parallelization approaches are supported: (1) a shared-memory model that uses multiple cores of a single machine, and (2) a distributed-memory model that runs across multiple machines. This setup allows the same code to scale from a personal laptop up to an HPC cluster. In shared-memory mode, the toolkit automatically manages the creation of worker processes and the distribution of tasks.

On a single machine (single node), the toolkit uses a shared-memory strategy based on Python's built-in multiprocessing process pool. When parallel processing begins, a pool of worker processes is spawned (Fig. 2.9, middle panel), and each worker runs the SP2 processing workflow independently (section 2.3). As soon as a worker finishes processing its current file or time-chunk, it automatically retrieves the next task from a queue. This persistent process-pool strategy avoids repeated process startup overhead and keeps all CPU cores busy until the entire dataset is processed. To keep the GUI responsive during parallel execution, we use an individual compute thread oversees the worker pool. Worker processes send progress updates, warnings, and errors via a thread-safe queue to a central handler. A separate listener process logs these messages (with timestamps) and refreshes the GUI in real time. If the user clicks "Stop" or any worker encounters a critical error, the toolkit performs an orderly shutdown: the master process logs the event and gracefully terminates all workers to prevent data corruption.

For multi-node HPC environments, the toolkit provides a distributed-memory parallel solution (coordinated via the Message Passing Interface, MPI). At startup, the master node (rank 0) broadcasts the configuration (calibration parameters, file lists, etc.) to all worker nodes. Each node then processes its assigned portion of the dataset independently (as illustrated in Fig. 2.9, right panel), with minimal inter-node communication needed during processing. This straightforward architecture yields near-linear performance scaling even as the number of nodes increases. The benchmarks for the parallel strategies (for both shared-memory and distributed-memory cases) on large SP2 datasets (see section 2.5)

2.5 Performance benchmark and validation

2.5.1 The parallel efficiency benchmark

We benchmarked the SPARK using a large SP2 dataset comprising 1921 raw ".sp2b" files collected over ∼1 000 h. Each file contains eight-channel waveform traces for roughly 50000 particle events. We partitioned the full dataset into 23 sub-workloads—each corresponding to a unique calibration set (13–478 files)—and used the number of BC-containing particles in each sub-workload as a proxy for workload complexity.

In shared-memory mode, each sub-workload was processed on a single HPC node with 72 cores, using a process pool of 10–60 workers (proportional to workload size). In distributed-memory mode, we ran all sub-workloads in one MPI job across four nodes (288 cores). MPI initialization took ~10 seconds in this case, which is negligible compared to total runtime.

Figure 2.10a compares total processing time in parallel vs. serial mode as a function of the number of BC-containing particles. Each point represents a sub-workload; the y-axis is the parallel processing runtime and the point's color denotes the corresponding serial processing runtime. All parallel runs are substantially faster—often about an order of magnitude—especially for workloads exceeding ~2×10^6 BC particles. The red-highlighted point corresponds to the distributed-memory run on the entire dataset, which completed in 7.7 minutes.

Figure 2.10b shows the observed speedup (serial runtime divided by parallel runtime) versus the number of processes, with the ideal linear scaling line for reference. We compute parallel efficiency as speedup normalized by the number of processes. According to Amdahl's law (Amdahl, 1967) , efficiency approaches 1 for ideal scaling but is always less. In our tests, efficiency remained high and stable (mean ± std: 0.81 ± 0.07) across different BC concentrations and both parallel modes. The deviation from 100% efficiency is attributable to overhead and occasional load imbalance (e.g., when some cores idle due to variability in workload).

Overall, these benchmarks show that process-based parallelization—on a single multi-core machine or across an HPC cluster—substantially accelerates SP2 analysis, reducing days of serial runtime to minutes.

2.5.2 LEO-fit validations

To validate the LEO fitting implementation and evaluate the advantages of using SP signal (instead of SC), we applied both methods to a dataset consisting of ambient PSC particles collected from oceanic environments and PSL standards. Using the LEO fit on SC signal (amplification factor 20) yielded stable but low calibration slopes (~0.75 for PSL and ~0.71 for ambient PSC), consistent with previous studies (Gao et al., 2007; Metcalf et al., 2012). In contrast, the LEO fit on SP signal (amplification factor 25) significantly improved the fitting quality: the slopes were much closer to unity (approximately 1.00 for PSL and 1.20 for ambient PSC; see Fig. 2.11). The data points also cluster much tighter around the 1:1 line with the dual-channel method, illustrating the improvement. These results demonstrate that our toolkit's LEO implementation accurately reconstructs the undistorted scattering signals, and that the dual-channel approach further enhances the fit reliability.

2.5.3 Optical sizing validations

We validated the optical sizing for both core-shell BC (lag-times >1.6 μs) and PSC particles by comparing SP2-derived total optical diameters of D_{total} with monodisperse aerosol sizes selected by a differential mobility analyzer (DMA) during the filed campaign at the Xianghe, China (Zhang et al., 2016; 2018). In this configuration the DMA set mobility diameters to 250, 300, and 350 nm and delivered the classified aerosol directly to the SP2. The DMA scanned across these sizes repeatedly for 4 days and we adopted from these 4 days. For core-shell BC retrievals we adopted the refractive indices $RI_{coating} = 1.42 + 0\mathrm{i}$ and $RI_{core} = 1.84 - 0.84\mathrm{i}$, and effective BC core density of 1.2 g cm^{-3}; PSC particles were treated as homogeneous spheres

with $RI_{PSC} = 1.42 + 0\mathrm{i}$, consistent with the assumed coating composition (Zhang et al., 2016; 2018). Core-shell BC were processed with the workflow described in section 2.3, to obtain core size D_{core} from incandescence-derived BC mass and D_{total} from LEO-reconstructed scattering and core–shell Mie lookups. Since the per-particle BC mass dependent only on the incandescence peak height and incandescence-to-mass calibrations, so we expect accurate BC mass calculations thus only the core-shell BC total size validations are conducted.

Figure 2.11 shows the normalized SP2 optical-diameter distributions for PSC and core–shell BC at the three DMA set sizes. PSC distributions exhibit sharp peaks that align with the DMA mobility diameters, confirming accurate sizing for non-absorbing particles under the assumption of $RI_{PSC} = 1.42 + 0\mathrm{i}$. Coated-BC distributions are broader—reflecting variability in shell thickness and refractive index relative to the fixed-parameter Mie tables—but their means agree with the DMA set points; multiple-charge modes are also resolved in the SP2 distributions. Collectively, these comparisons indicate that the toolkit retrieves reliable optical sizes for both PSC and coated-BC particles under realistic campaign conditions, supporting the use of SP2-derived size and mixing-state metrics in subsequent analyzes.

2.6 Summary

The methods in this chapter establish a scalable workflow that converts raw SP2 waveforms into calibrated per-particle properties and time-aggregated products while explicitly correcting for environmental drift. SPARK's Gaussian beam characterization with an analytical Jacobian, closed-form SP-based LEO reconstruction, enable robust retrievals of rBC mass, optical sizes (core and total), coating thickness, and lag-time; process-based parallelism scales the same code from laptops to multi-node HPC, reducing days of serial runtime to minutes.

The remainder of this thesis leverages that capability: Chapters 3–4 apply SPARK to campaign datasets to quantify BC loadings, and BC size distributions, coating statistics, and mixing-state dynamics in Atlantic Ocean from shipborne measurement.

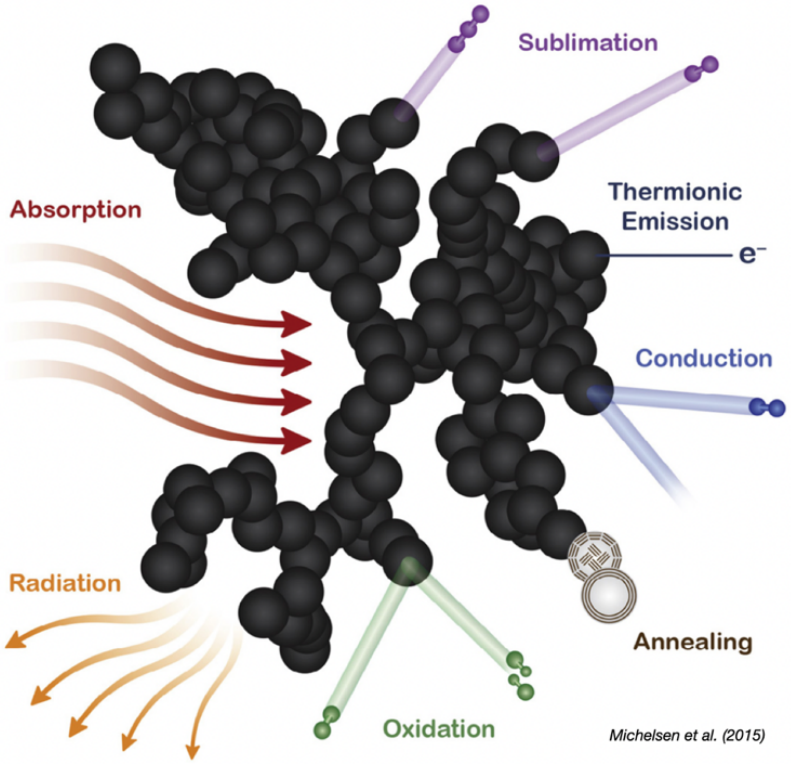

Figure 2.1. Energy transfer mechanisms that govern laser-induced incandescence in BC particles. Laser absorption provides the primary energy input, driving particle temperatures to ~4000 K. Energy dissipation occurs through conduction to surrounding gas, thermal radiation, and sublimation at high temperatures. Minor processes (oxidation, annealing, thermionic emission) contribute less than 5% to the total energy budget under typical SP2 conditions. Adapted from Michelsen et al. (2015).

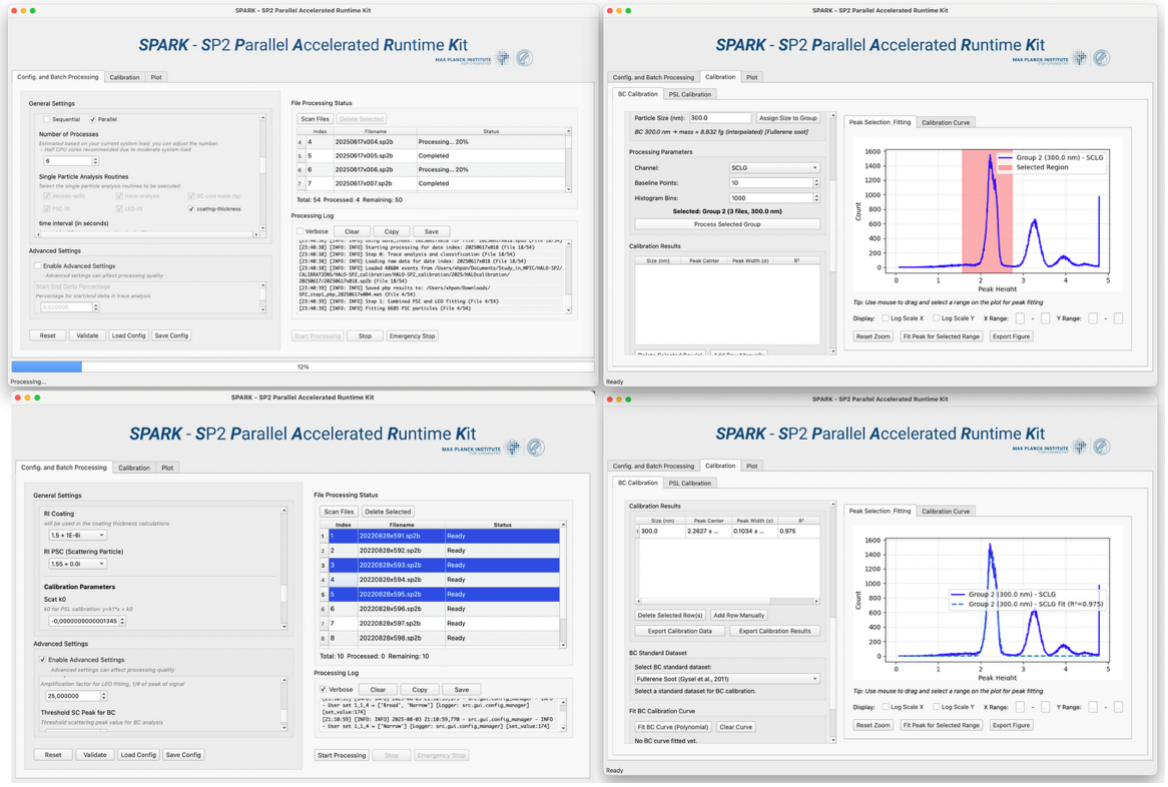

Figure 2.2. Screenshots of the SPARK graphical user interface on macOS. Left: The main window (Configuration tab) with the settings viewer and task progress monitor, showing ongoing processes and system status. Right: the calibration data processing tab.

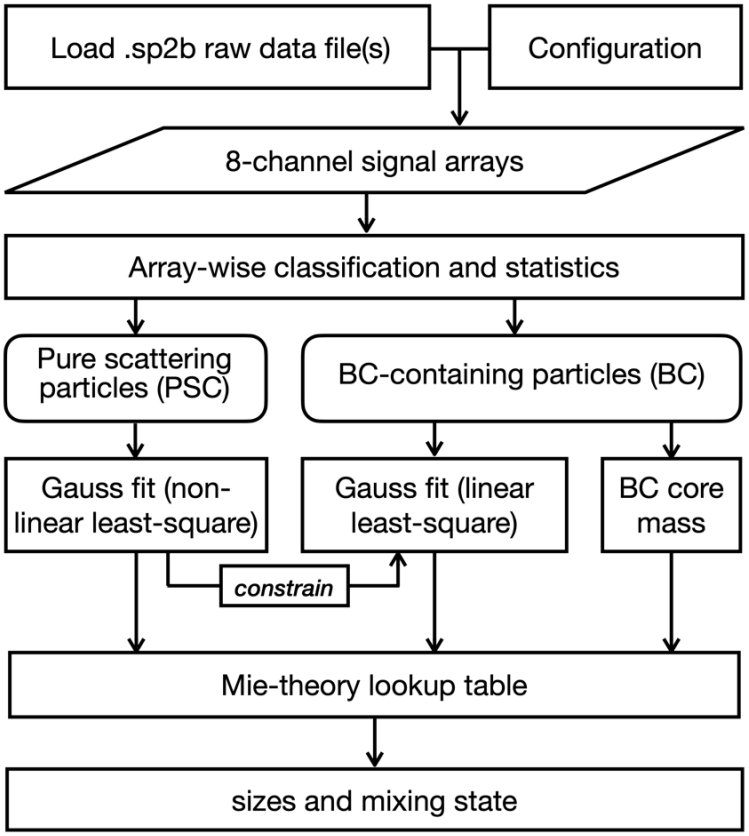

Figure 2.3: Schematic overview of the SPARK data processing workflow. Raw SP2 waveform files are loaded and decoded, then processed through each step: baseline subtraction, peak detection, particle classification (PSC vs. BC), signal reconstruction, size/mass retrieval, and finally the export of per-particle results and time-aggregated summaries.

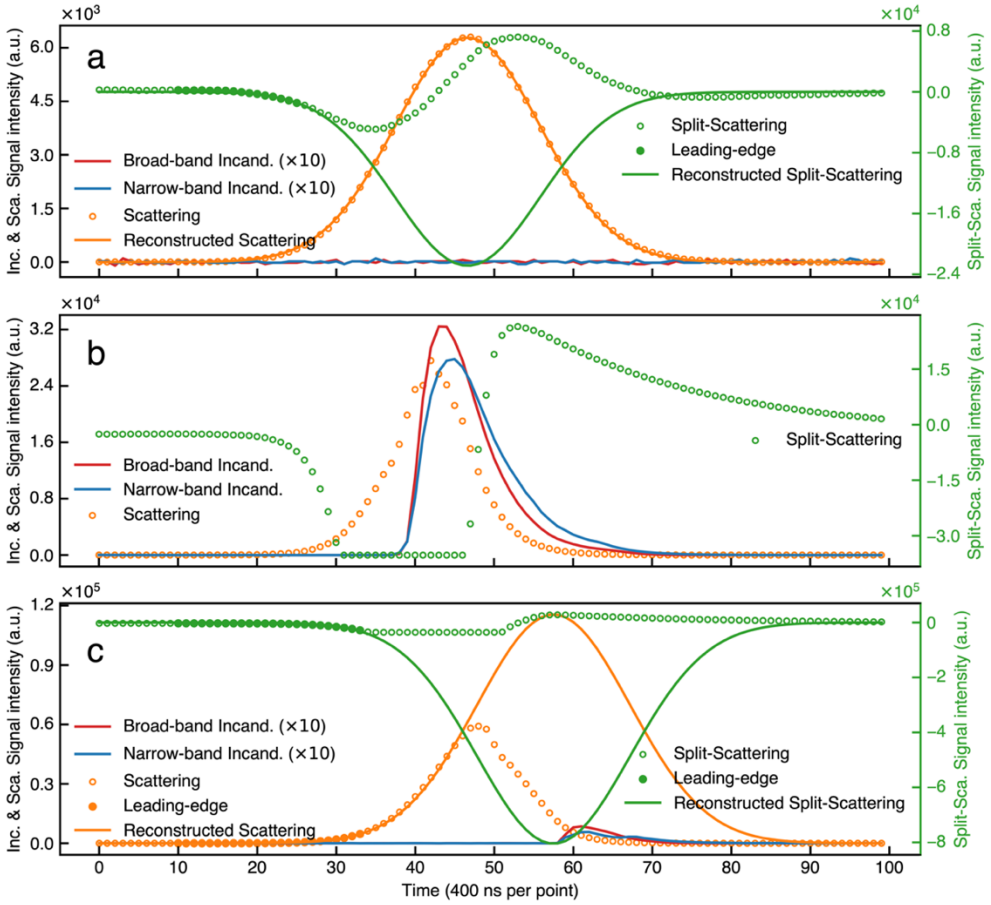

Figure 2.4: Example SP2 waveforms for three particle types – (a) a purely scattering particle (PSC), (b) an uncoated (bare) BC particle, and (c) a core–shell (coated) BC particle. The orange curve is the total scattering signal (SC detector); green is the split scattering signal (SP detector); red and blue are the narrowband and broadband incandescence signals (in panels a and c the incandescence signals are amplified for visibility). The left y-axis corresponds to scattering and incandescence intensity (arbitrary units), and the right y-axis corresponds to the SP detector's split signal.

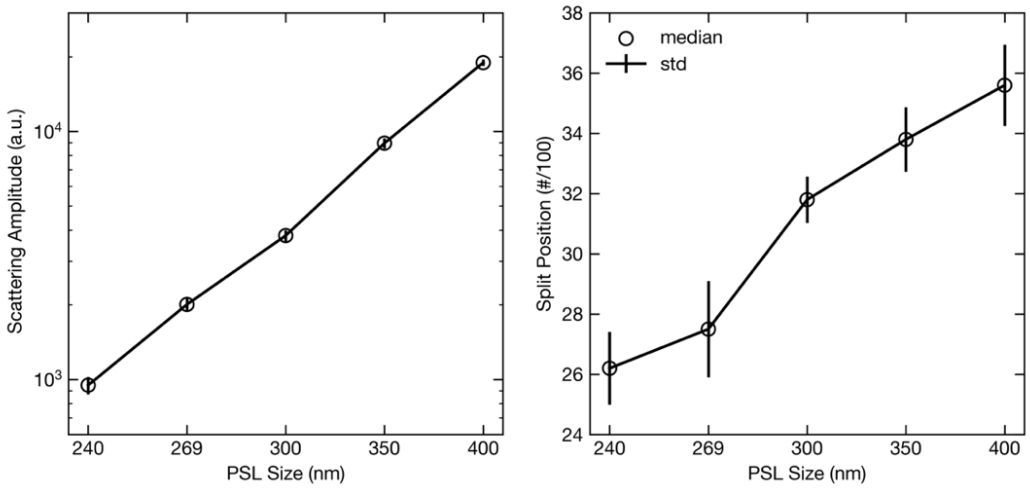

Figure 2.5: Dependence of split-position timing (t_{SP}) on particle size for polystyrene latex (PSL) spheres. The scatter plot shows that t_{SP} (delay between when the split detector triggers and the beam center) increases systematically with PSL diameter. Larger particles cross the fixed split-detector threshold later in time, resulting in a longer delay.

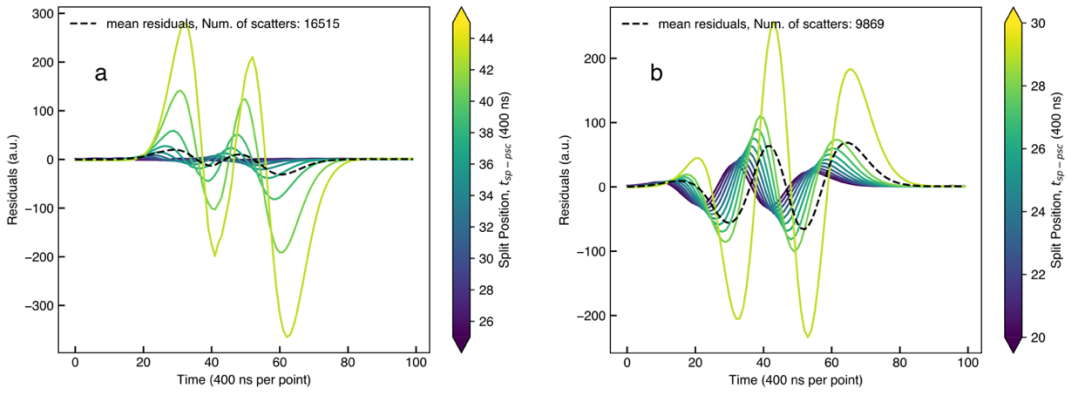

Figure 2.6: Mean residual profiles from the PSC Gaussian fitting, shown for two example data sets (panel a and panel b). In each panel, the black dashed line represents the average residual (difference between actual signal and Gaussian fit) across all particles in that data set. These two data sets come from separate field campaigns and were measured with different SP2 instruments, illustrating the consistency of the fitting performance across different conditions.

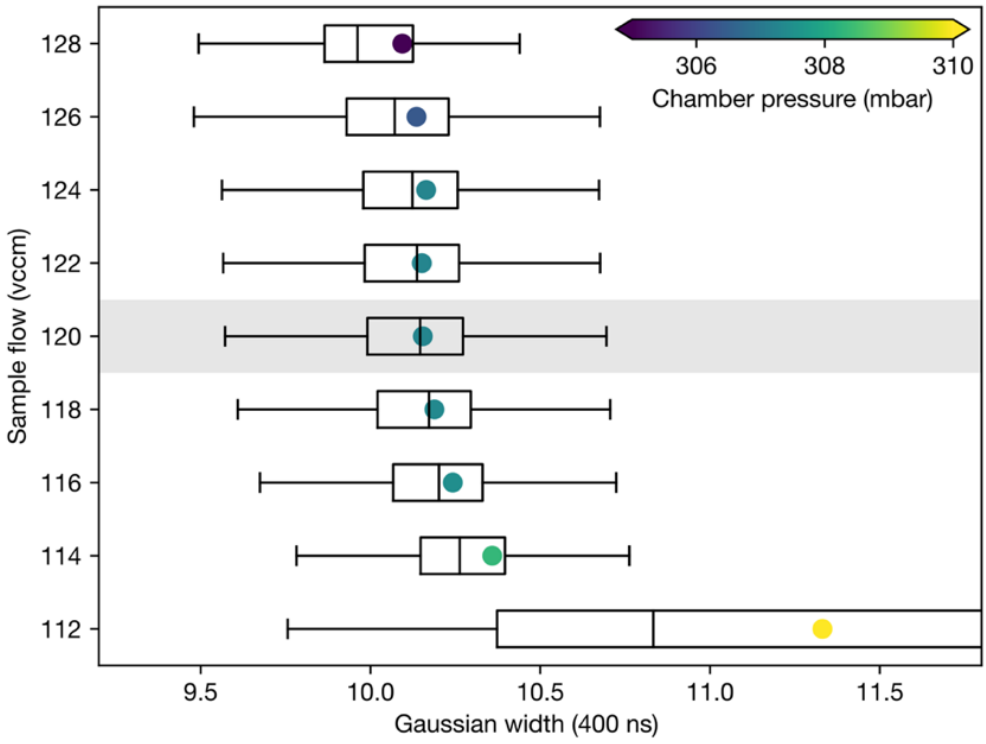

Figure 2.7: Distribution of fitted Gaussian widths (σ) under different SP2 sampling flow rates during ~12 hours of aircraft measurements. Each boxplot summarizes the σ values at a given flow rate setting; the shaded vertical band marks the nominal (preset) flow rate for the instrument. In each horizontal boxplot, the left edge, center line, and right edge correspond to the 25th percentile, median (50th percentile), and 75th percentile of σ, respectively. The "whiskers" extend to show the full range (min to max), and the overlaid dots mark the mean σ for each period. The dot colors indicate the SP2 chamber pressure for those measurements.

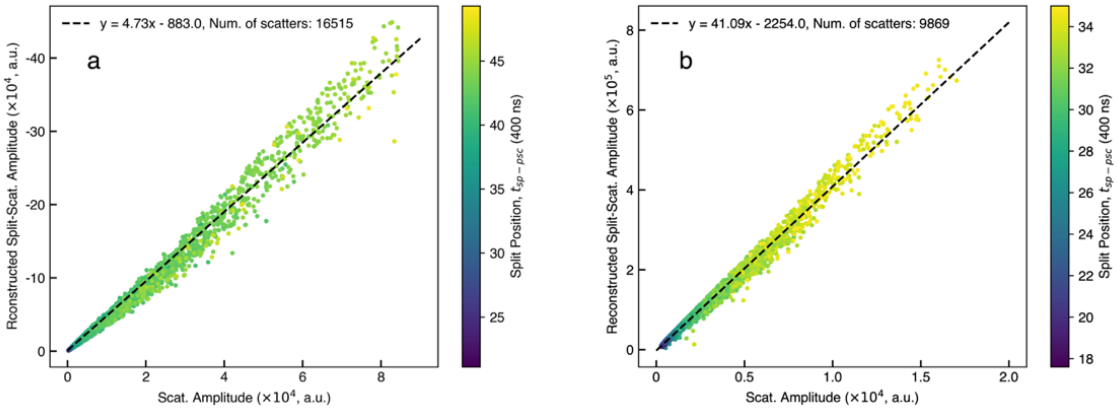

Figure 2.8: Correlation between the total scattering signal amplitude (x-axis) and the split-detector scattering amplitude (y-axis) for the two example data sets from Figure 3 (panels a and b). Each point is a particle; the point color indicates that particle's split-position timing (t_{SP}). The black dashed line in each panel is a linear fit to the data, illustrating the proportional relationship between the split detector signal and the total scattering signal.

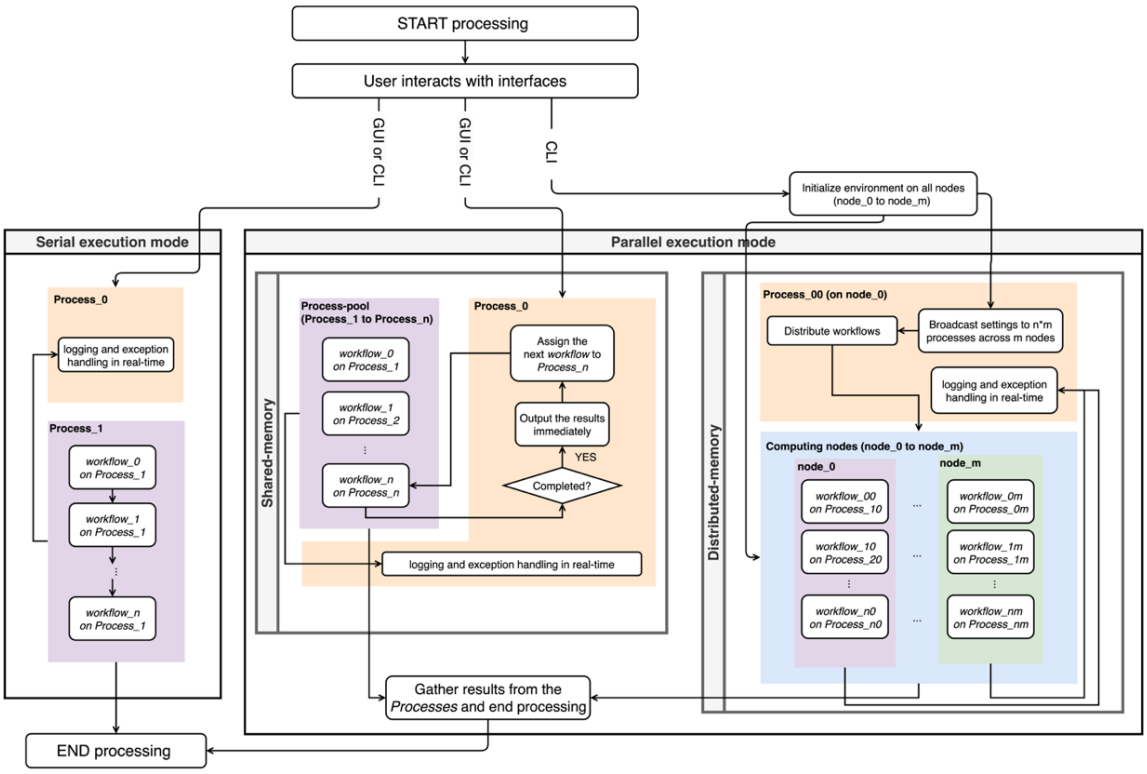

Figure 2.9: Comparison of Serial and Parallel Processing Architectures: Showcases a side-by-side visual comparison between the serial and parallel processing architectures in the data processor. The left segment depicts the serial execution mode with its sequential process flow, while the right segment highlights the parallel execution mode, demonstrating how tasks are distributed and processed concurrently, thus elucidating the operational differences and efficiencies between the two methods.

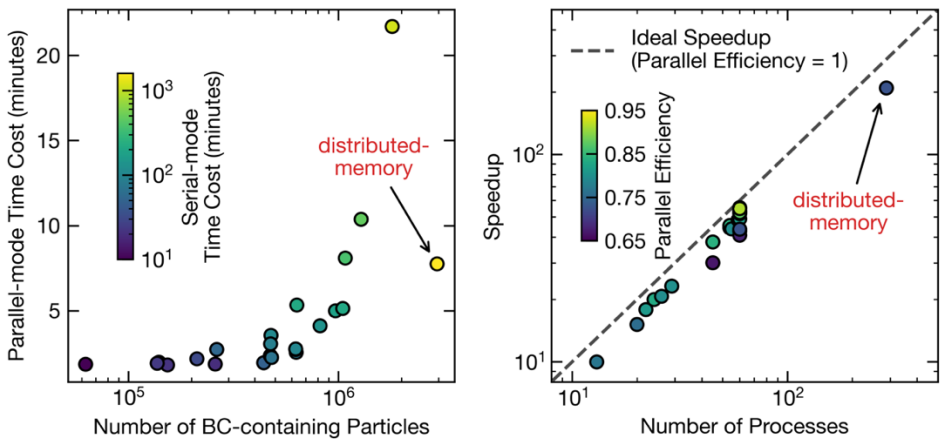

Figure 2.10: (a) Parallel-mode time cost as a function of the number of BC-containing particles, with colors indicating the equivalent serial-mode time cost. (b) Speedup versus the number of processes for each workload. Points are color-coded by parallel efficiency. The dashed line represents ideal speedup (efficiency = 1), while the red-labeled point highlights the distributed-memory benchmark. The annotated scatter denotes the result from the distributed-memory MPI execution across 288 processes.

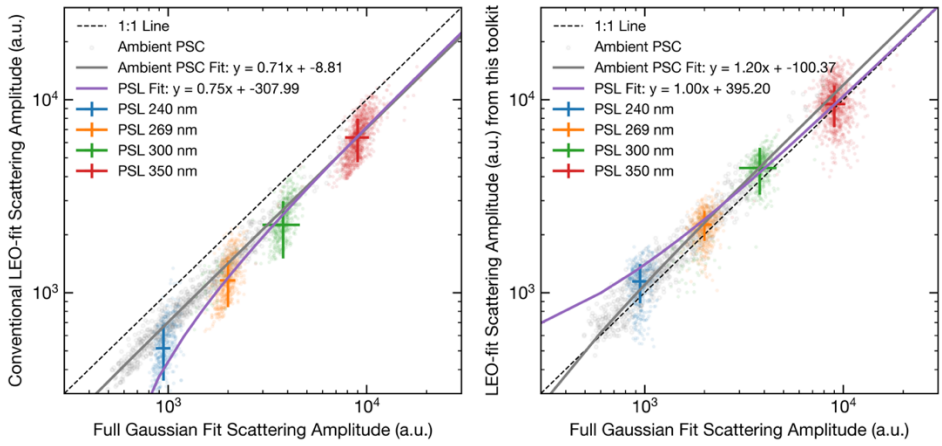

Figure 2.11: Comparison of two leading-edge-only (LEO) fit performance. Scatter of fitted vs. true scattering amplitudes for PSL standards (blue) and ambient PSC particles (orange) using (a) conventional SC-channel LEO and (b) SP-channel LEO. Dashed line: 1:1 reference; slopes and R^2 values annotated.

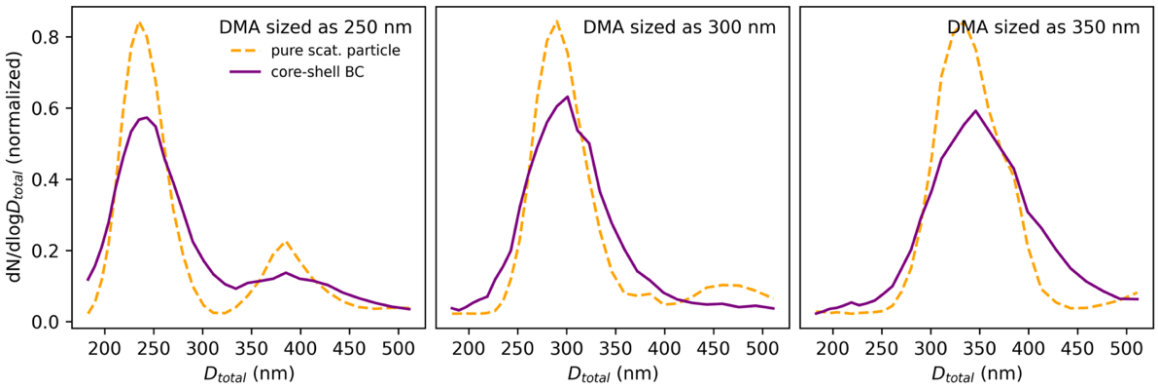

Figure 2.12. Normalized SP2-derived optical-diameter distributions (dN/dlogD_{total}), for DMA-selected monodisperse aerosols at 250, 300 and 350 nm (left to right). Dashed orange lines: purely scattering (PSC) calibration particles; solid purple lines: core–shell BC particles (lag-time ≥ 1.6 µs). Distributions were aggregated from four days of DMA scans from ambient measurement. Secondary peaks visible in some panels arise from multiply charged DMA transmission.

Appendix

This appendix provides details of the custom least-squares fitting routines introduced in Section 2.2, including the incorporation of an analytical Jacobian and the linear 'leading-edge-only' fit for BC particles.

A2.1. PSC-fit implementation

General-purpose curve-fitting functions (e.g., SciPy's curve_fit or fitting routines in MATLAB/Igor Pro) are very flexible, but that generality can be inefficient for our problem. We need to perform millions of fits, so we implemented a custom least-squares routine with an analytical Jacobian. By tailoring the routine to our specific use-case, we eliminate the overhead of a generic optimizer and gain robustness. In particular, providing an analytical Jacobian improves the convergence speed and stability for our repetitive calculations.

Let the observed scattering signal from the PSC particles on SC channel be $s_{SC_{PSC},i}$ at time points t_i. We fit the Gaussian model $g(t_i; A_{PSC}, \mu, \sigma)$ by minimizing the least-squares objective function:

$$L(A, \mu, \sigma) = \sum_{i=1}^{100} \left[s_{SC_{PSC},i} - g(t_i; A_{PSC}, \mu, \sigma) \right]^2 \quad (a1)$$

To minimize $L(A, \mu, \sigma)$, we use the Levenberg–Marquardt (L-M) algorithm for this optimization and supply it with an analytical Jacobian J_i:

$$J_i = \left[\frac{\partial g}{\partial A}, \frac{\partial g}{\partial \mu}, \frac{\partial g}{\partial \sigma} \right]_{t=t_i}$$
$$= \left[exp\left(-\frac{(t_i - \mu)^2}{2\sigma^2} \right), \frac{A(t_i - \mu)}{\sigma^2} exp\left(-\frac{(t_i - \mu)^2}{2\sigma^2} \right), \frac{A(t_i - \mu)^2}{\sigma^3} exp\left(-\frac{(t_i - \mu)^2}{2\sigma^2} \right) \right] \quad (a2)$$

Where J_i represents the partial derivatives of the Gaussian function with respect to A, μ, σ at time t_i. Including this exact Jacobian (instead of having the algorithm approximate derivatives) makes the fitting both faster and more stable (Figure S2 shows the performance improvement).

A2.2. LEO-fit implementation

Reconstructing a BC particle's scattering signal via LEO fitting ultimately comes down to finding one parameter: the best-fit scattering amplitude A_{BC} (the Gaussian's peak height) that matches the signal's leading-edge. In principle this is a simple linear least-squares problem, but many standard fitting routines still approach it with heavier machinery than necessary. For instance, SciPy's curve_fit will by default treat it like a non-linear problem and run an iterative solver (Levenberg–Marquardt), even though only one linear parameter is being determined (Virtanen

et al., 2020). MATLAB and Igor Pro solve linear least-squares more directly (using matrix techniques like QR decomposition or singular value decomposition, SVD; MathWorks, 2023; WaveMetrics, 2024), but those still carry overhead from handling matrices and are not designed for millions of repetitive fits in our case.

We derive a closed-form formula for the optimal amplitude instead of any iterative optimization that is time-consuming. For a BC-containing particle, the modeled scattering signal can be written as:

$$g_{BC}(t_i; A_{BC}, \mu_{BC}, \sigma) = A_{BC} \cdot \exp\left(-\frac{(t_i - \mu_{BC})^2}{\sigma^2}\right) + w_i(t_{SP}) \tag{a4}$$

Here, the σ and $w_i(t_{SP})$ are both derived from fitting PSC particles, while the BC particle's center time μ_{BC} is inferred from the split-position t_{SP} plus the delay Δt_{SP} (which is independent of the particle and also derived from fitting PSC) (Gao et al., 2007). Substituting the σ, μ_{BC} and $w_i(t_{SP})$ values and give discrete signal data points, Gaussian function for BC particles is simplified as:

$$g_{BC,i}(\mathrm{A}_{BC}) = A_{BC} \cdot \varepsilon_i + w_i \tag{a5}$$

where the $\varepsilon_i = \exp(-\frac{(t_i-\mu_{BC})^2}{\sigma^2})$ represents the known, normalized Gaussian shape, and w_i derived from PSC fitting, dependent on t_{SP} (Gao et al., 2007).

The objective of the LEO-fit is to find the amplitude A_{BC} that best matches the observed scattering data points in the leading-edge region $s_{LEO,i}$. Similar to equation (a1) the discrete least-squares loss function becomes:

$$L_{LEO}(A_{BC}) = \sum_{i=1}^{M} \left[s_{LEO,i} - (A_{BC} \cdot \varepsilon_i + w_i)\right]^2 \tag{a6}$$

where M is the number of valid data points on the leading-edge. Subtracting the w_i from the observed scattering data before fitting with $s'_{LEO,i} = s_{LEO,i} - w_i$ and the loss function is simplified into a purely amplitude-linear problem:

$$L_{LEO}(A_{BC}) = \sum_{i=1}^{M} \left[s'_{LEO,i} - A_{BC} \cdot \varepsilon_i)\right]^2 \tag{a7}$$

Then, the loss function is expressed in matrix notation as:

$$r(\boldsymbol{A}_{LEO}) = \| \boldsymbol{E}_{LEO} A_{LEO} - \boldsymbol{S}'_{LEO} \|_2^2 \tag{a8}$$

Where, $\boldsymbol{E}_{LEO}$ represents vector of Gaussian shape $(\varepsilon_1, \varepsilon_2, \cdots, \varepsilon_M)^T$, $\boldsymbol{S'}_{LEO}$ represents vector of corrected leading-edge signals $\left(s'_{LEO,1}, s'_{LEO,2}, \cdots, s'_{LEO,M}\right)^T$. Expanding $(a8)$ yields:

$$r(A_{LEO}) = \boldsymbol{A}_{LEO}^T \boldsymbol{E}_{LEO}^T \boldsymbol{E}_{LEO} A_{LEO} - 2\boldsymbol{S'}_{LEO}^T \boldsymbol{E}_{LEO} A_{LEO} + \boldsymbol{S'}_{LEO}^T \boldsymbol{S'}_{LEO} \quad (a9)$$

The gradient of the objective function ∇r (with respect to A_{LEO}) is then computed as:

$$\nabla r = \frac{\partial r}{\partial A_{LEO}} = 2\boldsymbol{E}_{LEO}^T \boldsymbol{E}_{LEO} A_{LEO} - 2\boldsymbol{E}_{LEO}^T \boldsymbol{S'}_{LEO} \quad (a10)$$

Setting $\nabla r = 0$ to find the global minimum gives the closed-form solution:

$$2\boldsymbol{E}_{LEO}^T \boldsymbol{E}_{LEO} A_{LEO} - 2\boldsymbol{E}_{LEO}^T \boldsymbol{S'}_{LEO} = 0 \quad (a11)$$

Solving for A_{LEO} yields:

$$A_{LEO} = (\boldsymbol{E}_{LEO}^T \boldsymbol{E}_{LEO})^{-1} \boldsymbol{E}_{LEO}^T \boldsymbol{S'}_{LEO} \quad (a12)$$

This result is simply the one-parameter least-squares formula (Boyd & Vandenberghe, 2004). It requires only basic vector operations—no iterations or heavy matrix factorizations—so it significantly reduces computation and is numerically robust.

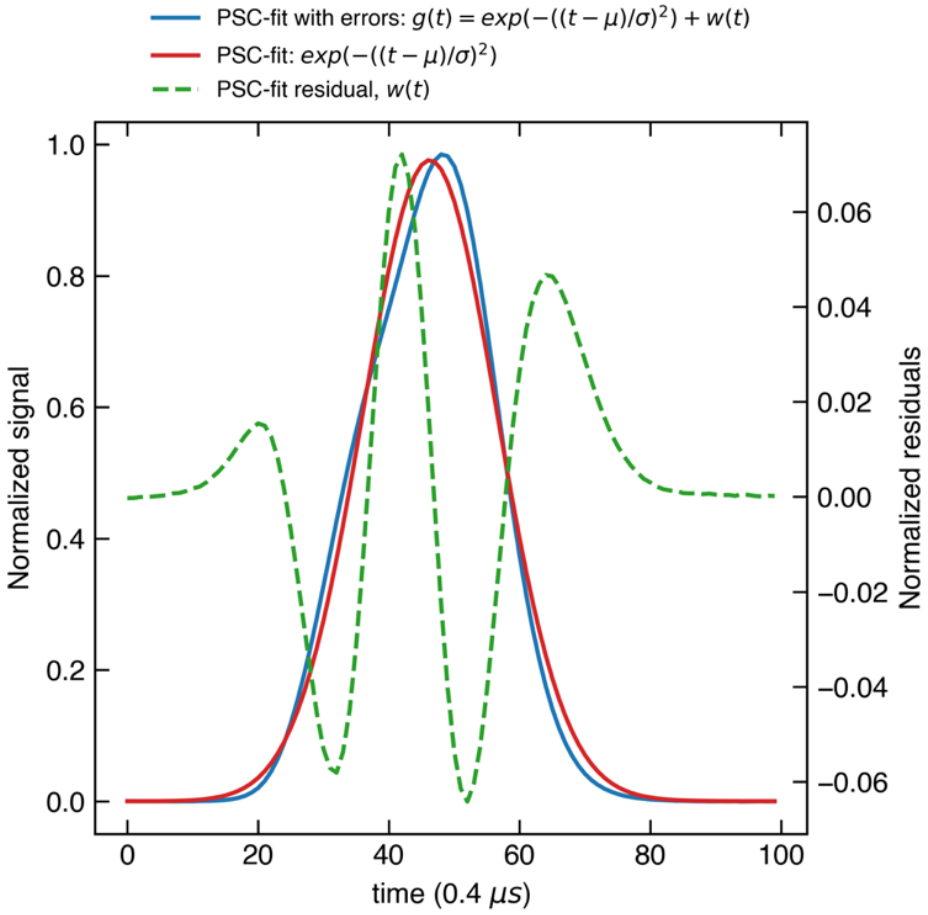

Figure S2.1: Illustration of the PSC Gaussian-fit model and its residual. The observed scattering waveform (blue) can be described as a Gaussian term (red) plus a small systematic residual (green dashed, right-hand axis). The residual peaks at ≈ 6 % of the normalized signal, demonstrating minor deviations from an ideal TEM_{00} beam profile.

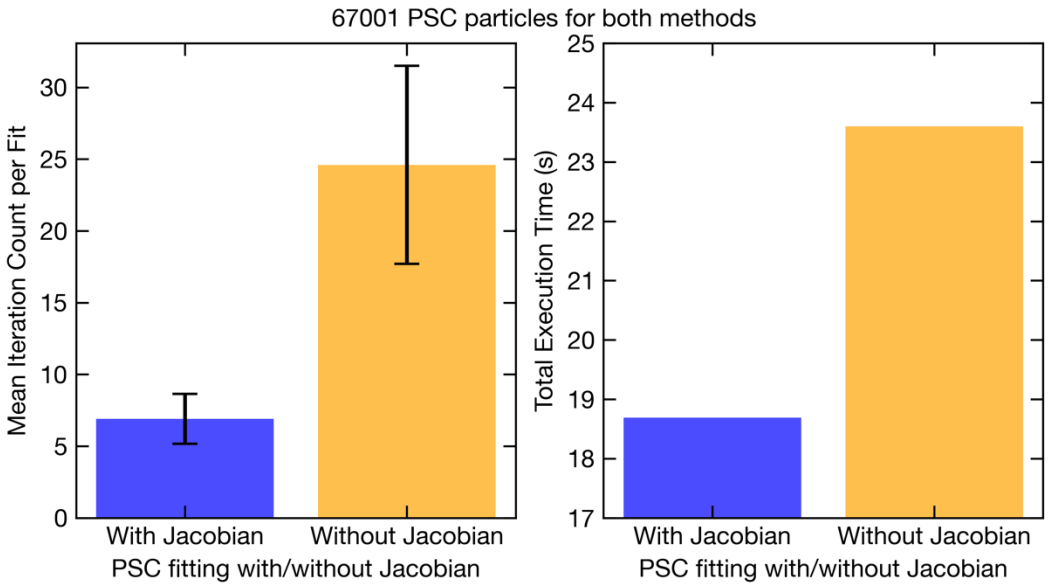

Figure S2.2: Performance comparison of the least-squares routine with (blue) and without (yellow) analytical Jacobian. Bar chart showing mean iteration count and total runtime for fitting 60 000 PSC particles, demonstrating ~30 % speed-up when using the Jacobian.

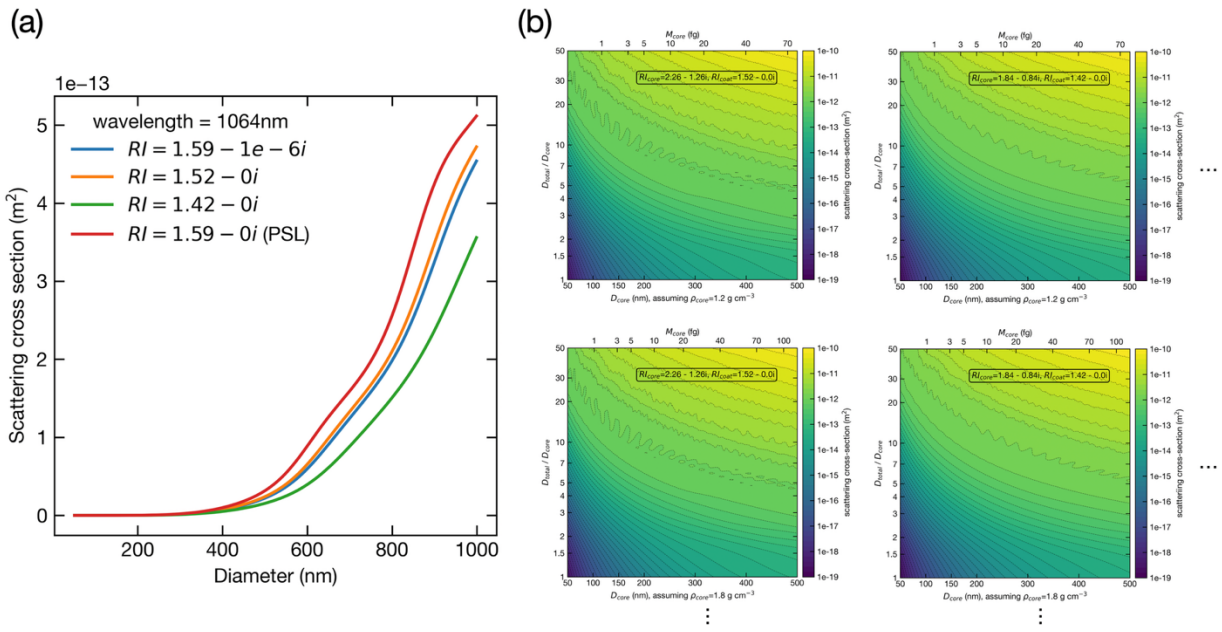

Figure S2.3: Mie-theory-based scattering calculations relevant to SP2 analysis, calculated at a wavelength of 1064 nm. (a) Scattering cross-sections of spherical particles, curves correspond to different refractive indices (RI), including polystyrene latex spheres (RI_{PSL} = 1.59–0i) and several non-absorbing and weakly absorbing materials. (b) Contours illustrating relationships between BC particle mass (top x-axis), BC core diameter Dcore (bottom x-axis), and the ratio of total diameter to core diameter Dtotal/Dcore (y-axis), assuming a spherical core–shell morphology. The upper panels assume a BC core density of 1.2 g cm^{-3}, while the lower panels assume a density of 1.8 g cm^{-3}. Color scales indicate calculated scattering cross-sections. The refractive indices used for these calculations correspond to different combinations of core and coating materials.

„

Chapter 3 Black Carbon in the Marine Atmosphere: Concentration and Mixing State from Coastal to Remote Atlantic Regions

This work is submitted as Pan et al. (2025):

Xihao Pan, Yuxuan Zhang, Chaoyang Xue, Uwe Kuhn, Isabella Hrabe de Angelis, Christopher Pöhlker, Jeannine Ditas, Lena Heins, Hedy M. Aardema, Hans A. Slagte, Maria Ll. Calleja, Antonis Dragoneas, David Walter, Björn Nillius, Qiaoqiao Wang, Nan Ma, Hang Su, Ulrich Pöschl, Gerald H. Haug, Ralf Schiebel, Yafang Cheng: Black Carbon in the Marine Atmosphere: Concentration and Mixing State from Coastal to Remote Atlantic Regions, Journal of Geophysical Research: Atmospheres, 2025

I am the first-author of this work and my contribution to this work includes maintaining and calibrating the instruments, organizing and analyzing the data, making the figures and tables, discussing the results, interpretation and drafting the manuscript.

The following text, figures, and tables quoted (within "") from page 44 to page 71 are the same as the manuscript which is cited on page 43.

"

Abstract

Black carbon (BC) from maritime emissions plays a critical role by influencing radiation, cloud processes, and atmospheric dynamics in the marine atmosphere. These impacts depend on BC concentration and mixing state with other aerosol components. However, in-situ observations of BC over oceans remain scarce, and the influence of the marine environment on the evolution of BC mixing state is not well understood. Here, we present shipborne measurements of BC concentration and mixing state using a Single Particle Soot Photometer (SP2) aboard the research sailing yacht S/Y Eugen Seibold during ten Atlantic Ocean cruises. The dataset spans 1120 of measurement hours from near-coastal zones a few tens of kilometers from land to remote ocean areas up to a thousand kilometers offshore. In oceanic regions extending from tens to thousands of kilometers offshore, 1-minute averaged BC concentrations were typically around 100 ng m^{-3}, suggesting a background level shaped by the well-mixed Atlantic marine atmosphere. Despite the relatively small variability in BC mass concentrations, the mixing state of BC exhibits substantial differences between nearshore and remote oceanic regions. High number fractions (>50%) of BC particles without core-shell morphologies, characterized by BC externally attached to non-BC materials, were observed in near-coastal regions and decreased to ~20% in remote oceanic regions. In ship-impacted regions, small freshly emitted BC particles tend to coagulate with other aerosol particles and forming non-core-shell attached structures, while high relative humidity (RH >85%) tends to promote the formation of thick coatings. Our results provide new insights into climate-relevant properties and underscore the importance of coagulation and hygroscopic processing for the mixing state of BC in the marine atmosphere.

Plain Language Summary

Uncertainty in estimating black carbon (BC)-induced climate warming remains high due to debates over the role of BC mixing state in light absorption. According to Mie theory, when BC is coated by other materials in a "core-shell" structure, it can absorb more sunlight through a "lensing effect". However, whether such structures actually form, especially over the ocean, is largely unknown. The marine atmosphere, characterized by high humidity, low precursor levels, abundant marine aerosols, and strong air-sea turbulence, may drive distinct BC aging pathways. Our study shows that fresh BC in marine environments tends to form non-core-shell attached structures through coagulation with aerosol particles/droplets, especially near coastal regions, likely driven by wave-induced turbulence. Although low precursor levels constrain condensation and multiphase reactions, high humidity over the ocean can promote hygroscopic growth, transforming BC particles that attach with marine aerosol (e.g., sea salt) into thickly coated core-shell particles. This suggests that marine shaping of BC mixing states can significantly enhance its light absorption, thereby amplifying its impact on the marine climate.

3.1 Introduction

Black carbon (BC) is an important light-absorbing component of atmospheric aerosols and is widely recognized as a significant short-lived climate-warming agent (Bond and Bergstrom, 2006; Ramanathan and Carmichael, 2008). Produced through incomplete combustion of fossil fuels, biofuels, and biomass etc., BC not only absorbs sunlight, thereby contributing to atmospheric warming, but also influences cloud processes (Bond et al., 2013). The overall radiative effects of BC depend not just on its concentration, but also on its microphysical properties, including its size, shape, and mixing state. Here, “mixing state” refers to the extent to which BC particles are mixed with other aerosol constituents formed or acquired during atmospheric aging processes such as condensation, coagulation, and multiphase reactions (Zhang et al., 2023). Changes in the mixing state can significantly alter the optical properties, hygroscopicity, ice nucleation (IN) activity and lifetime of BC, making it more difficult to quantify its climate effect (Bond et al., 2013; Cheng et al., 2012; Kärcher, 2018). An improved understanding of the climatic impact of BC requires more comprehensive observational constraints to enable accurate representation of BC mixing states under real atmospheric conditions in models (Zhang et al., 2025).

To elucidate the impact of BC aerosols on marine climate, increasing efforts have been devoted to in situ measurements of BC in marine environments. According to Bond et al. (2013) , marine shipping contributes approximately 2% of global BC emissions; however, it may account for a disproportionately larger share of direct BC emissions in remote regions. Marine regions, characterized by their vast spatial extent, relatively pristine atmospheric conditions, limited local emissions, and high-albedo surfaces (e.g., sea ice and cloud cover), are particularly susceptible to BC-induced radiative forcing, thereby amplifying the climatic significance of BC in these areas (Bond and Bergstrom, 2006; Ramanathan and Carmichael, 2008). Current online observations of BC in marine environments have predominantly focused on quantifying atmospheric BC concentrations. These measurements indicate that background BC levels in marine environments are substantially influenced by shipping activity. In regions with high shipping density, BC concentrations typically range from tens to several hundred nanograms per cubic meter (ng m^{-3}) (Buffaloe et al., 2014; Diesch et al., 2013). In contrast, in remote open-ocean areas such as the Arctic, BC concentrations are generally limited to a few ng m^{-3}, and in some instances, fall below 1 ng m^{-3} (Deng et al., 2024; Katich et al., 2018; Taketani et al., 2016; Zanatta et al., 2018).

Compared to concentration measurements, observations of BC mixing state in marine environments remain sparse. Taketani et al. (2016) conducted shipborne measurements in the Arctic Ocean and reported the presence of BC particles coagulated with sea salt and other marine aerosols via coagulation processes, forming so-called "attached BC." However, few studies have examined the processes driving changes in BC mixing state, with most focusing on urban pollution conditions or biomass-burning plumes (Peng et al., 2016). The current understanding of how marine environments influence BC mixing state is still limited, posing a

significant challenge to the accurate representation of BC mixing state and their radiative effects in atmospheric models.

In this work, we conduct shipborne measurements of BC particles across the Atlantic Ocean to explore the influence of the marine environment on the BC mixing state. We compare the characteristics of BC under different marine conditions in coastal and remote ocean regions, highlighting the important roles of vessel density, BC particle size, and relative humidity (RH) in shaping the BC mixing state in the marine atmosphere. Our study reveals the transformation of the BC mixing state during long-range (nearly thousand-kilometer) atmospheric transport over the ocean. The findings suggest that the formation of thickly coated BC in the marine environment is mainly governed by coagulation and hygroscopic growth, rather than the condensation of secondary aerosol components onto BC surfaces. This study not only provides new observational data on BC mixing states over the ocean but also offers a novel perspective on the formation mechanisms of core-shell structured BC in the atmosphere.

3.2 Materials and Methods

3.2.1 The S/Y Eugen Seibold

This study utilized data collected during oceanic cruises aboard the S/Y Eugen Seibold, a 72-foot research yacht specifically designed for sampling of air, seawater, and plankton (Aardema et al., 2024; Schiebel et al., 2024). Atmospheric measurements were conducted onboard as indicated in Fig. S3.1. The inlet system is mounted approximately 13 m above the waterline, with a flexible glass-epoxy tube (outer diameter 60 mm, inner diameter 56 mm) shielding a bundle of smaller inlet tubes (for both aerosol and gas sampling) from direct sunlight and the corrosive marine environment (Fig. S3.1a and Fig. S3.1b). Further technical details on air and water sampling configurations on board the S/Y Eugen Seibold are provided by Schiebel et al. (2024).

3.2.2 The black carbon measurement

BC measurements collected during ten cruises conducted between February 2022 and January 2023 in the Atlantic Ocean, extending from temperate Bremerhaven, Germany (55°N, 8.5°E) to St. George's, Grenada (12°N, 61°W), in the tropical ocean (Fig. 3.1 and Fig. S3.2). Refractory BC (rBC) aerosols were characterized using a Single Particle Soot Photometer (SP2). The SP2 sampled 0.12 L min^{-1} of dried air from the shared inlet system, which also served several other instruments drawing a combined total of 3.72 L min^{-1} (Fig. S3.1c). The transmission efficiency as a function of particle size was calculated using the Particle Loss Calculator (Weiden et al., 2009). For particles in the size range of 80-500 nm, particle losses within the inlet system were found to be less than 10% (Fig. S3.3), and the dataset was corrected accordingly.

The SP2 uses laser-induced incandescence (LII) to measure the mass of rBC cores within individual particles. When a BC-containing particle passes through the focused 1064 nm laser beam, the rBC core absorbs energy and is rapidly heated to incandescence (~4000 K), emitting

thermal radiation that is detected as the incandescence signal. Simultaneously, elastic light scattering from the entire particle, including both the rBC core and any associated non-refractory material, is measured (Moteki and Kondo, 2007; Schwarz et al., 2006; Stephens et al., 2003). Here, the rBC specifically refers to the BC cores quantified by LII in SP2 measurements, and all references to measured BC in this study refer to this rBC component (Petzold et al., 2013). Calibrations of the SP2 were conducted during and after these cruises to ensure consistency and instrument stability. The relationship between electrical mobility diameter and incandescence signal intensity was established using size-classified fullerene soot particles (stock 40971, lot L20W054, Alfa Aesar, USA), with soot densities at different diameters adapted from Gysel et al. (2011). The scattering signal response was calibrated using standard polystyrene latex (PSL; Thermo Fisher) spheres. Both particle types were first size classified using a differential mobility analyzer and then introduced into the SP2. Assuming spherical geometry and a constant material density of 1.8 g cm^{-3}, the mass-equivalent diameter of the rBC core was derived. Throughout this study, we refer to this mass-equivalent diameter simply as "core size" (D_{core}).

In this study, the mixing state of BC-containing particles was assessed by both "lag-time" method and "leading-edge-only (LEO)-fit" method (Gao et al., 2007; Moteki and Kondo, 2007; Zhang et al., 2018a). The "lag-time" method is defined as the temporal offset calculated as the time of the incandescence peak minus the time of the scattering peak (Moteki and Kondo, 2007). This method is commonly used to distinguish between "thickly coated" and "thinly coated or bare" BC particles based on their thermal response to laser heating in SP2 measurements. For BC-containing particles with core-shell structures, lag-times are typically positive because the non-refractory coating material evaporates prior to the incandescence of the rBC core, resulting in a delayed incandescence peak relative to the scattering peak. BC-containing particles with shorter lag-times (typically 0-2 μs) are generally classified as bare or thinly coated. Threshold values used to define "thickly coated" particles vary slightly from 1.6 μs to 2.0 μs, depending on the specific SP2 instrument and particle properties (Dahlkötter et al., 2014; Ko et al., 2020; Moteki and Kondo, 2007; Subramanian et al., 2010; Zhang et al., 2016).

However, BC-containing particles with non-core-shell structures can exhibit distinct thermal behaviors in the laser beam, resulting in negative lag-times in SP2 measurements, where the incandescence peak precedes the scattering peak (Fig. S3.4). During SP2 measurement, BC-containing particles are exposed to a 1064 nm laser beam. If rBC incandesces before reaching the beam center, while the scattering signal of the residual particle still shows a peak at the beam center, it indicates that the rBC is externally attached to non-BC material rather than internally mixed. Negative lag-times have also been reported in field studies (Dahlkötter et al., 2014; Ko et al., 2020; Sedlacek et al., 2012; Taketani et al., 2016).

We categorize representative lag-time patterns for both positive and negative lag-times in the Fig. S3.4. Notably, we also observed twin-peak features in both incandescence and scattering signals, similar to those reported by Moteki and Kondo (2007) and Sedlacek et al. (2015). To exclude the possibility of mechanical issues contributing to multiple peaks, the laser beam profile was verified to be TEM_{oo} using a Mightex camera (Fig. S3.5). To minimize ambiguity in

lag-time determination, all lag-times were calculated based on the maximum peak positions of the scattering and incandescence signals (Moteki and Kondo, 2007).

For those BC with positive lag-times (>0 μs), we further estimated their coating thickness using LEO-fit method (Gao et al., 2007). In this approach, the particle position relative to the laser center is derived from the split-scattering signals, and the Gaussian width of the laser beam is measured using pure-scattering particles (Ditas et al., 2018; Gao et al., 2007). In this study, LEO-fit is applied to both the scattering and split-scattering signals (Schwarz et al., 2015; Yuan et al., 2020), as the split-scattering signals exhibit a higher signal-to-noise ratio (SNR) due to detectors' characteristics. In the SP2 instrument used in this study, the gain of the split-scattering detector is approximately 40 times higher than that of the scattering detector. This ratio was estimated by applying LEO-fit to both signals from pure-scattering particles and it remains stable because it depends solely on the inherent characteristics of the detectors (Schwarz et al., 2015). A higher SNR is advantageous for LEO-fit, as beyond 1-5% of the peak laser intensity the scattering signal may become biased due to the evaporation of non-BC material (Gao et al., 2007; Metcalf et al., 2012; Taketani et al., 2016). Therefore, in the leading-edge signal, data points with higher SNR are considered more reliable; otherwise, the signal may be obscured by noise, increasing the likelihood of inaccurate reconstruction of the scattering peak height during Gaussian fitting.

3.2.3 Vessel density, distance to shoreline and meteorological parameters

To support our analyses, we incorporated monthly vessel density data as a proxy for local shipping activity. These data are sourced from the Global Maritime Traffic Density Service, GlobalMaritimeTraffic.org (GMTDS, 2024), which compiles Automated Identification System (AIS) datasets into georeferenced raster files. Each raster provides aggregated monthly vessel traffic intensity (hours per km^2 per month) at a specified spatial resolution (e.g., kilometers per pixel). In this study, for each measurement point, we selected the raster corresponding to the cruise month, transformed the coordinates into the same reference system as the raster, and extracted grid cells within a 5 km radius. We then computed the average vessel density over this region to obtain a local indicator of maritime traffic. In addition, we calculated the minimum distance from each ship coordinate to the nearest coastline using the 10 m resolution Natural Earth shoreline dataset. Assigning these vessel density and distance-to-shoreline values to each sampling instance enabled us to distinguish regions with high shipping activity (and thus likely fresher BC emissions) from those where BC may be more regionally or remotely influenced.

We also monitored CO2 concentrations and recorded standard meteorological parameters (e.g., temperature, RH, wind speed, wind direction) onboard. Details on the measurement setup, calibration procedures, and data quality controls are provided in the supplementary information and in related references (Schiebel et al., 2024).

3.3 Results and Discussion

3.3.1 Marine traffic density and BC concentration

During the ten Atlantic Ocean cruises (Fig. 3.1a and Fig. S3.2), vessel density in the observed ocean regions spanned five orders of magnitude (10^{-2}-10^{3} hours km^{-2} month^{-1}, Fig. 3.1b), providing a robust representation of the impact of shipping activities on the marine environment. As shown in Fig. 3.2, the probability density function (PDF) of vessel density within the observed regions exhibits a bimodal distribution. Our observations were predominantly conducted in ocean areas with vessel densities below 1 hour km^{-2} month^{-1}, located tens to thousands of kilometers offshore. In contrast, observation areas with vessel densities exceeding 1 hour km^{-2} month^{-1} were primarily concentrated within 50 km of the coastline. In this study, we classify the marine environment into two distinct regimes for statistical analysis of our measurements: regions with vessel densities greater than 1 hour km^{-2} month^{-1}, representing areas heavily influenced by anthropogenic activities, and regions with vessel densities less than 1 hour km^{-2} month^{-1}, reflecting relatively clean remote marine environments.

Similar to vessel density, BC concentrations in the observed ocean regions span five orders of magnitude from 10^{-1} to 10^{4} ng m^{-3} (Figs. 3.1c, 3.3 and 3.4). Where vessel density exceeds 1 hour km^{-2} month^{-1}, the highest BC concentrations can reach 10^{3} to 10^{4} ng m^{-3}. However, across different vessel density regimes, the PDFs of 1-minute averaged BC mass concentrations consistently exhibit a peak around 100 ng m^{-3} (Fig. 3.4), suggesting a characteristic marine background level shaped by the well-mixed atmosphere over oceanic regions from tens to a thousand of kilometers offshore. In summary, vessel density primarily affects the high values of BC concentrations in the marine environment, while the transport of clean marine air masses can influence the background levels of BC concentrations over distances of several hundred kilometers across the ocean.

Figure 3.5 shows BC core size distribution under different marine environments. In the high shipping activity regime (vessel density >= 1 hour km^{-2} month^{-1}), BC core size exhibits a concentration-dependent pattern: (1) in near-coastal areas and busy shipping lanes with elevated BC levels (>300 ng m^{-3}), , the cores are relatively small, with a number median diameter (NMD) of ~80 nm and a mass median diameter (MMD) of ~110 nm, consistent with freshly emitted fossil fuel BC (Cappa et al., 2014; Zhang et al., 2020), indicating dominance of local shipping emissions; (2) in contrast, in marine environments influenced by oceanic air masses but with similar shipping activity and lower BC concentrations (<300 ng m^{-3}), the BC cores remain larger (MMD ~150 nm) and invariant with concentration, suggesting aging processes such as coagulation contribute to particle growth. On the other hand, in remote oceanic environments with low shipping activity (vessel densities <1 hour km^{-2} month^{-1}), BC particles exhibit a relatively large core size, with an MMD of approximately 180 nm. This observation indicates that prolonged atmospheric transport in the marine environment enhances the BC core size, likely driven by coagulation processes over extended timescales.

Notably, in remote areas with lower vessel density (< 1 hour km^{-2} $month^{-1}$), the BC core size distribution remains unaffected by BC concentration, even when concentrations exceed 300 ng m^{-3}, highlighting that long-range transport, rather than local emissions, predominantly governs BC characteristics in these remote marine regions.

3.3.2 BC-containing particles with non-core-shell structures

In the marine environment, a substantial fraction of BC-containing particles exhibits non-core-shell structures (Fig. 3.1d), as identified through lag-time distributions from SP2 analysis. Laboratory and field studies have reported that some BC-containing particles measured by SP2 exhibit negative lag-time, likely due to the coagulation of pure BC with non-BC particles, which could be relevant to source attribution and aging (Moteki et al., 2014; Moteki and Kondo, 2007; Sedlacek et al., 2012; Taketani et al., 2016). Near sources, high particle number concentrations and limited secondary formation likely promote coagulation of nearly bare BC with non-BC material, producing negative-lag signatures. Sedlacek et al. (2012) reported high negative-lag fractions (>0.6 μs) in near-surface wildfire plumes over Long Island. With transport and aging, the negative-lag fraction is lower but persists: Dahlkötter et al. (2014) found ~5% negative lag times in aged biomass-burning plumes at high altitudes; Moteki et al. (2014) reported "attached-BC" in Tokyo urban air, with fractions typically <10% and short episodes up to ~40%. Ko et al. (2020) also reported negative lag-time over California's coastal regions with a number fraction of ~2%. Taketani et al. (2016) identified a distinct -3 μs mode comprising ~20% of refractory BC during Arctic shipborne measurements. Similarly, our marine observations frequently detected attached-BC particles with negative lag-times.

The BC-containing particles with negative lag-times observed in our marine measurements were primarily smaller than 180 nm in rBC size. As shown in Fig. 3.6, BC-containing particles with D_{core} less than 180 nm display a bimodal lag-times distribution: one mode between -8 and-2 μs corresponds to externally attached or partially coated BC, while the other mode from -2 to 2 μs represents bare or thinly coated BC. In contrast, BC-containing particles with D_{core} greater than 180 nm show a unimodal distribution centered around 0 μs. This suggests that smaller BC-containing particles are more likely to exist in non-core-shell structures in the marine atmosphere. This may result from coagulation processes, where smaller D_{core} are more prone to external attachment by sea salt or other aerosol/droplet components. As shown in Fig. 3.5, BC particles with smaller D_{core} dominate in number, with BC particles of $80 < D_{core} < 180$ nm accounting for 76.3% of the total number concentration. In this study, our analysis focuses on the bimodal lag-times distribution of these smaller BC-containing particles to investigate their non-core-shell structures (Fig. 3.7). In this study, we define BC-containing particles with lag-times < -2 μs as non-core-shell structures.

Figures 3.7 and 3.8 show the influence of vessel density and BC concentrations on the mixing state of BC-containing particles in marine environments. Lag-time distributions show that in regions with vessel densities exceeding 1 hour km^{-2} $month^{-1}$, BC-containing particles with non-core-shell structures are more prevalent. This indicates that in oceanic regions near active shipping lanes, freshly emitted BC from marine vessels can undergo coagulation with other

particles, resulting in a substantial fraction of BC being externally attached to non-BC materials. As shown in Fig. 3.8, when vessel density exceeds 1 hour km^{-2} $month^{-1}$ and BC concentrations are above 300 ng m^{-3}, non-core-shell structures of BC-containing particles constitute 54.3% of the total number concentration. These particles are predominantly composed of freshly emitted BC with smaller core sizes (Fig. 3.5). However, in near coastal regions with high vessel density that are influenced by clean marine air masses, BC concentrations can drop significantly (e.g., < 30 ng m^{-3}), leading to a decrease in the fraction of non-core-shell structures of BC-containing particles. These results highlight the strong influence of shipping emissions on the occurrence and abundance of BC-containing particles with non-core-shell structures.

Compared to oceanic regions with vessel densities exceeding 1 hour km^{-2} $month^{-1}$, a lower fraction of BC-containing particles exhibits non-core-shell morphologies in remote marine environments with vessel densities below this threshold. As shown in Fig. 3.7, coated BC particles with lag-times > 0 μs are more prevalent in remote regions (vessel density < 1 hour km^{-2} $month^{-1}$) than in areas influenced by shipping activity. Specifically, the number fraction of coated BC in low-vessel density regions is approximately 56.2%, significantly higher than the ~27.2% observed in high-vessel density regions. Moreover, under low vessel density conditions, BC concentration has a little effect on the mixing state characteristics (Fig. 3.8), suggesting that BC-containing particles in remote marine environments are primarily influenced by long-range atmospheric transport rather than fresh emissions from local sources such as shipping. This is also supported by the BC size distribution (Fig. 3.5), which indicates a larger core size in these regions. During atmospheric transport, the fraction of non-core-shell BC particles decreases, while the proportion of coated BC particles increases, highlighting the shaping of the marine environments on BC mixing state.

In addition to BC core size and vessel density, RH is also found to significantly influence the occurrence of BC-containing particles with non-core-shell structures (Fig. 3.9). Compared to near-coastal regions with vessel densities exceeding 1 hour km^{-2} $month^{-1}$, such particles in remote oceanic environments (vessel density < 1 hour km^{-2} $month^{-1}$) are more sensitive to variations in RH. This is because, in marine regions with intense shipping activity, the presence of non-core-shell BC particles is primarily governed by shipping emissions. In contrast, in remote oceanic regions with low shipping influence, the abundance and transformation of non-core-shell BC particles are largely shaped by marine environmental factors such as RH.

Figure 3.9 reveals a nonlinear relationship between RH and the occurrence of non-core-shell BC particles. When RH is below 85%, lower RH conditions favor the formation of non-core-shell structures. Specifically, as RH decreases, the number of BC-containing particles with lag-times < -5 μs, indicative of externally attached BC, increases significantly. In contrast, high RH levels above 85% promote the formation of partially coated BC particles, as evidenced by the increasing abundance of particles with lag-times between -5 μs and -2 μs. This suggests two distinct RH-dependent regimes: at RH < 85%, reduced RH enhances the external attachment of BC to non-BC material (lag-times < -5 μs); at RH > 85%, and particularly above 95%, elevated RH facilitates the formation of partially coated BC (-5 μs <lag-times <-2 μs) through interactions with liquid-phase aerosol components such as sea salt. As shown in Fig. 3.9, under RH > 95% in

marine environments with vessel densities below 1 hour km^{-2} $month^{-1}$, the number fraction of partially coated BC particles (-5 μs < lag-times <-2 μs) reaches 33.2%, being significantly higher than the 16.9% observed under moderate RH conditions (75% < RH < 85%).

These findings indicate that under high RH conditions, more BC particles interact with droplets, promoting coagulation and partial coating. As shown in Fig. 3.9, in RH > 95% environments, the fraction of bare and thinly coated BC particles (-2 μs < lag-times < 2 μs) decreases markedly, while the fraction of non-core-shell BC-containing particles, particularly partially coated ones (-5 μs < lag-times < -2 μs), increases significantly. This points to the importance of repeated deliquescence and efflorescence cycles during atmospheric transport in shaping the BC mixing state. As discussed earlier (Fig. 3.7), this is consistent with the enhanced abundance of coated BC particles (lag-times > 0 μs) observed in remote oceanic regions.

3.3.3 Thickly coated BC particles

In addition to non-core-shell BC particles, we also observed thickly coated BC particles with a core-shell structure in the marine environment. As shown in Fig. 3.7, in remote marine regions with vessel densities below 1 hour km^{-2} $month^{-1}$, thickly coated BC particles with lag-times greater than 2 μs accounted for approximately 22% of the BC-containing population. These particles are influenced by both atmospheric transport and physicochemical processes in the marine environment. The lag-time distributions of BC-containing particles (Figs. 3.6-3.9) indicate that the BC mixing state in marine environments is affected by BC core size, vessel density, and RH. To further investigate the impact of the marine environment on thickly coated BC particles, we retrieved the coating thickness of BC-containing particles with lag-times > 0 μs using SP2 measurements. Figure 3.10 presents the coating thickness distributions for different BC sizes under varying vessel densities and RH conditions across different marine regions.

Our study focuses on the coating processes of BC particles emitted from shipping in the marine environment. To distinguish thickly coated BC particles predominantly influenced by marine physicochemical processes from those primarily transported from continental sources, we compared detailed measurements from two S/Y Eugen Seibold cruises near the Canary Islands (ES22C01 in February 2022 and ES22C15 in October 2022), which experienced similar vessel densities at contrasting air mass origins. During the February cruise, air masses mainly originated from continental regions, including the western Mediterranean and northern Africa, passing over areas with intense anthropogenic activity (Fig. S3.6). In contrast, the October cruise was influenced by air masses from remote marine regions over the open Atlantic Ocean, where anthropogenic influence is minimal (Fig. S3.6). Figure S3.7 compares the BC characteristics measured during the two cruises with contrasting air mass origins. Under the influence of continental air masses, BC mass concentration, core size, the fraction of thickly coated BC particles, and coating thickness increased significantly. We found that continental air masses mainly affected the coating thickness of BC particles with D_{core} larger than 80 nm. Figure S3.8 shows an example of a ship plume encounter, revealing that BC from shipping emissions is primarily characterized by D_{core} smaller than 180 nm. Therefore, to investigate the coating

processes of shipping-related BC in the marine atmosphere, we focused our analysis on the coating thickness characteristics of BC particles with D_{core} below 180 nm.

As shown in Fig. 3.10, the coating thickness of BC-containing particles in marine environments is influenced by BC core size, vessel density and RH. Table S2 summarizes the fractions of thickly coated BC particles under different RH and vessel density conditions. For thickly coated BC particles (coating thickness > 30 nm), the coating thickness distribution exhibits two distinct modes: one at ~100 nm associated with BC cores of 100-150 nm, and another at 30-50 nm corresponding to BC cores of 150-180 nm. In near-coastal regions under high vessel density conditions (>1 hour km^{-2} $month^{-1}$), thickly coated BC particles are predominantly composed of smaller BC cores (100-150 nm) with thicker coatings (~100 nm) (Fig. 3.10b), most likely influenced by air masses from continental regions. In contrast, in remote oceanic regions with under low vessel density conditions (<1 hour km^{-2} $month^{-1}$), larger BC cores (150-180 nm) with relatively thinner coatings (30-50 nm) dominate (Fig. 3.10a), which is most likely related to influence of marine environments.

In this work, we focus on thickly coated BC particles in remote marine environments. As shown in Figs. 3.10a and 3.10b, in remote oceanic regions with low vessel density (1 hour km^{-2} $month^{-1}$), BC-containing particles exhibit an additional coating thickness mode (30-50 nm), in contrast to near-coastal regions with high vessel density (>1 hour km^{-2} $month^{-1}$). In remote oceanic regions, RH above 85% enhances the 30-50 nm coating mode of larger BC cores (150-180 nm) more strongly than the ~100 nm coating mode of smaller cores (100-150 nm) (Fig. 3.10a). This contrasts with condensation aging, which is more efficient for smaller particles. This suggests that the RH-driven enhancement of the 30-50 nm coating mode of larger BC is not caused by condensation but is instead dominated by coagulation with other aerosols (e.g., sea salt), followed by droplet formation via deliquescence during atmospheric transport over the ocean. In summary, high humidity over the ocean can promote hygroscopic growth, transforming BC particles that attach with marine aerosol (e.g., sea salt) into thickly coated core-shell particles.

3.4 Summary

In situ measurements from ten cruises aboard the S/Y Eugen Seibold, spanning the Atlantic Ocean (10°N-60°N, 10°E-65°W), provide key insights into BC concentrations and mixing states. These findings help constrain processes that remain poorly represented in global climate models, improving the understanding of BC behavior in marine environments. Despite ship traffic varying by up to five orders of magnitude across the surveyed regions, 1-minute averaged BC concentrations were typically around 100 ng m^{-3}. This highlights a remarkable regional consistency in BC loading, likely driven by large-scale atmospheric transport across oceanic areas spanning up to a thousand kilometers. The BC concentration data obtained in marine environments can be used to constrain BC levels in global climate models to assess BC's climate effect.

In contrast, BC mixing states exhibited pronounced spatial variability. In coastal regions (within tens of kilometers from land), BC particles were primarily externally attached to non-BC aerosols, indicative of relatively fresh emissions. In remote oceanic areas (extending up to a thousand kilometers offshore), the fraction of coated BC particles increased substantially. These observations suggest that in marine environments, BC mixing states are influenced not only by emission sources but also by environmental conditions, particularly RH. Our results suggest that high RH can promote the transformation of externally attached BC into partially and eventually thickly coated core-shell structures via repeated deliquescence-efflorescence cycles. These findings provide critical insights into the aging process of BC in remote marine atmospheres.

This work suggests the potential for the marine atmosphere to amplify BC’s climate impacts. Coagulation with non-BC aerosols and subsequent hygroscopic growth under humid conditions facilitate the development of core-shell morphologies, significantly enhancing BC's light absorption via the lensing effect. Moreover, marine-induced transformation of BC mixing state may increase its ability to act as cloud condensation nuclei. Future research should further explore BC-marine aerosol interactions and evaluate their roles in aerosol-cloud-radiation feedback.

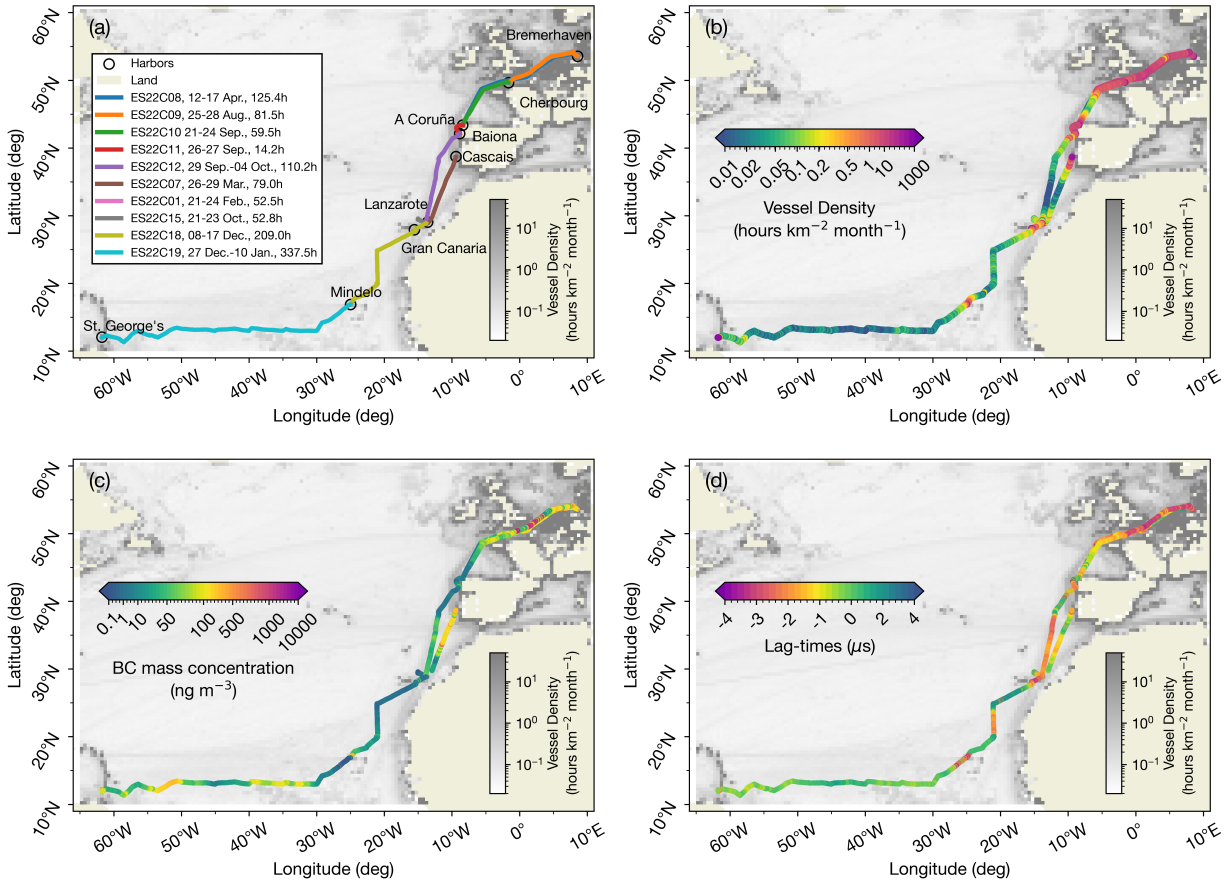

Figure 3.1. Cruise tracks of the S/Y Eugen Seibold across the Atlantic Ocean during ten cruises conducted from February 2022 to January 2023, overlaid on monthly averaged vessel density maps (hour km^{-2} month^{-1}). (a) Ship tracks color-coded by individual cruise legs, with cruise identifiers and measurement periods provided in the legend. Key harbors and coastal locations visited during the cruises are indicated. (b) Vessel density along the cruise routes extracted from monthly AIS-based vessel traffic data. (c) rBC mass concentration measured using the SP2 along the cruise paths. (d) Lag-times (μs), defined as the time offset between scattering and incandescence signals from the SP2.

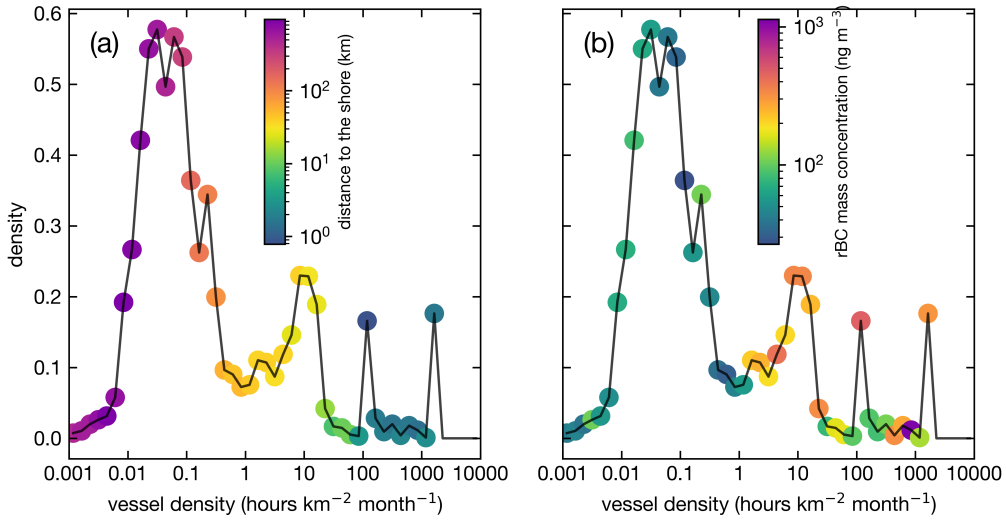

Figure 3.2. Probability density function (PDF) of vessel density (hour km^{-2} month^{-1}) across all measurement points. (a) Vessel density color-coded by the average distance to shore (km) for each bin. (b) Vessel density color-coded by average rBC mass concentration (ng m^{-3}).

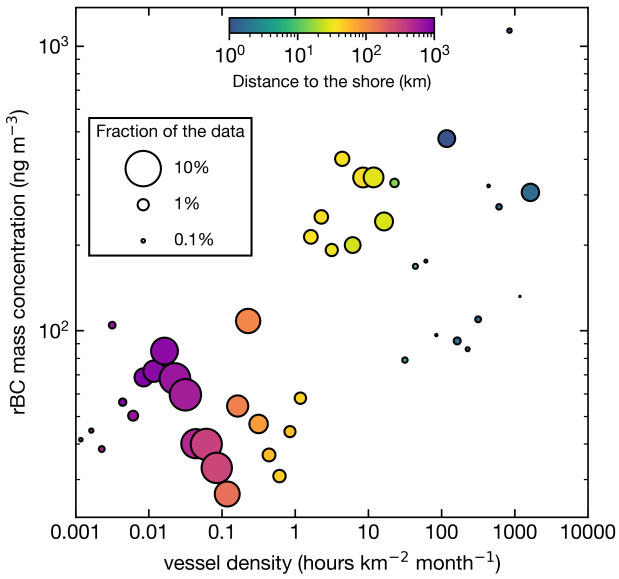

Figure 3.3. Relationship between vessel density (hour km^{-2} month^{-1}) and rBC mass concentration (ng m^{-3}), color-coded by distance to shore (km) and sized by the fraction of the total dataset (1-min average) represented by each bin. Warmer colors (e.g., pink, orange) indicate offshore locations, while cooler colors (e.g., green, blue) correspond to measurements taken closer to shore. Larger circle sizes indicate a greater fraction of data.

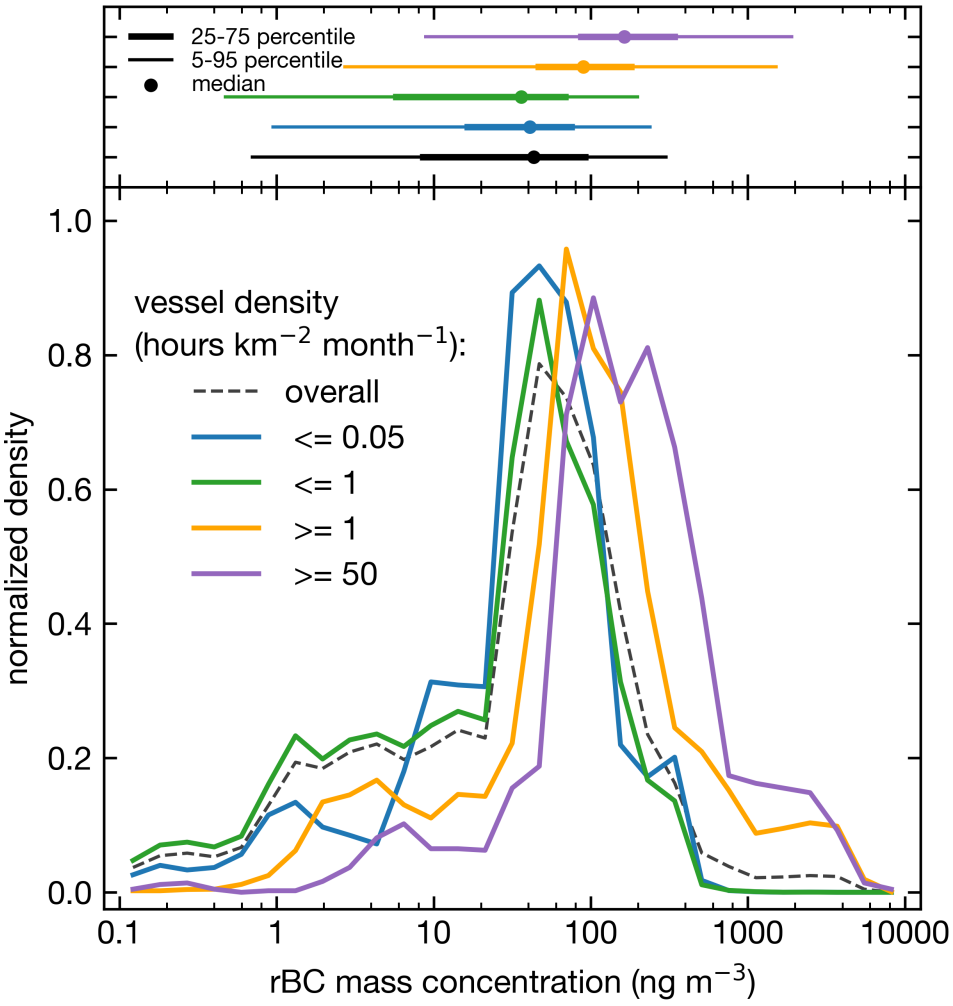

Figure 3.4. Probability density functions (PDFs) of rBC mass concentration (ng m^{-3}) 1-min average for different vessel densities. The color-coded lines represent subsets of data with varying vessel densities: ≤0.05 (blue), ≤1 (green), ≥1 (orange), and ≥ 50 hour km^{-2} $month^{-1}$ (purple), with the overall distribution shown in dashed black. The top panel indicates the 25-75th percentile (thick line), 5-95th percentile (thin line), and median (dot) for each category. Statistical summary of rBC mass concentrations under different vessel density regimes is shown in Table S1.

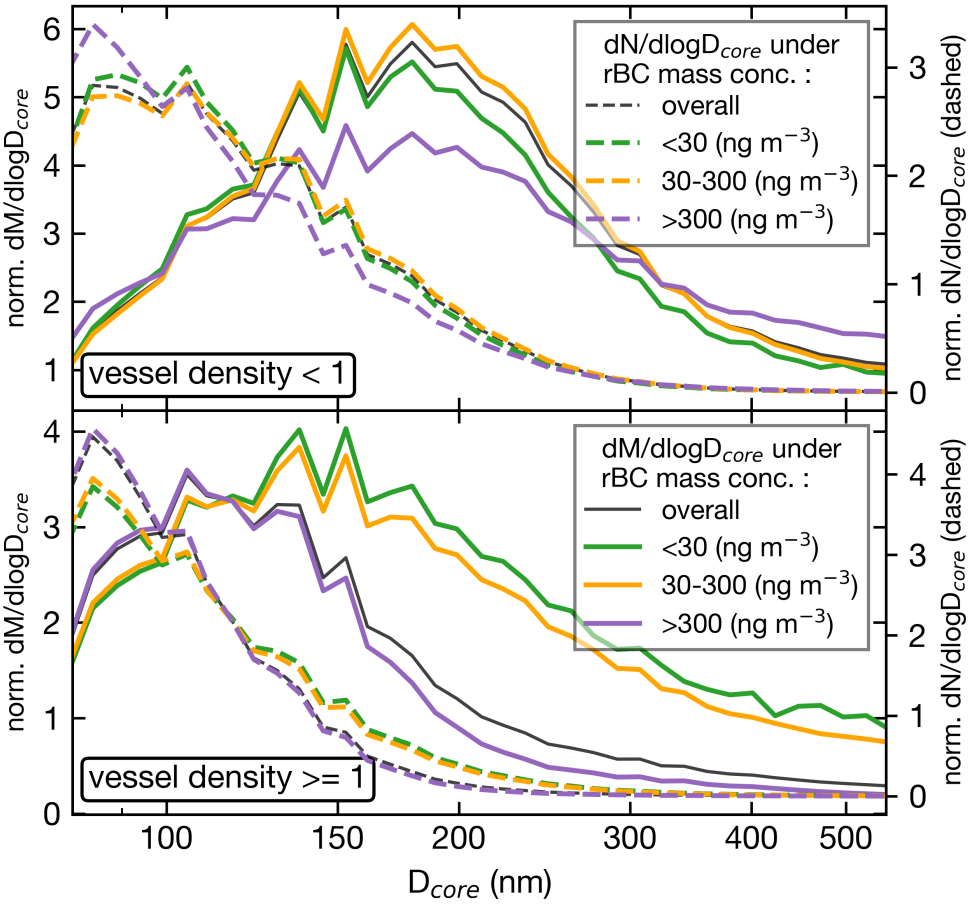

Figure 3.5. Core size distributions of BC-containing particles under different vessel density and rBC mass concentration conditions. Top panel: Observations in regions with vessel density < 1 hour km^{-2} month^{-1}. Bottom panel: Observations in regions with vessel density ≥ 1 hour km^{-2} month^{-1}. Solid lines represent mass-weighted distributions (dM/dlogD$_{core}$), and dashed lines represent number-weighted distributions (dN/dlogD$_{core}$, each normalized to their respective maxima. Colors indicate BC mass concentration bins: <30 ng m^{-3} (green), 30-300 ng m^{-3} (orange), and >300 ng m^{-3} (purple), with the overall distribution shown in black.

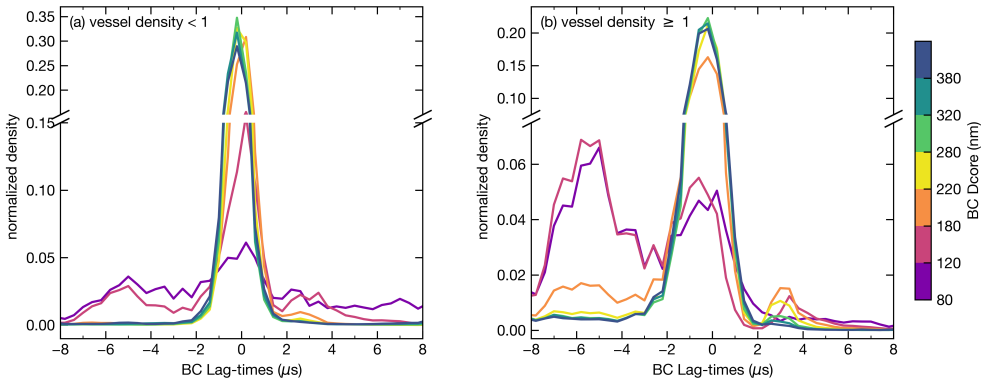

Figure 3.6. Lag-time distributions of BC-containing particles in different core size (Dc) ranges under contrasting vessel density regimes. (a) Regions with vessel density < 1 hour km^{-2} $month^{-1}$; (b) Regions with vessel density ≥ 1 hour km^{-2} $month^{-1}$. Each curve represents a different D_{core} size bin (color-coded), from 80 nm to 380 nm. Lag-times were calculated as the temporal offset between the peak scattering and incandescence signals.

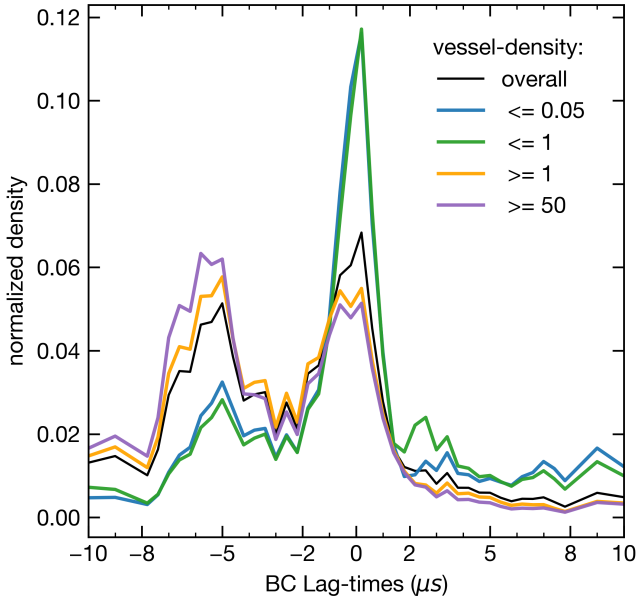

Figure 3.7. Normalized lag-time distributions of BC-containing particles under different vessel density regimes. Lines represent subsets of data binned by vessel density: ≤ 0.05 (blue), ≤ 1 (green), ≥ 1 (orange), ≥ 50 hour km^{-2} $month^{-1}$ (purple), and >0 (black, overall dataset). Particles with lag-times < -2 μs are classified as non-core-shell, while those with lag-times > 0 μs are considered coated.

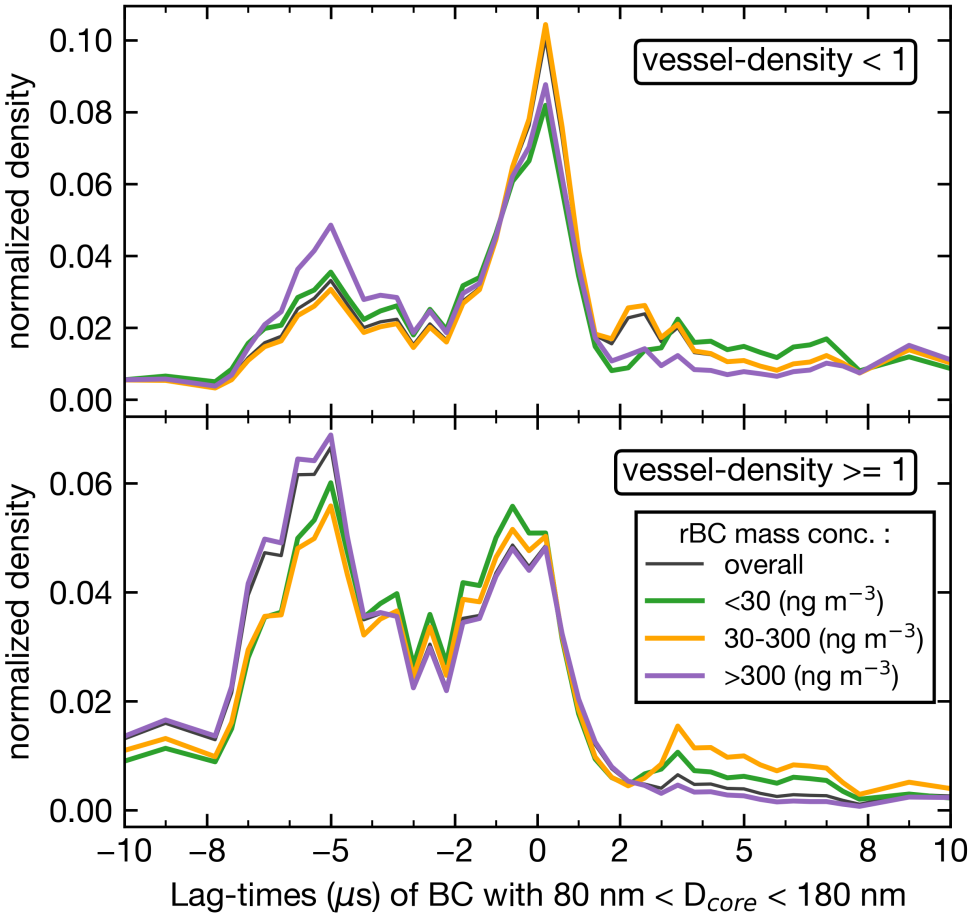

Figure 3.8. Lag-times distributions of BC-containing particles with core diameters between 80 and 180 nm, stratified by vessel density and BC mass concentration. Top: Regions with vessel density <1 hour km^{-2} $month^{-1}$. Bottom: Regions with vessel density ≥1 hour km^{-2} $month^{-1}$. Lines are color-coded by BC mass concentration: <30 ng m^{-3} (green), 30-300 ng m^{-3} (orange), >300 ng m^{-3} (purple), and the overall distribution (black).

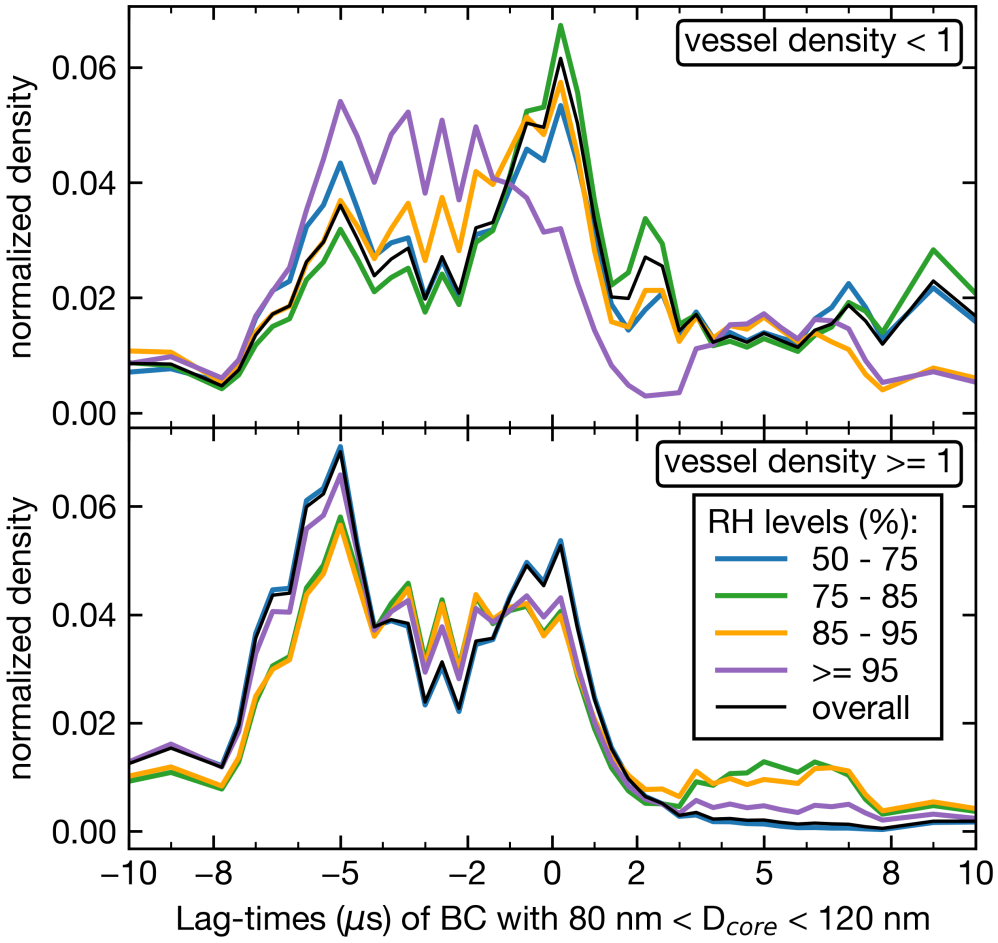

Figure 3.9. Lag-time distributions of BC-containing particles with core diameters between 80 and 120 nm, stratified by vessel density and relative humidity (RH). Top: Regions with vessel density <1 hour km^{-2} month^{-1}. Bottom: Regions with vessel density ≥1 hour km^{-2} month^{-1}. Lines are color-coded by RH level: 50-75% (blue), 75-85% (green), 85-95% (orange), ≥95% (purple), with the overall distribution shown in black.

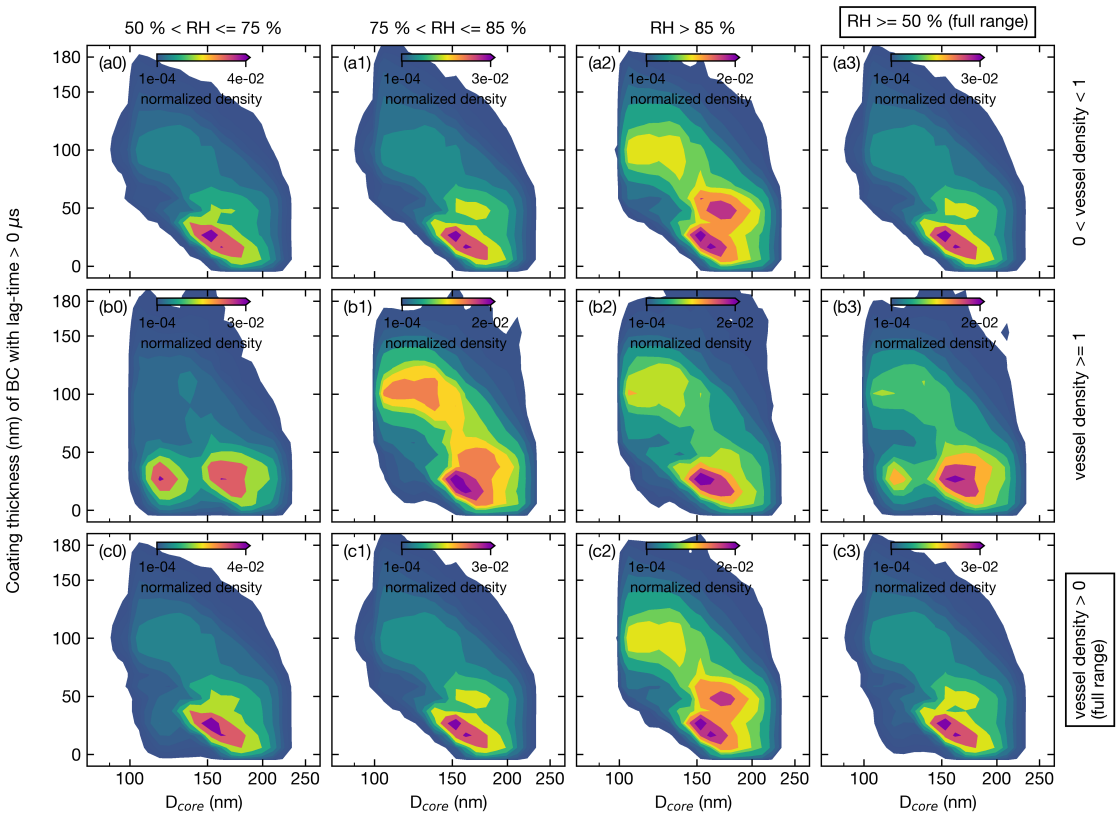

Figure 3.10. Distributions of BC coating thickness as a function of BC core diameter (D_{core}), organized by RH and vessel density regimes. Columns represent RH categories: (1) 50% < RH ≤ 75%, (2) 75% < RH ≤ 85%, (3) RH > 85%, and (4) RH ≥ 50% (entire RH range). Rows indicate vessel density conditions: (a) <1 hour km^{-2} month^{-1} (remote marine regions), (b) ≥1 hour km^{-2} month^{-1} (shipping-influenced regions), and (c) >0 hour km^{-2} month^{-1} (overall dataset). Color shading indicates particle counts on a logarithmic scale.

Appendix

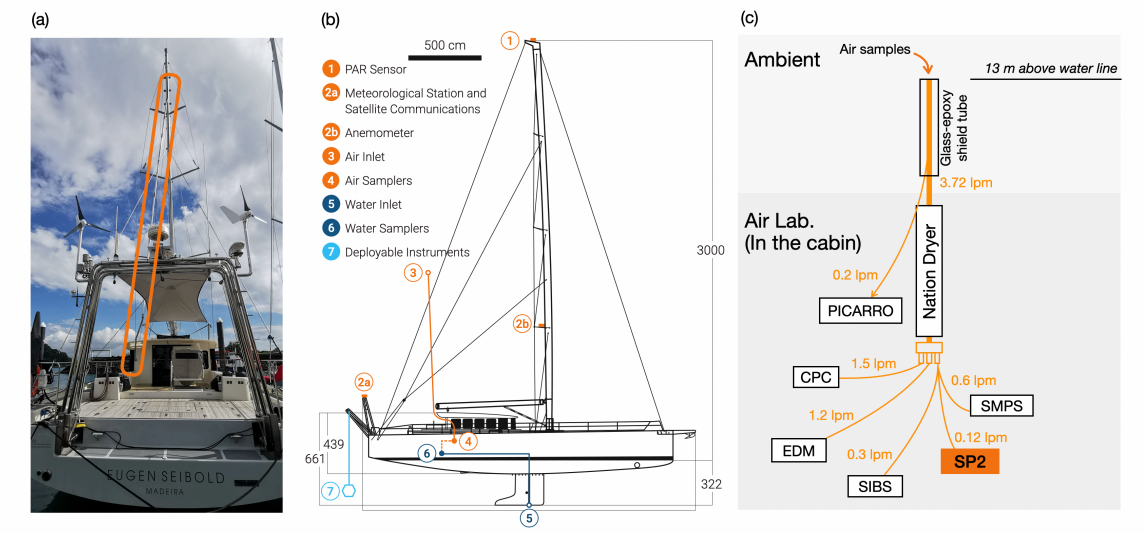

Figure S3.1. Experimental setup aboard the S/Y Eugen Seibold. (a) Photo of the vessel's stern showing the main inlet shield tube (orange) extending to the air sampling inlet. (b) Side elevation of the ship, highlighting the positions of key environmental sensors and sampling ports, including the aerosol inlet mounted approximately 13 m above the waterline. (c) Schematic of the aerosol and gas sampling system inside the Air Lab. Ambient air was dried to <30% relative humidity using a Nafion dryer before distribution to the SP2 and other instruments. Flow rates for each channel are indicated.

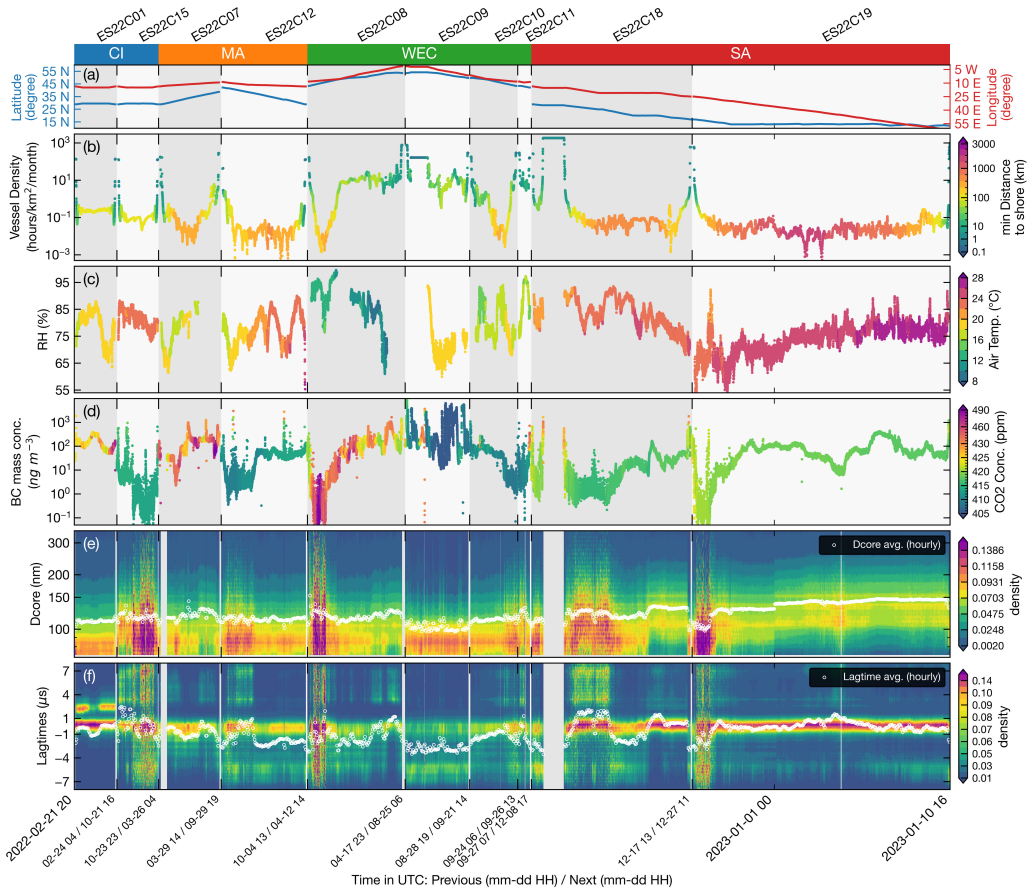

Figure S3.2. Time series analysis of black carbon (BC) aerosols and environmental variables during 10 Atlantic Ocean cruises (February 2022-January 2023). Shaded regions highlight individual cruise segments, and cruise IDs are labeled above the panels. The x-axis ticks represent the time in UTC, indicating the start and end of two adjacent cruises. (a) Latitude (blue) and longitude (red) plotted as lines, with cruise segments labeled above. (b) Ship density along the cruise tracks (hour km^{-2} $month^{-1}$), color-coded by the distance to the nearest shoreline (km), which represents the calculated minimal distance from measurement coordinates to the coastline (10-meter-resolution). The vessel density data points correspond to monthly average data sourced from the Global Maritime Traffic Density Service (GMTDS), GlobalMaritimeTraffic.org, a service of MapLarge, 2024 (https://www.globalmaritimetraffic.org). (c) Relative humidity (RH, %) shown as scatters with air temperature (°C) color-coded on each data point. (d) BC mass concentrations (ng m^{-3}) shown as scatters, with the color scale indicating corresponding CO2 concentrations (ppm). (e) Ten-minute normalized BC core size distributions (D_{core}, nm) represented as color-coded particle size bins, with white circles indicating hourly averages. (f) Ten-minute normalized lag-time distributions (μs) shown as color-coded density bins, with white circles representing hourly averages.

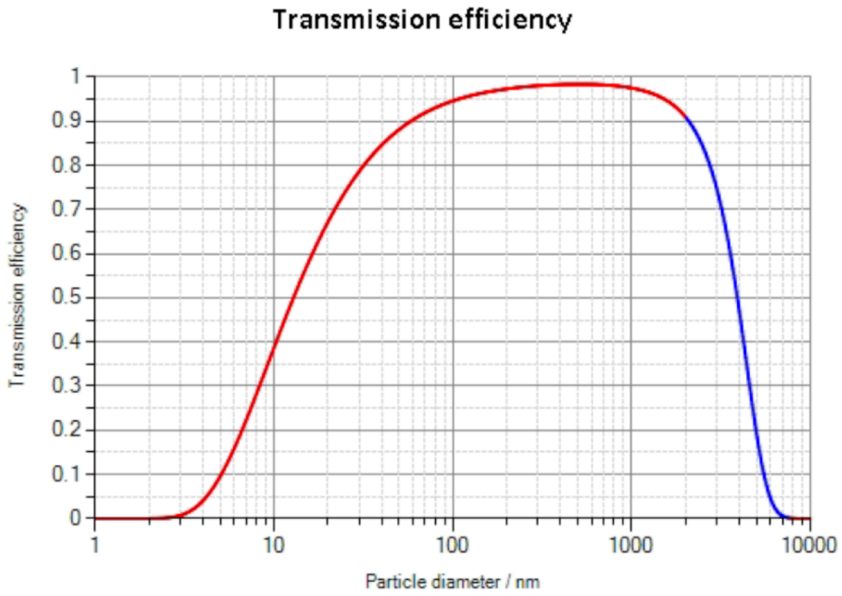

Figure S3.3. Transmission efficiency for the SP2 inlet system (from ambient to SP2 inlet), calculated using the Particle Loss Calculator in August 2022.

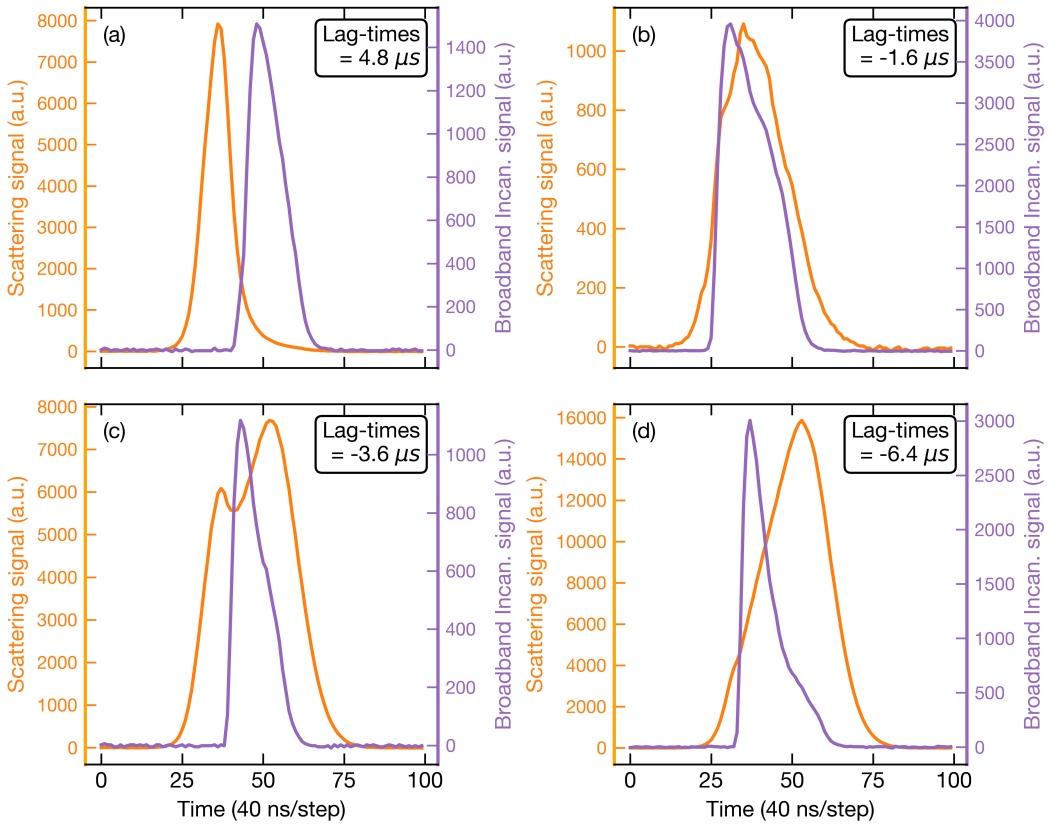

Figure S3.4. Representative time-resolved SP2 signals of BC-containing particles illustrating positive and negative lag-time patterns. Each panel shows elastic scattering signals (orange, left axis) and broadband incandescence signals (purple, right axis) as a function of time. (a) Example of a thickly coated BC particle with a positive lag-time (4.8 µs); (b)-(d) Examples of BC particles with negative lag-times (-1.6 µs, -3.6 µs, and -6.4 µs, respectively), indicating non-core-shell structures.

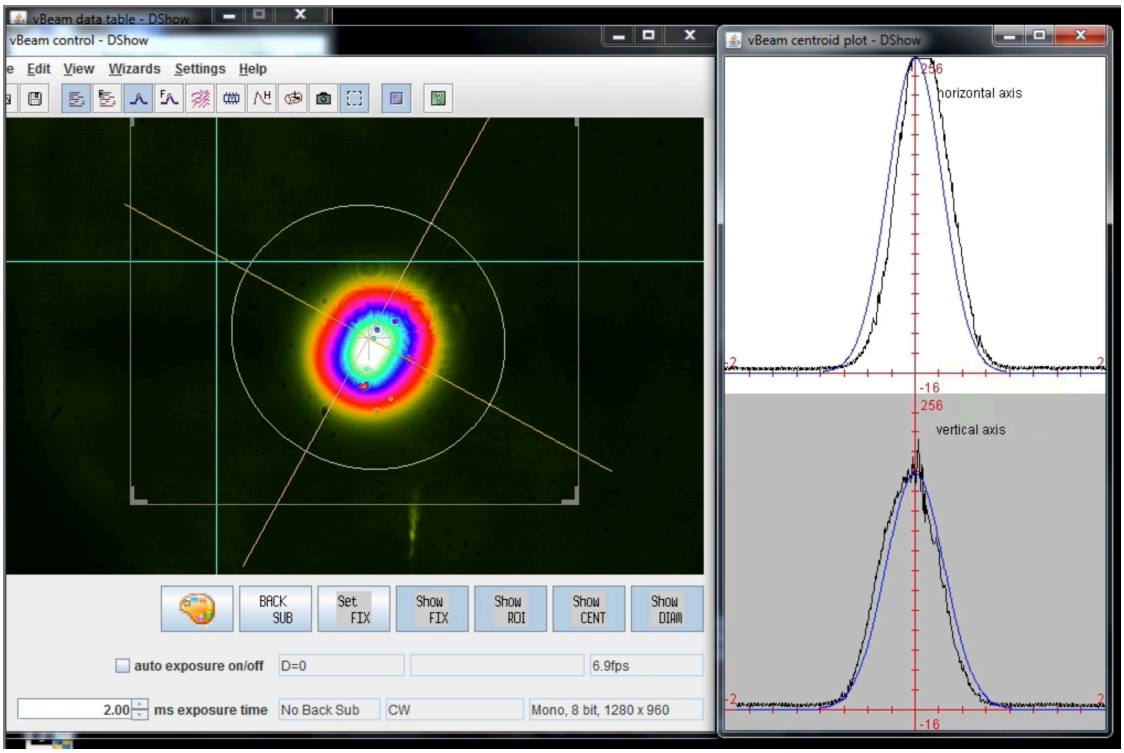

Figure S3.5. The laser intensity profile closely follows the TEM00 Gaussian mode.

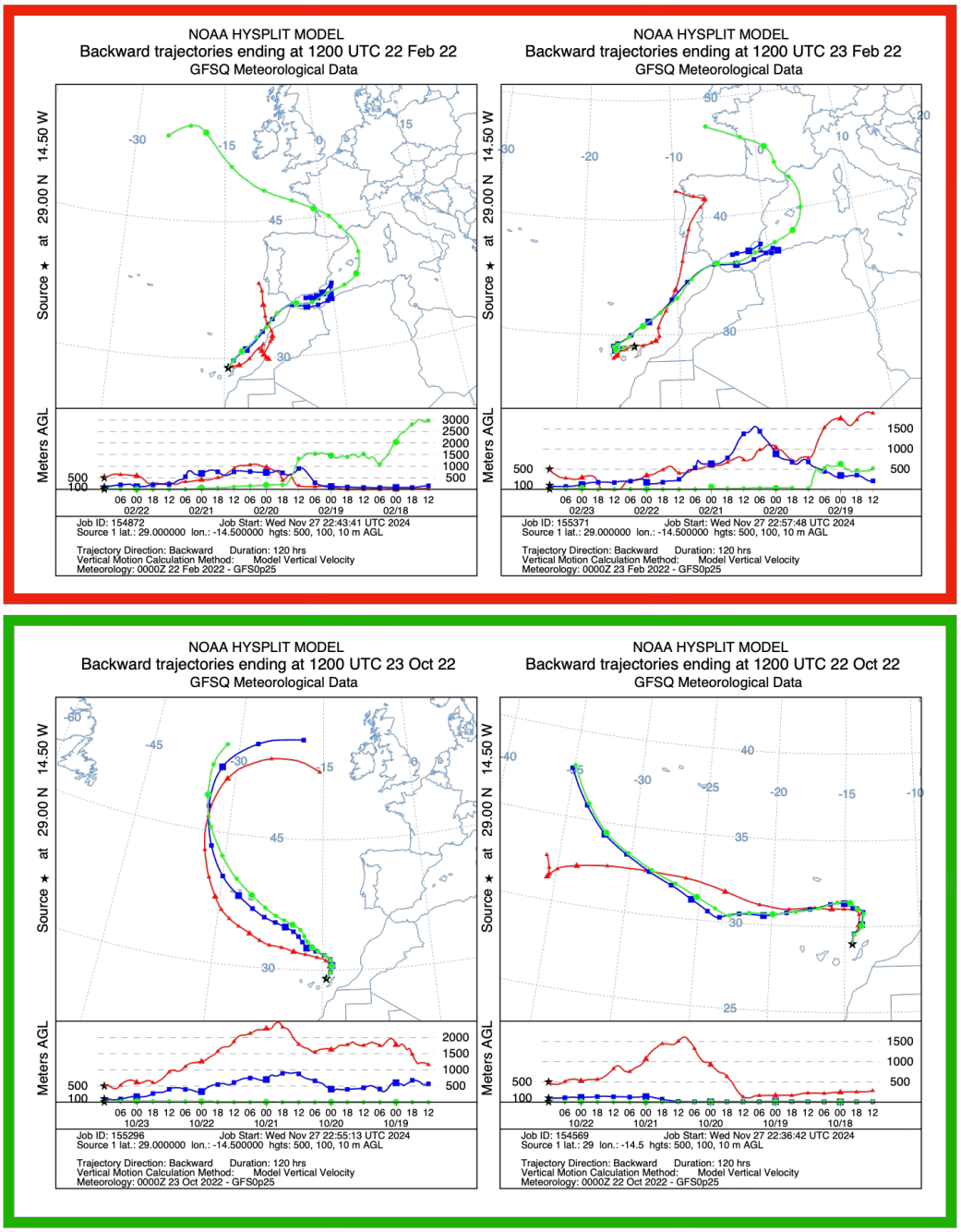

Figure S3.6. NOAA HYSPLIT backward-trajectory analyses for two sampling periods in February (green box, ES22C01) and October (red box, ES22C15) 2022. Each map shows three color-coded trajectories (red, blue, green) originating near 29° N 14.5° W, with corresponding altitude profiles beneath each panel. Trajectories were computed using GFS0 meteorological data at 1200 UTC on the indicated dates.

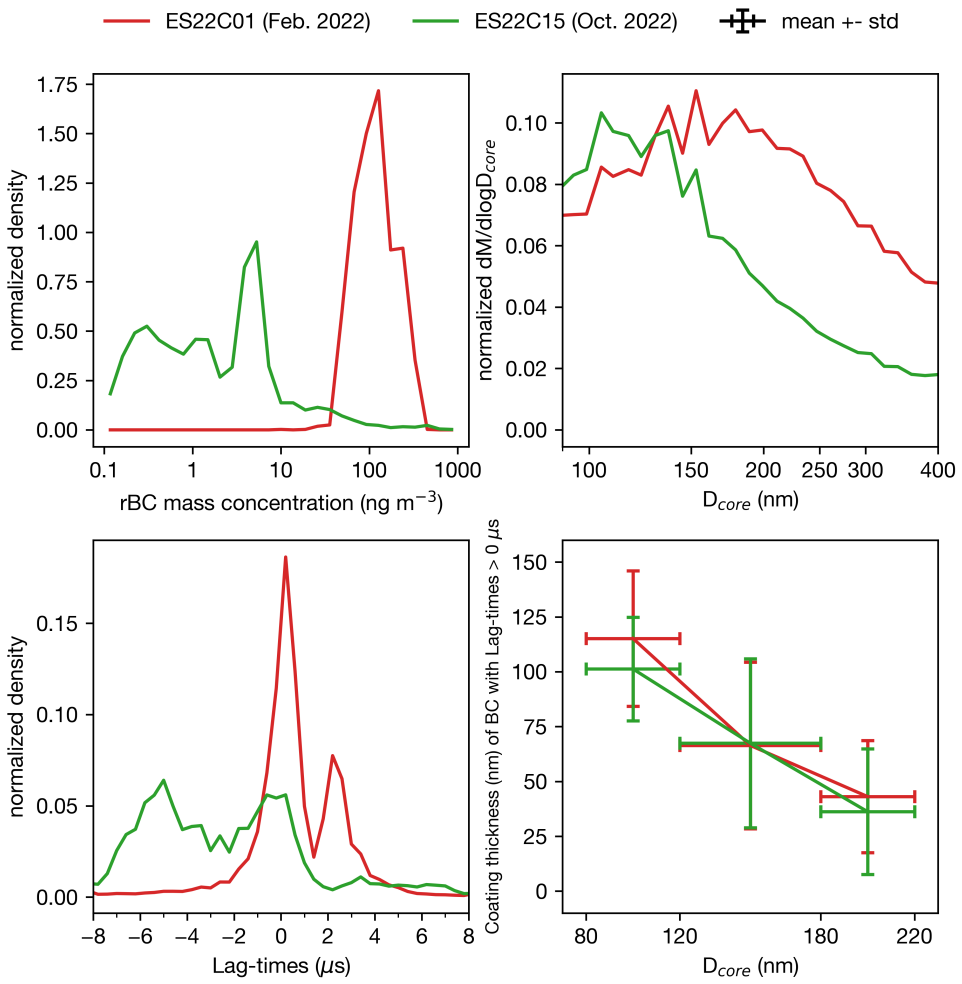

Figure S3.7. Comparison of rBC characteristics measured during two cruises near the Canary Islands: ES22C01 (February 2022; red lines) and ES22C15 (October 2022; green lines). Shown are probability PDFs of BC mass concentration (top left), normalized mass-weighted BC core size (D_{core}) distributions (top right), lag-time distributions (bottom left), and BC coating thickness distributions for selected core diameters (180-280 nm) with positive lag-times (bottom right).

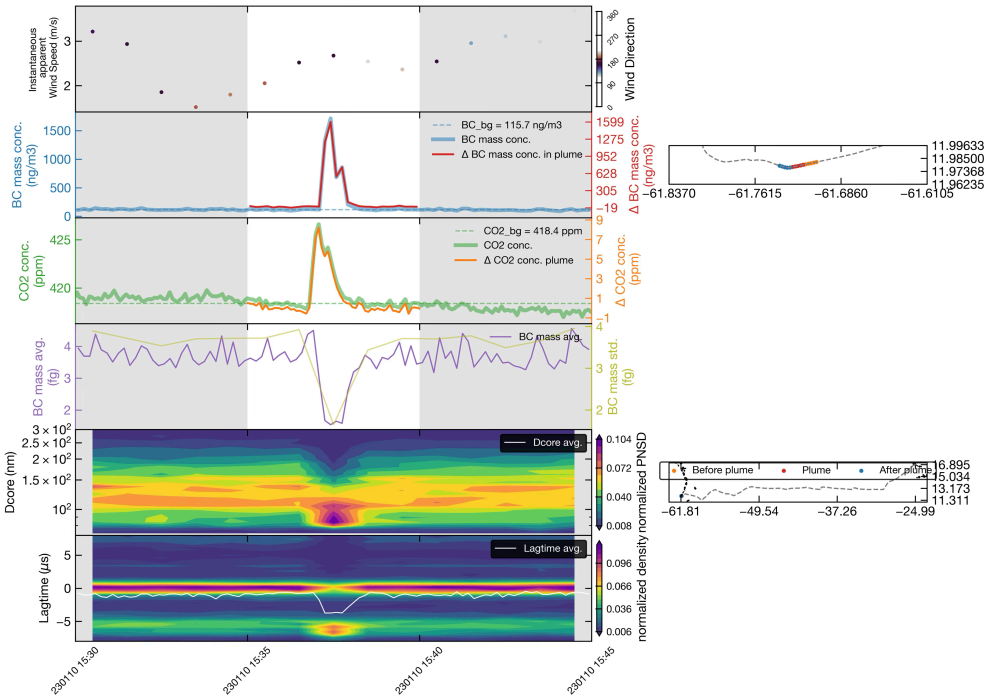

Figure S3.8. Example of a ship-emission plume encounter on 2023/10/29. From top to bottom, the time-series panels show (i) wind speed and direction (ii) BC mass concentrations (blue line) with background BC (BC_bg) and the instantaneous ΔBC concentration in the plume (red line); (iii) CO2 concentrations (green line) with background CO2 (CO2_bg) and the plume-induced concentration change (orange line); (iv) the rolling average of BC mass (purple) and its relative drop (gray shading); (v) the BC core size distributions (D_{core}, nm) displayed as color-coded bins; and (vi) the lag-times distributions (μs), also color-coded by normalized density. Shaded intervals mark the plume period, and inset panels on the right indicate vessel position and measurement segments (before, during, after the plume).

Table S3.1. Statistical summary of BC mass concentrations (ng m-3) under different vessel density regimes in the Atlantic marine environment, spanning tens to a thousand kilometers from the coastline. Values include mean, median, standard deviation (Std), and percentiles (5th, 25th, 75th, and 95th).

	Mean	Median	Std	5-th perc.	25-th perc.	75-th perc.	95-th perc.
Vessel density (hour km^{-2} $month^{-1}$)	BC mass concentrations (ng m^{-3})						
> 0 (overall)	121.9	46.4	375.4	0.9	9.	101.7	328.1
< 0.05	64.9	42.6	80.8	1.1	17.1	77.4	239.7
< 1	58.8	36.4	78.4	0.7	6.7	74.4	221.0
>= 1	323.2	103.2	719.6	3.2	50.7	219.5	1769.2
>= 50	439.8	192.2	765.5	13.1	93.8	397.4	2096.1

Table S3.2. Fractions (%) of thickly coated BC-containing particles with coating thickness >30 nm and >50 nm under various relative humidity (RH) and vessel density conditions.

	50% < RH <= 75%	75% < RH <= 85%	RH > 85%	Overall (RH > 50%)
	BC with coating > 30 nm as (%) of BC with lag time > 0.1 µs and D_{core} > 90 nm			
Vessel density < 1	56	61	75	61
Vessel density >= 1	53	75	71	65
Overall (vessel density> 0)	56	62	75	44
	BC with coating > 50 nm as (%) of BC with lag time > 0.1 µs and D_{core} > 90 nm			
Vessel density < 1	36	42	56	42
Vessel density >= 1	22	58	55	43
Overall (vessel density > 0)	35	43	56	30

”

Chapter 4 Aging and Thick Coating Formation of Black Carbon during Marine-Dominated Regional Transport over the Northeast Atlantic

This work is to be submitted as Pan et al. (2025):

Xihao Pan, Yuxuan Zhang, Chaoyang Xue, Uwe Kuhn, Isabella Hrabe de Angelis, Christopher Pöhlker, Jeannine Ditas, Lena Heins, Hedy M. Aardema, Hans A. Slagte, Maria Ll. Calleja, Antonis Dragoneas, David Walter, Björn Nillius, Qiaoqiao Wang, Nan Ma, Hang Su, Ulrich Pöschl, Gerald H. Haug, Ralf Schiebel, Yafang Cheng: Aging and Thick Coating Formation of Black Carbon during Marine-Dominated Regional Transport over the Northeast Atlantic, Journal of Geophysical Research: Atmospheres, 2025

I am the first-author of this work and my contribution to this work includes maintaining and calibrating the instruments, organizing and analyzing the data, making the figures and tables, discussing the results, interpretation and drafting the manuscript.

The following text, figures, and tables quoted (within "") from page 73 to page 87 are the same as the manuscript which is cited on page 72.

"

Abstract

Black carbon (BC) is a major contributor to climate forcing. However, its impacts remain highly uncertain, partly due to limited understanding of its aging and coating growth during atmospheric transport, especially over marine environments. Observational constraints on how regional transport and marine processes modify BC mixing state are scarce, hindering accurate representation in global climate models. Here, we present shipborne measurements aboard the research sailing yacht S/Y Eugen Seibold from seven cruises in June-August 2020 across the Northeast Atlantic (35-66° N, 30 W-10° E). We find that continental air masses transported from Europe enhanced BC loadings over the Atlantic by tens to hundreds of ng cm^{-3}, while marine air masses promoted extensive aging of BC. Under marine-dominated regional transport, high number fractions of thickly coated BC (>50%) were observed, significantly higher than those under continental influence (<30 %). The results reveal that BC undergoes pronounced aging in the marine atmosphere, forming coatings of 100-200 nm. Such highly aged, thickly coated BC particles can markedly amplify direct radiative forcing and act as efficient cloud condensation nuclei, thereby exerting significant impacts on the marine climate. These observations highlight the critical role of the marine environment in BC aging during regional transport and provide essential constraints for parameterizing BC mixing state in climate models.

4.1 Introduction

Black carbon (BC) is a short-lived climate forcer whose radiative and microphysical effects depend on mixing state—whether BC remains externally mixed or becomes internally mixed with non-refractory material (e.g., sulfate, organics). Variations in mixing state can significantly affect BC optical properties, hygroscopic growth, ice nucleation potential, and atmospheric lifetime, complicating precise quantification of its climatic impact (Bond et al., 2013; Cheng et al., 2012). The marine environment, with its extensive area, limited local emissions, and high surface albedo, is particularly susceptible to radiative forcing by BC, even trace amounts of BC can disproportionately increase column heating and depress single-scattering albedo. Improving the understanding and representation of BC mixing state under realistic atmospheric conditions remains a significant challenge and requires more comprehensive observational data, especially from marine regions (Moteki, 2023; Wang et al., 2023b).

However, in situ BC measurements over the ocean remain limited and are primarily concentrated in coastal regions and near-source corridors. Direct observations in remote open-ocean air are scarce, constraining our understanding on how marine transport and oceanic conditions shape— and potentially promote—BC loadings and mixing state. The few remote open-ocean observations generally report very low background BC, commonly at a few ng m^{-3}

and occasionally <1 ng m^{-3}, punctuated by episodic enhancements from long-range transport and wildfires (Deng et al., 2024; Fossum et al., 2022; Katich et al., 2018). By contrast, coastal and near-source studies consistently report elevated BC loadings—typically tens to several hundred ng m^{-3}—linked to shipping and port activity, and they generally observe fresher BC with limited evidence of strong internal mixing (Buffaloe et al., 2014; Cappa et al., 2014; Diesch et al., 2013). However, the role of atmospheric transport in driving the aging of BC and its subsequent coating growth over marine environments—and the conditions that promote such transformations—remains poorly understood. These gaps limit both the parameterization of BC aging and the assessment of its radiative impact in marine settings.

This study presents shipborne measurements across the Atlantic Ocean, explicitly investigating how marine atmospheric processes influence BC mixing state. Utilizing observations from the research sailing yacht S/Y Eugen Seibold during seven cruises from June to August 2020 across the Northern Atlantic, this study characterizes BC under two distinct atmospheric transport regimes: continental-dominated and marine-dominated regional transport. By analyzing the size-resolved mixing state using Single Particle Soot Photometer (SP2) measurements and trajectory-based air-mass classifications, this study quantizes how regional transport conditions influence the formation and evolution of thickly coated BC. The findings reveal that marine atmospheric conditions substantially enhance the fraction of thickly coated BC, primarily through coagulation processes and hygroscopic growth rather than condensation-driven coating formation. This research not only provides crucial observational constraints on BC mixing state in marine atmospheres but also delivers insight into the mechanisms driving BC aging during long-range marine transport.

4.2 Methods

4.2.1 Black carbon aerosol measurement

Shipboard BC observations were made aboard the research sailing yacht S/Y Eugen Seibold, a 72-ft platform equipped for atmosphere–ocean sampling. Ambient air was drawn through the vessel's shared whole-air inlet mounted ~13 m above the waterline, dried with a Nafion dryer, and manifolded to the aerosol instruments, including the SP2. The Chapter 4 dataset covers seven summer 2020 (ES20C01–ES20C07), spanning the Northeast Atlantic from Bremerhaven (Germany) to the Azores (Portugal); the track ranges from roughly 35–66° N and 30° W–10° E (see Fig. 4.1 of this chapter). Platform and inlet details follow those used throughout our Eugen Seibold campaigns (Aardema et al., 2024; Schiebel et al., 2024).

Refractory black carbon (rBC) was quantified with a Single Particle Soot Photometer (SP2) using laser-induced incandescence to retrieve per-particle rBC mass and the corresponding mass-equivalent core diameter D_c (Schwarz et al., 2006; Stephens et al., 2003). Instrument calibrations (fullerene-soot for incandescence–mass, PSL for scattering) and the mixing-state diagnostics (lag-times classification and LEO-fit for coated particles) are identical to those used

previously; see Chapters 2 and 3 for the details full data processing workflow which is applied here.

4.2.2. Back-trajectory analysis

We used the Lagrangian particle dispersion model FLEXPART (v11) in backward mode to characterize air-mass origin and quantify wildfire influence during the cruises (Bakels et al., 2024). For each hourly receptor time along the ship track, FLEXPART simulated 50,000 particles instantaneously at 100 m above sea level and integrated them 72 hours backward in time. Simulations were driven by NCEP FNL analyses (1° grid, 6-hourly) and included boundary-layer turbulence, convection, and age-spectra diagnostics.

FLEXPART yielded (1) a trajectory-based depiction of the transport pathway and (2) a gridded source–receptor sensitivity (SRR; “footprint”) on the FLEXPART grid around the receptor. SRR was calculated hourly on a 0.1° resolution in this study. The wildfire attribution step combines these SRR footprints with wildfire emissions (CAMS Global Fire Assimilation System, GFAS, Kaiser et al., 2012), as described in the Appendix.

4.3 Results and discussion

4.3.1 Influence of regional transport on BC loading in the Atlantic atmosphere

In this study, the observational data were classified into two categories based on the origin of regional air masses: land-dominated and ocean-dominated regional transport. As shown by the 3-day backward trajectory analysis (Fig. 4.1), during the shipborne campaign conducted from June to August 2020, the air masses sampled between June and early July over the region 53-63°N and 8° W-10°E were predominantly influenced by continental outflow from Western Europe (Group 1). In contrast, during the measurements from mid-July to August over 35-66°N and 25-9°W, the regional transport was mainly governed by marine air masses (Group 2). Subsequent analyses of BC characteristics were classified according to these two types of regional transport.

BC transported via regional processes is typically more aged, and this study therefore focuses on thickly coated BC to elucidate the characteristics of regionally transported BC in the marine environment. As illustrated in Fig. S4.1, the lag-time distribution of BC-containing particles measured by the SP2 exhibited a distinct bimodal pattern, with pronounced peaks at approximately 0 μs and 2 μs, and a clear separation at 1.6 μs. Previous SP2-based studies (Moteki and Kondo, 2007; Sedlacek et al., 2012; Zhang et al., 2016) have employed such lag-time distributions to identify internally mixed (thickly coated) BC. In the present study, BC-containing particles with lag-times exceeding 1.6 μs were classified as thickly coated BC and used to analyze the properties of regionally transported BC in the marine atmosphere.

As shown in Figs. 4.2a and 4.3, air masses originating from continental regions can substantially enhance BC loading in the marine environment by several tens of ng cm^{-3}. Under the combined influence of continental outflow and maritime emissions (group 1), BC concentrations typically ranged from several tens to several hundred ng cm^{-3}, whereas during marine air mass dominance (group 2), they were generally limited to a few to several tens of ng cm^{-3}. This demonstrates that continental outflow can elevate marine BC levels by approximately one order of magnitude (Fig. 4.3a). The BC mass concentration distribution under group 1 conditions exhibited a clear peak around 100 ng cm^{-3}, consistent with the S/Y Eugen Seibold 2022 cruise observations from coastal to remote Atlantic regions (Chapter 3), suggesting that BC in the Atlantic marine atmosphere is typically influenced by both continental outflow and maritime emissions. Notably, the background BC concentration defined in this study refers to the peak value of the 1-min or 10-min averaged BC mass concentration distributions, representing typical marine atmospheric conditions influenced by both continental outflow and maritime emissions.

When the marine atmosphere was influenced by continental air masses transported from regional sources (group 1), the mass concentration of more aged BC particles with lag-times greater than 1.6 µs ranged from a few to several tens of ng cm^{-3} in the North Atlantic atmosphere, with a peak around ~10 ng cm^{-3} (Fig. 4.3b). These BC particles were most likely derived from continental emission sources in Western Europe (Fig. 4.1b). The aged BC transported from continental emission not only enhanced the overall BC loading in the marine environment but also exerted a significant influence on aerosol radiative absorption and aerosol-cloud interactions due to its higher light absorption capacity and enhanced hygroscopicity (Cappa et al., 2019; Lack and Cappa, 2010; Liu et al., 2017). The subsequent analysis in this study focuses on these regionally transported, more aged BC particles, aiming to elucidate their further aging processes in the marine atmosphere through comparison with BC associated with marine air masses (group 2).

4.3.2 BC size and mixing state

When the marine atmosphere was influenced by both continental air masses and maritime emissions (group 1), the presence of BC from multiple sources such as fossil fuel combustion and biomass burning resulted in a broader BC core size distribution, with an increased fraction of larger BC cores. As shown in Fig. 4.4 (left panels), the mass size distribution of BC cores under group 1 conditions exhibited a peak around ~150 nm, which is larger than that of BC cores dominated by maritime emissions (group 2), where the peak occurred at ~130 nm. For maritime emissions, BC primarily originates from fossil fuel combustion, particularly ship emissions, whereas continental air masses contain BC from a wider range of sources including both fossil fuel combustion and biomass burning. Generally, BC emitted from fossil fuel combustion exhibits smaller core sizes than that from biomass burning(Cheng et al., 2018; Liu et al., 2014; Schwarz et al., 2008). FLEXPART analysis further indicated a contribution from wildfire emissions in group 1, suggesting that some continental air masses transported wildfire-derived BC to the North Atlantic atmosphere. In summary, regional transport, particularly from anthropogenically influenced continental air masses, enriches the sources of BC in the marine environment and broadens the BC core size distribution.

For thickly coated BC with lag-times greater than 1.6 μs, the differences in BC core size distributions between group 1 and group 2 suggest distinct aging processes in marine and continental environments. As shown in Fig. 4.4 (right panels), under continental air mass influence (group 1), the mass size distribution of BC cores peaked below 150 nm, whereas under marine air mass dominance (group 2), the peak shifted to above 150 nm. This indicates that thickly coated BC formed in continental environments tends to have smaller cores than those formed in marine environments, likely reflecting different BC aging processes. In continental regions, where secondary aerosol precursors are abundant, BC aging is primarily driven by condensation, and smaller BC particles are more readily converted into thickly coated forms (Fierce et al., 2015; Peng et al., 2016; Riemer et al., 2010). In contrast, as discussed in Chapter 3, the low precursor levels in the marine atmosphere favor aging through coagulation with other aerosols, such as sea salt, followed by droplet-phase processes. Thickly coated BC formed under marine conditions generally undergoes regional transport within marine air masses, during which coagulation not only promotes coating formation but also contributes to the growth of BC cores through BC–BC collisions. Consequently, under marine air mass influence (group 2), the observed thickly coated BC cores (lag-times >1.6 μs) were larger than those associated with continental air masses (Fig. 4.2c and Fig. 4.4).

As shown in Figs. 4.2b and 4.5a, when regional transport was dominated by marine air masses (group 2), thickly coated BC accounted for 40-60% of the total BC number concentration in the marine atmosphere, which was substantially higher than the 5-30% observed under continental air mass influence (group 1). This indicates that BC tends to form thickly coated structures more readily during regional transport in the marine environment. As discussed in Chapter 3, freshly emitted BC in marine environments can readily interact with other particles such as sea salt through coagulation, forming attached BC. During regional transport under high relative humidity in marine atmosphere, these attached BC particles are prone to deliquescence and droplet formation, leading to morphological transformation into thickly coated BC. The high fraction (40-60%) of thickly coated BC observed under marine air mass influence in this study further supports the role of the marine environment in shaping BC mixing states, thereby enhancing its light absorption and potential to act as CCN (Bond et al., 2013; Liu et al., 2017).

Figure 4.5b compares the number fraction of thickly coated BC with different core sizes under group 1 and group 2 conditions, revealing that larger BC are more likely to become thickly coated in the marine environment than in continental regions. According to diffusion growth theory (Seinfeld and Pandis, 2006), smaller BC particles are more efficiently coated through condensation and thus more likely to form thickly coated BC. Our observations show that, under both continental and marine air mass influences, the fraction of thickly coated BC exceeds 40% when the BC core size is smaller than 100 nm. However, for BC cores smaller than 100 nm, the fraction of thickly coated BC was significantly lower under continental air mass influence (group 1) than under marine air mass influence (group 2). Under group 1 conditions, the fraction of thickly coated BC decreased markedly with increasing core size, from ~28% to < 10%, consistent with diffusion growth theory and suggesting that BC aging during continental transport is primarily driven by condensation. In contrast, during marine air mass influence (group 2), the fraction of thickly coated BC exhibited relatively little dependence on core size across the 80–

400 nm range, indicating that condensation plays a limited role in BC aging in the marine environment due to the low level of secondary aerosol precursors. As discussed in Chapter 3, BC aging and the formation of thickly coated BC in the marine atmosphere are mainly governed by coagulation and droplet-phase processes.

4.3.3 BC aging in the marine atmosphere

This study further compares the coating thickness of thickly coated BC under group 1 and group 2 conditions. The results show that BC associated with marine air mass-dominated regional transport exhibits thicker coatings than those transported under continental air mass influence. As shown in Figure 4.2d, the median coating thickness of thickly coated BC under continental-dominated conditions (group 1) is typically below 100 nm, whereas that under marine-dominated conditions usually exceeds 100 nm (group 2). This suggests that, although precursor concentrations of secondary components are generally lower in marine environments, BC can undergo a higher degree of aging there than in continental environments. Moreover, Figure 4.4b shows that thickly coated BC under marine-dominated conditions has a larger core median size than that under continental air mass influence, indicating that marine environments favor the formation of aged BC with both larger cores and thicker coatings.

Figures 4.5c and 4.6 show the coating thickness distributions of thickly coated BC. In marine environments, a distinct bimodal distribution is observed, with peaks at 50-100 nm and 100-200 nm. Back-trajectory analysis indicates that thickly coated BC in group 1 air masses remained over the ocean for 1-2 days, shorter than those in group 2 (≥ 3 days). The differences in coating thickness distributions between the two groups suggest that the longer BC is exposed to marine air masses, the more it shifts toward the 100-200 nm mode. This implies that thickly coated BC with coating thicknesses > 100 nm primarily forms under marine conditions. Such observations further indicate that BC can reach aging degree in marine environments that are rarely achieved under continental conditions, likely due to coagulation with marine aerosols (e.g., sea salt) and droplet formation at high relative humidity, which promote the development of thick coatings in marine atmosphere.

This study suggests that marine aging processes play a crucial role in promoting the growth of BC coatings to several hundred nanometers. For BC particles emitted from Europe, coating growth in continental environments typically ranges from only a few to tens of nanometers (Cheng et al., 2018; Laborde et al., 2013; Liu et al., 2014). When transported into the Atlantic marine atmosphere, these particles can develop coatings of several hundred nanometers through coagulation and droplet-phase processes. Such marine-aged BC exhibits significantly enhanced light absorption and can act as CCN, thereby influencing solar radiation and cloud microphysics. Our findings highlight that global climate models should account for the impact of marine environments on BC mixing states, and provide observational constraints for representing BC aging processes over the ocean.

4.4 Summary

Our work elucidates the influence of regional transport on the mass concentration, size, and mixing state of BC in the Atlantic marine atmosphere. BC loading in the marine atmosphere is typically influenced by both continental outflow and maritime emissions, with air masses originating from continental Europe increasing BC mass concentrations by tens to hundreds of ng cm^{-3}. Regional transport within the marine environment substantially increases the number fraction of thickly coated BC, rising from 5-30% under continental air mass influence to more than 50% under marine-dominated conditions. Comparisons of BC mixing states under continental- and marine-dominated transport reveal that marine transport favors the formation of aged BC with larger core sizes and thicker coatings, with coating thicknesses often reaching 100-200 nm. This substantial coating growth is most likely driven by coagulation with marine aerosols such as sea salt, followed by droplet-phase processes under high relative humidity, which can enhance BC aging beyond what is typically observed in continental environments.

Our findings highlight the critical role of the marine environment in enhancing BC aging during regional transport and the formation of thickly coated particles. The presence of BC with coatings of several hundred nanometers in marine air masses has important implications for the global climate system. Such thickly coated BC particles not only significantly increase the direct radiative forcing of BC but also serve as highly efficient cloud condensation nuclei, thereby modulating cloud microphysics. Current estimates of BC's climate effects remain highly uncertain, with model assessments differing by up to an order of magnitude, particularly in representing its direct and indirect radiative impacts (Bond et al., 2013; Matsui et al., 2018; Räisänen et al., 2022). Incorporating the influence of marine environments on BC mixing state and coating growth is therefore essential to more accurately quantify BC's climate forcing in global scale. Our observational results provide crucial empirical evidence to inform and constrain the parameterization of BC aging, mixing state, and associated radiative and microphysical effects in marine regions for future climate modeling efforts, improving predictions of BC's role in global climate change.

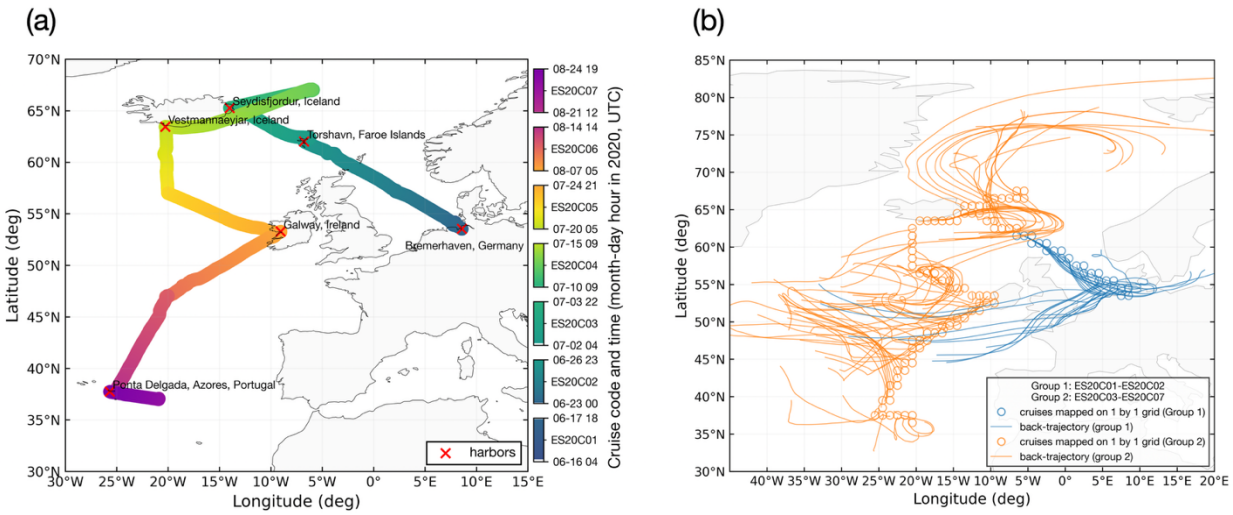

Figure 4.1. (a) Track of S/Y Eugen Seibold during summer 2020 (legs ES20C01–ES20C07), colored by time along the cruise; harbors are marked by red “X”. (b) FLEXPART back-trajectories used to define two air-mass regimes: Group 1 (continental/polluted outflow; orange) and Group 2 (clean-marine inflow; blue). Together these panels summarize the spatial context and the trajectory-based regime separation used throughout.

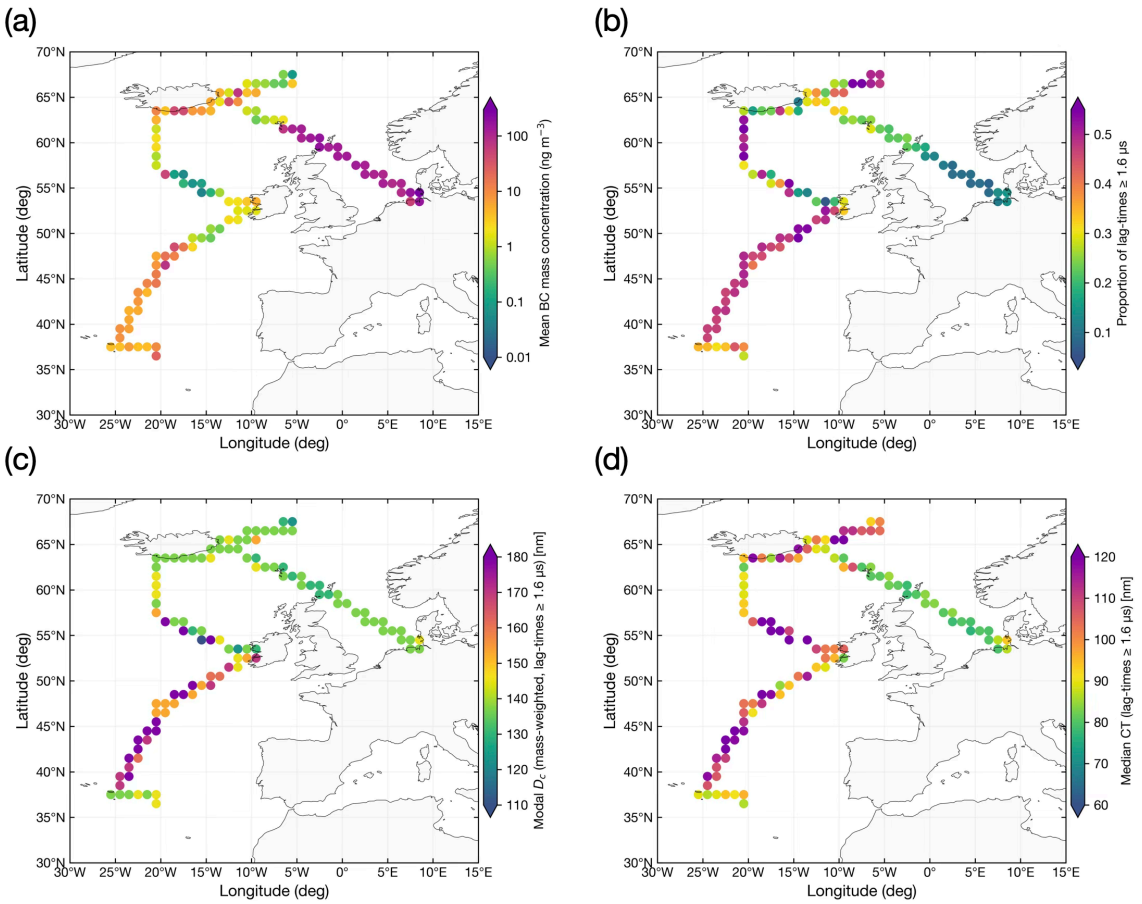

Figure 4.2. Spatial variation of BC loading and mixing-state metrics along the S/Y Eugen Seibold 2020 cruise track, mapped on one-by-one latitude-longitude grid cells. Each filled circle represents the center of a grid cell (cells with <2 samples were excluded); color scale shows the per-cell metric computed from all SP2 samples that fall into that cell. (a) Mean BC mass concentration (ng m^{-3}) averaged over samples in each grid cell; (b) Number fraction of thickly coated BC (lag-time ≥ 1.6 µs) in each cell; (c) Mass-weighted modal core diameter D_c (nm) of thickly coated BC (lag-time ≥ 1.6 µs); (d) Median coating thickness (CT, nm) of thickly coated BC (lag-time ≥ 1.6 µs) in each cell.

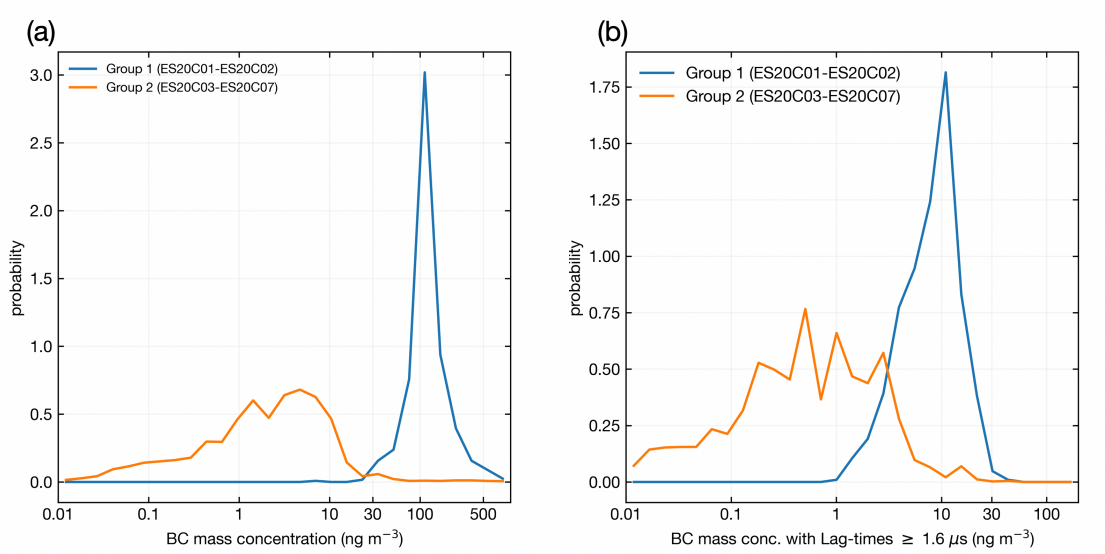

Figure 4.3. Probability distributions functions (PDF) of BC mass concentrations during the cruises in this study under Group-1 (blue lines) and Group-2 (orange lines). (a) PDF of total BC mass concentration (ng m^{-3}); (b) PDF of BC mass concentrations for the thickly coated BC subset (lag-times ≥ 1.6 μs). Curves show normalized probability densities

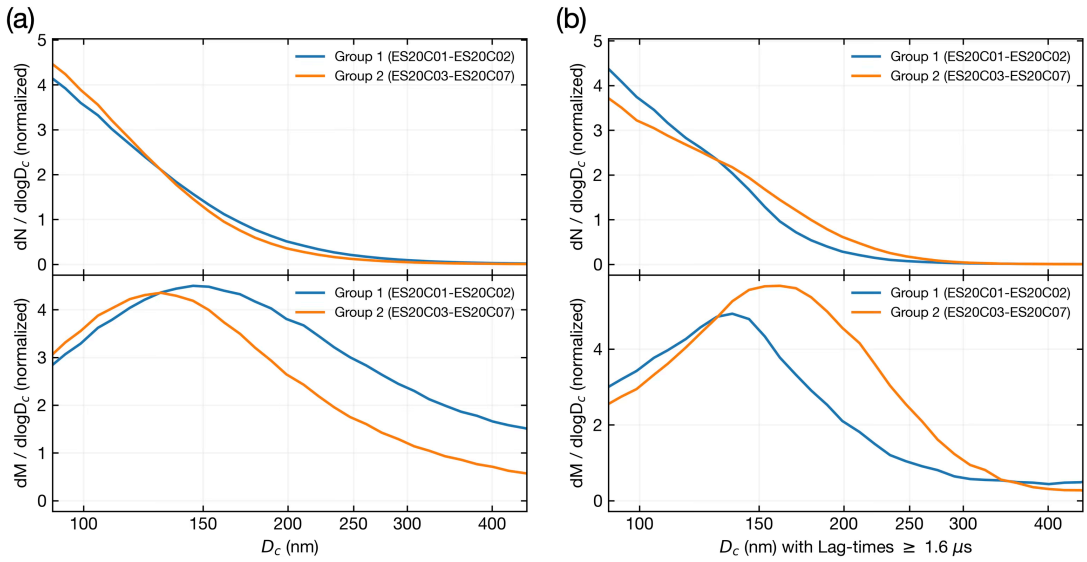

Figure 4.4. (a) Normalized number- and mass-weighted BC core size distributions (dN/dlog(D_c) and dM/dlog(D_c)) for all SP2 measured BC under Group-1 and Group-2 (b) The same diagnostics for the thickly coated BC subset (lag-times ≥ 1.6 μs).

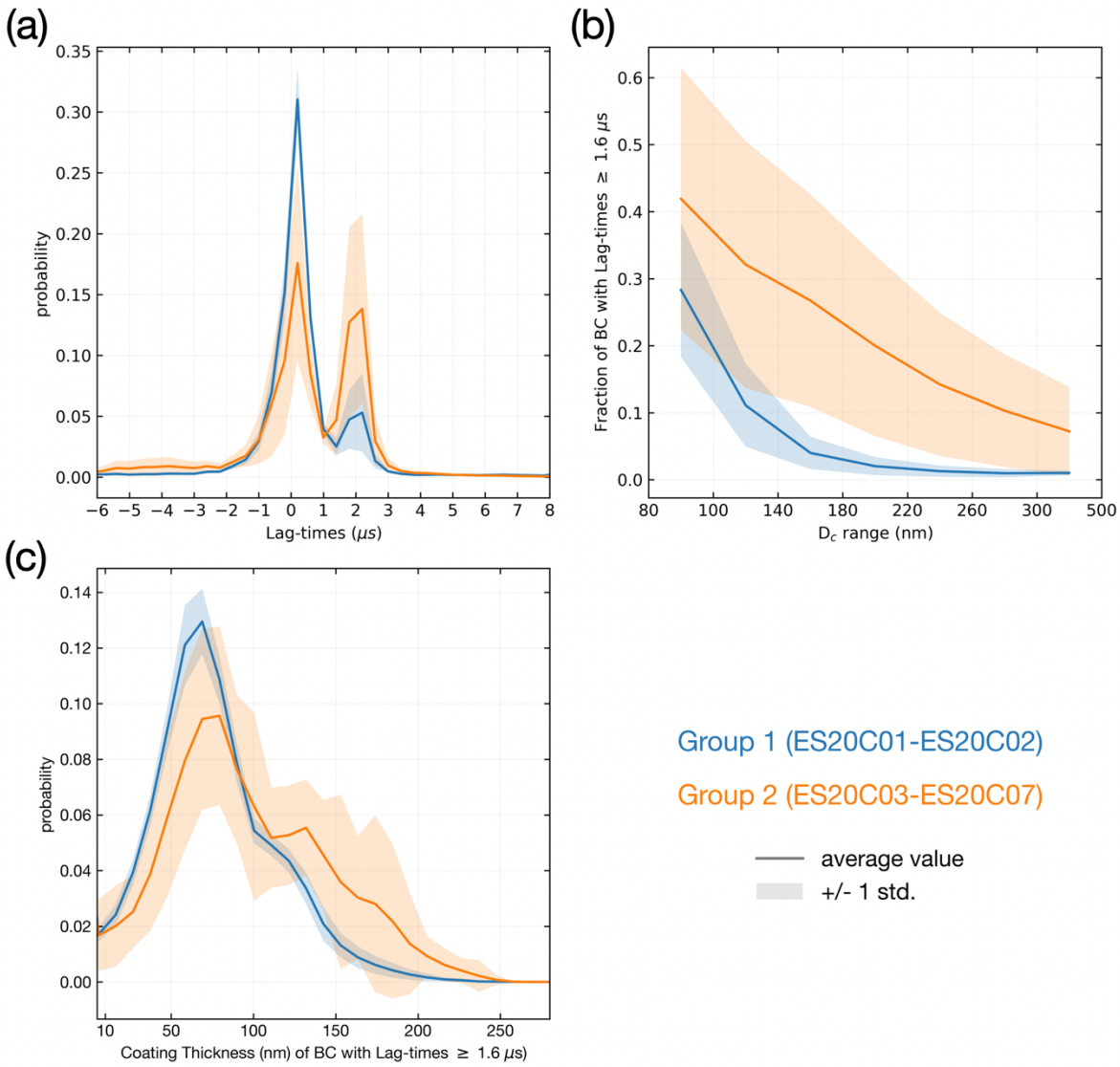

Figure 4.5. Mixing-state metrics for Group-1 (continental-influenced; blue) and Group-2 (marine-dominated; orange) during the S/Y Eugen Seibold 2020 cruises in this study. (a) Probability distributions of SP2 lag-time for BC particles. (b) Number fraction of thickly coated BC (lag-times ≥ 1.6 µs) as a function of core diameter D_c; D_c is binned as 80–100, 100–140, 140–180, 180–220, 220–260, 260–300, and 300–500 nm. (c) Probability distributions of coating thickness (CT) for thickly coated BC (lag-time ≥ 1.6 µs). Curves in all panels show the mean probability (or fraction) across spatial grid cells (one-by-one latitude-longitude cell, align with the Fig. 2); shaded areas show ±1 standard deviation across grid cells and therefore represent spatial variability along the cruise track.

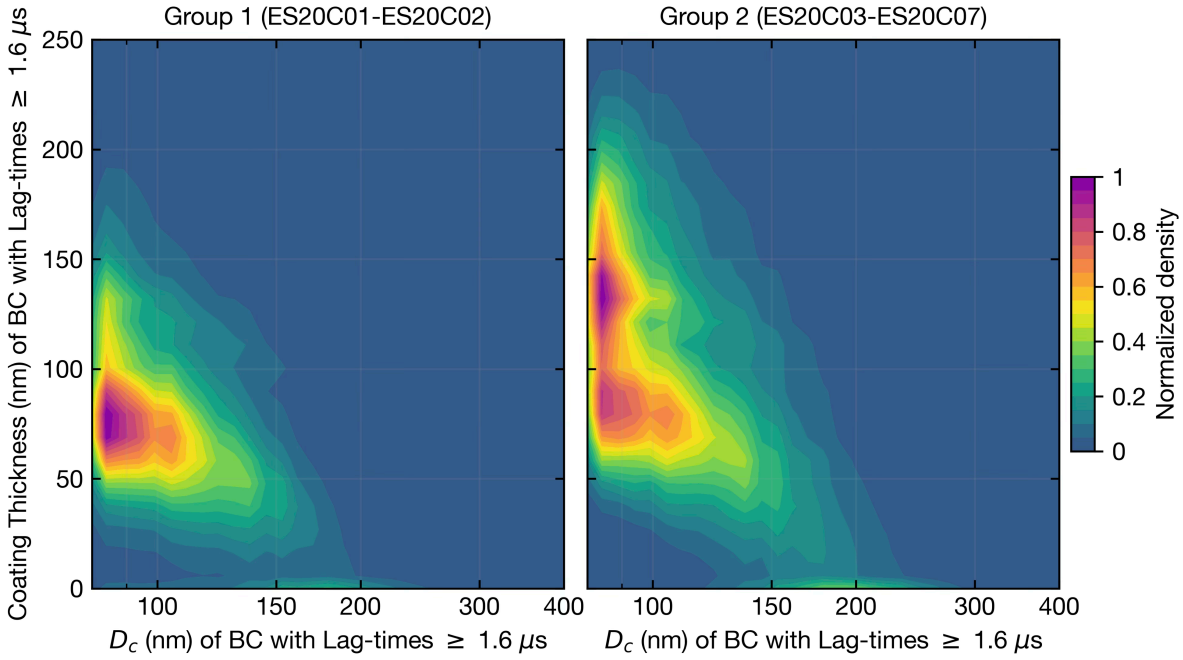

Figure 4.6. Two-dimensional distributions of coating thickness (CT; y-axis, nm) versus BC core diameter for BC with lag-time ≥ 1.6 µs. Left panel: Group 1 (ES20C01–ES20C02). Right panel: Group 2 (ES20C03–ES20C07). Color code indicates the normalized 2-D density of observations in each panel.

Appendix

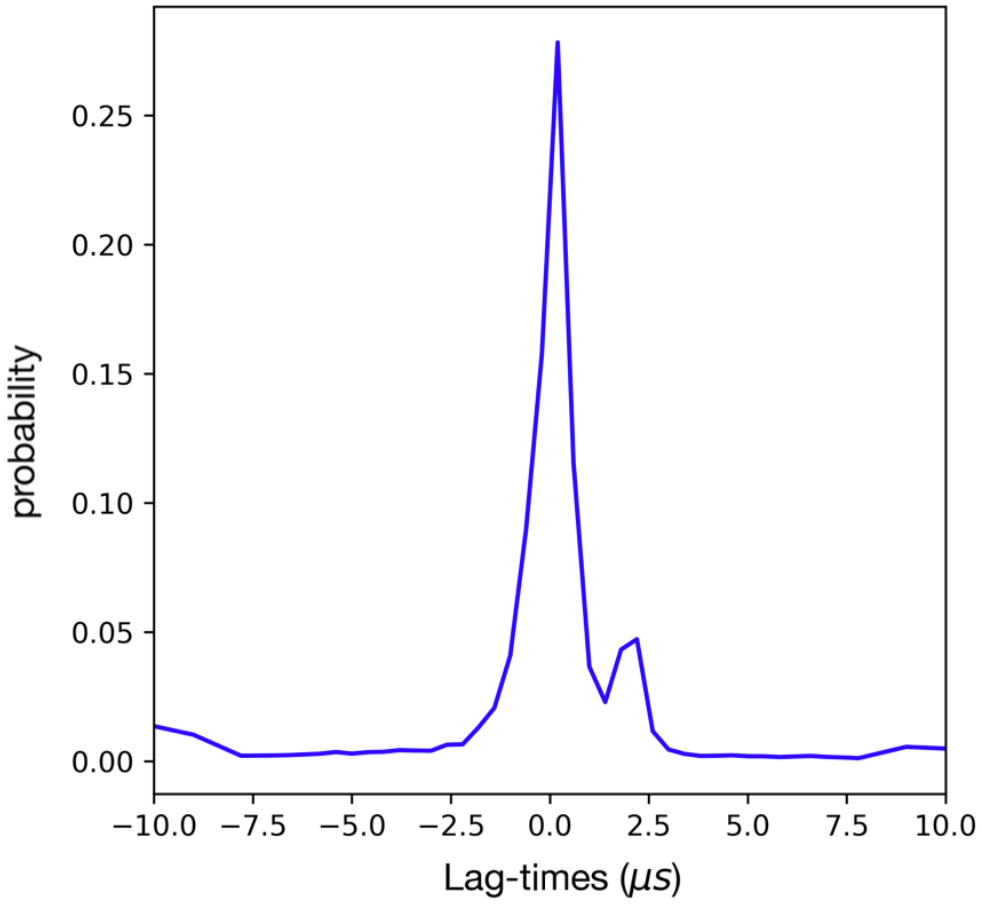

Figure S4.1. Lag-times (μs) probability distribution of all SP2 measured BC particles during the S/Y Eugen Seibold 2020 cruises (ES20C01 - ES20C07) in this study.

Wildfire attribution

The black carbon (BC), organic carbon (OC), and carbon monoxide (CO), and particulate matter (PM2.5) emission fluxes from GFAS emissions (Fig. S2) are assembled over the footprint time window and linearly interpolated to the SRR timestamps and grid. We compute, for each GFAS flux variable v and grid cell i at time t, an incremental contribution sum over time, and integrate the resulting map over the sphere using grid-cell areas A_i:

$$Index_v = \Sigma_i \Sigma_t [SRR(t,i) \times GFAS_v(t,i) \times \Delta t \times A_i] \quad (1)$$

This procedure yields a per-sample wildfire-influence index (kg s^{-1}): $Index_v = 0$ when the retroplume does not intersect active fire grid cells during the integration period, whereas $Index_v > 0$ identifies samples that were influenced by wildfire emissions. The magnitude of $Index_v$ increases with the strength and persistence of overlap between the SRR footprint and active fire regions. Because SRR is a sensitivity field, the integrated values are interpreted as relative indicators of potential smoke influence, rather than as absolute mass loadings.

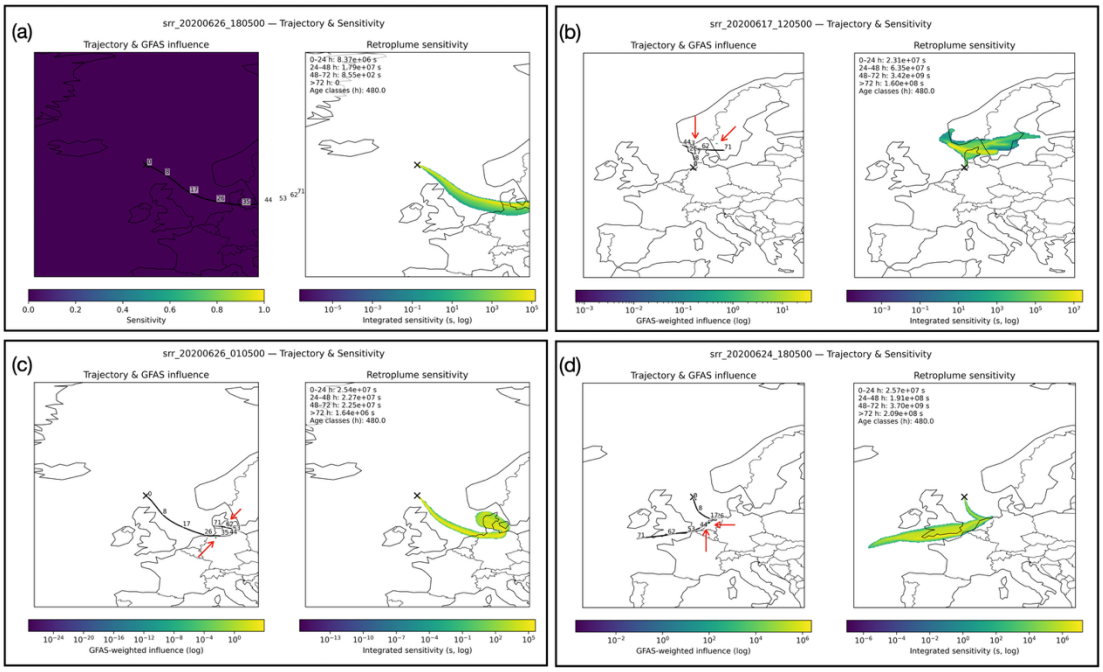

Figure S4.2. FLEXPART diagnostics for four hourly receptor times along the cruise: (a)–(d). Panel (a) illustrates a non-influenced case (no overlap between the retroplume and active fire pixels; near-zero GFAS-weighted field), whereas panels (b)–(d) show cases with plume-fire overlap (indicated by red arrows) and increasing sensitivity along the transport pathway (age-bin summaries indicated in the inset). In each panel, left shows the GFAS-weighted wildfire influence (SRR × GFAS; kg s^{-1}) with the 72-h ensemble-mean back trajectory overlaid and age labels in hours; the receptor is marked by “x”. Right shows the time-integrated retroplume (column SRR; s). All runs release 50 000 particles at 100 m AGL on a 0.1° grid within ±15° of the receptor.

„

Chapter 5 Conclusions and Outlook

This thesis quantified how BC loading and mixing state evolve across the Atlantic and what that implies for climate-relevant properties. It is based on shipborne SP2 measurements aboard the research sailing yacht S/Y Eugen Seibold during June-August 2020, 2022, and 2023, spanning 10–66° N, 10° E–65° W from coastal to remote Atlantic regions and from near-Arctic to near-tropical latitudes. In total, over 1800 hours of observations of single particle SP2 data were collected and presented in this work. To enable rapid, accurate, and consistent analysis, this work developed SPARK, a cross-platform toolkit that converts raw SP2 waveforms into standardized, high-precision per-particle properties. SPARK improves accuracy with refined numerical algorithms, maintains stability via automated drift corrections (laser alignment, baselines, timing), and achieves campaign-scale throughput through parallelization, yielding particle-resolved constraints on BC mass, mass-equivalent core size, optical total size, coating thickness, and lag-time.

The thesis establishes observational baselines of BC mass concentration and mixing state across the Atlantic in chapter 3. BC concentrations cluster around a characteristic marine background of ~100 ng m^{-3} even hundreds of kilometers offshore, indicating a well-mixed marine atmosphere. In contrast, the mixing state varies strongly with environment: near coasts and shipping corridors, freshly emitted BC is dominated by externally attached (non-core-shell) aggregates, suggests the rapid coagulation with marine aerosol (e.g., sea salt); in cleaner, remote marine air, BC is predominantly internally mixed and often thickly coated, reflecting extended marine aging.

Building on these baselines, chapter 4 attributes the observed variabilities to regional transport. Continental-influenced air masses elevate BC loading but exhibit lower fractions of thickly coated BC, consistent with condensation-dominated aging in polluted outflow. In marine-dominated air, overall BC mass is lower, yet the fraction of thickly coated particles increases markedly, with coating thickness and core size both growing during multi-day over-ocean residence. Together, these results reinforce and mechanistically clarify the spatial transitions, highlighting coagulation with marine aerosols and droplet-phase (high-RH) processing as dominant marine-specific BC aging pathways.

Finally, these insights make marine BC treatment in models more realistic by linking optics and lifetime directly to the observed BC concentration and mixing state: (1) Light-absorption enhancement—combine core–shell optics with the measured, regime- and size-resolved distributions of coated fraction and coating thickness to derive environment-specific enhancement E_{abs} (with treating attached, non-core-shell BC that dominates near coasts as essentially unenhanced (E_{abs} ~1); (2) Radiative forcing over the ocean—apply those E_{abs} values so that a more realistic MAC_{BC} in marine environment can be estimated; (3) use the observed mixing-state information to raise hygroscopicity and CCN activation for coated BC (lower activation supersaturation), increasing in-cloud and warm-rain removal pathways, while attached/bare BC remains less CCN-active and longer-lived—keeping absorption, cloud interactions, and lifetime internally consistent rather than tuned separately.

References

Aardema, H. M., Slagter, H. A., Angelis, I. H. de, Calleja, M. Ll., Dragoneas, A., Moretti, S., Schuback, N., Heins, L., Walter, D., Weis, U., Haug, G. H., and Schiebel, R.: On the Variability of Phytoplankton Photophysiology Along a Latitudinal Transect in the North Atlantic Surface Ocean, J. Geophys. Res.: Biogeosciences, 129, https://doi.org/10.1029/2023jg007962, 2024.

Adachi, K. and Buseck, P. R.: Internally mixed soot, sulfates, and organic matter in aerosol particles from Mexico City, Atmos. Chem. Phys., 8, 6469–6481, https://doi.org/10.5194/acp-8-6469-2008, 2008.

Adachi, K., Chung, S. H., and Buseck, P. R.: Shapes of soot aerosol particles and implications for their effects on climate, J. Geophys. Res.: Atmos., 115, https://doi.org/10.1029/2009jd012868, 2010.

Amdahl, G. M.: Validity of the single processor approach to achieving large scale computing capabilities, Proc. April 18-20, 1967, spring Jt. Comput. Conf. - AFIPS '67 (Spring), 483–485, https://doi.org/10.1145/1465482.1465560, 1967.

Andreae, M. O. and Gelencsér, A.: Black carbon or brown carbon? The nature of light-absorbing carbonaceous aerosols, Atmos. Chem. Phys., 6, 3131–3148, https://doi.org/10.5194/acp-6-3131-2006, 2006.

Bakels, L., Tatsii, D., Tipka, A., Thompson, R., Dütsch, M., Blaschek, M., Seibert, P., Baier, K., Bucci, S., Cassiani, M., Eckhardt, S., Zwaaftink, C. G., Henne, S., Kaufmann, P., Lechner, V., Maurer, C., Mulder, M. D., Pisso, I., Plach, A., Subramanian, R., Vojta, M., and Stohl, A.: FLEXPART version 11: improved accuracy, efficiency, and flexibility, Geosci. Model Dev., 17, 7595–7627, https://doi.org/10.5194/gmd-17-7595-2024, 2024.

Bambha, R. P. and Michelsen, H. A.: Effects of aggregate morphology and size on laser-induced incandescence and scattering from black carbon (mature soot), J. Aerosol Sci., 88, 159–181, https://doi.org/10.1016/j.jaerosci.2015.06.006, 2015.

Bhandari, J., China, S., Chandrakar, K. K., Kinney, G., Cantrell, W., Shaw, R. A., Mazzoleni, L. R., Girotto, G., Sharma, N., Gorkowski, K., Gilardoni, S., Decesari, S., Facchini, M. C., Zanca, N., Pavese, G., Esposito, F., Dubey, M. K., Aiken, A. C., Chakrabarty, R. K., Moosmüller, H., Onasch, T. B., Zaveri, R. A., Scarnato, B. V., Fialho, P., and Mazzoleni, C.: Extensive Soot Compaction by Cloud Processing from Laboratory and Field Observations, Sci. Rep., 9, 11824, https://doi.org/10.1038/s41598-019-48143-y, 2019.

BOHREN, C. F. and HUFFMAN, D. R.: Absorption and Scattering of Light by Small Particles, 1983.

Bond, T. C. and Bergstrom, R. W.: Light Absorption by Carbonaceous Particles: An Investigative Review, Aerosol Sci. Technol., 40, 27–67, https://doi.org/10.1080/02786820500421521, 2006.

Bond, T. C., Doherty, S. J., Fahey, D. W., Forster, P. M., Berntsen, T., DeAngelo, B. J., Flanner, M. G., Ghan, S., Kärcher, B., Koch, D., Kinne, S., Kondo, Y., Quinn, P. K., Sarofim, M. C., Schultz, M. G., Schulz, M., Venkataraman, C., Zhang, H., Zhang, S., Bellouin, N., Guttikunda, S. K., Hopke, P. K., Jacobson, M. Z., Kaiser, J. W., Klimont, Z., Lohmann, U., Schwarz, J. P., Shindell, D., Storelvmo, T., Warren, S. G., and Zender, C. S.: Bounding the role of black carbon in the climate system: A scientific assessment, J. Geophys. Res.: Atmos., 118, 5380–5552, https://doi.org/10.1002/jgrd.50171, 2013.

Boyd, S. and Vandenberghe, L.: Convex Optimization, https://doi.org/10.1017/cbo9780511804441.016, 2004.

Buffaloe, G. M., Lack, D. A., Williams, E. J., Coffman, D., Hayden, K. L., Lerner, B. M., Li, S.-M., Nuaaman, I., Massoli, P., Onasch, T. B., Quinn, P. K., and Cappa, C. D.: Black carbon emissions from in-use ships: a California regional assessment, Atmos. Chem. Phys., 14, 1881–1896, https://doi.org/10.5194/acp-14-1881-2014, 2014.

Cappa, C. D., Onasch, T. B., Massoli, P., Worsnop, D. R., Bates, T. S., Cross, E. S., Davidovits, P., Hakala, J., Hayden, K. L., Jobson, B. T., Kolesar, K. R., Lack, D. A., Lerner, B. M., Li, S.-M., Mellon, D., Nuaaman, I., Olfert, J. S., Petäjä, T., Quinn, P. K., Song, C., Subramanian, R., Williams, E. J., and Zaveri, R. A.: Radiative Absorption Enhancements Due to the Mixing State of Atmospheric Black Carbon, Science, 337, 1078–1081, https://doi.org/10.1126/science.1223447, 2012.

Cappa, C. D., Williams, E. J., Lack, D. A., Buffaloe, G. M., Coffman, D., Hayden, K. L., Herndon, S. C., Lerner, B. M., Li, S.-M., Massoli, P., McLaren, R., Nuaaman, I., Onasch, T. B., and Quinn, P. K.: A case study into the measurement of ship emissions from plume intercepts of the NOAA ship *Miller Freeman*, Atmos. Chem. Phys., 14, 1337–1352, https://doi.org/10.5194/acp-14-1337-2014, 2014.

Cappa, C. D., Zhang, X., Russell, L. M., Collier, S., Lee, A. K. Y., Chen, C., Betha, R., Chen, S., Liu, J., Price, D. J., Sanchez, K. J., McMeeking, G. R., Williams, L. R., Onasch, T. B., Worsnop, D. R., Abbatt, J., and Zhang, Q.: Light Absorption by Ambient Black and Brown Carbon and its Dependence on Black Carbon Coating State for Two California, USA, Cities in Winter and Summer, J. Geophys. Res.: Atmos., 124, 1550–1577, https://doi.org/10.1029/2018jd029501, 2019.

Cavalli, F., Viana, M., Yttri, K. E., Genberg, J., and Putaud, J.-P.: Toward a standardised thermal-optical protocol for measuring atmospheric organic and elemental carbon: the EUSAAR protocol, Atmos. Meas. Tech., 3, 79–89, https://doi.org/10.5194/amt-3-79-2010, 2010.

Cheng, Y., Li, S.-M., Gordon, M., and Liu, P.: Size distribution and coating thickness of black carbon from the Canadian oil sands operations, Atmos. Chem. Phys., 18, 2653–2667, https://doi.org/10.5194/acp-18-2653-2018, 2018.

Cheng, Y. F., Su, H., Rose, D., Gunthe, S. S., Berghof, M., Wehner, B., Achtert, P., Nowak, A., Takegawa, N., Kondo, Y., Shiraiwa, M., Gong, Y. G., Shao, M., Hu, M., Zhu, T., Zhang, Y. H., Carmichael, G. R., Wiedensohler, A., Andreae, M. O., and Pöschl, U.: Size-resolved measurement of the mixing state of soot in the megacity Beijing, China: diurnal cycle, aging and parameterization, Atmos. Chem. Phys., 12, 4477–4491, https://doi.org/10.5194/acp-12-4477-2012, 2012.

China, S., Mazzoleni, C., Gorkowski, K., Aiken, A. C., and Dubey, M. K.: Morphology and mixing state of individual freshly emitted wildfire carbonaceous particles, Nat. Commun., 4, 2122, https://doi.org/10.1038/ncomms3122, 2013.

Chow, J. C., Watson, J. G., Chen, L.-W. A., Chang, M. C. O., Robinson, N. F., Trimble, D., and Kohl, S.: The IMPROVE_A Temperature Protocol for Thermal/Optical Carbon Analysis: Maintaining Consistency with a Long-Term Database, J. Air Waste Manag. Assoc., 57, 1014–1023, https://doi.org/10.3155/1047-3289.57.9.1014, 2007.

Coen, M. C., Weingartner, E., Apituley, A., Ceburnis, D., Fierz-Schmidhauser, R., Flentje, H., Henzing, J. S., Jennings, S. G., Moerman, M., Petzold, A., Schmid, O., and Baltensperger, U.: Minimizing light absorption measurement artifacts of the Aethalometer: evaluation of five correction algorithms, Atmos. Meas. Tech., 3, 457–474, https://doi.org/10.5194/amt-3-457-2010, 2010.

Dahlkötter, F., Gysel, M., Sauer, D., Minikin, A., Baumann, R., Seifert, P., Ansmann, A., Fromm, M., Voigt, C., and Weinzierl, B.: The Pagami Creek smoke plume after long-range transport to the upper troposphere over Europe – aerosol properties and black carbon mixing state, Atmos. Chem. Phys., 14, 6111–6137, https://doi.org/10.5194/acp-14-6111-2014, 2014.

Deng, Y., Tanimoto, H., Ikeda, K., Kameyama, S., Okamoto, S., Jung, J., Yoon, Y. J., Yang, E. J., and Kang, S.-H.: Shipborne observations of black carbon aerosols in the western Arctic Ocean during summer and autumn 2016–2020: impact of boreal fires, Atmos. Chem. Phys., 24, 6339–6357, https://doi.org/10.5194/acp-24-6339-2024, 2024.

Diesch, J.-M., Drewnick, F., Klimach, T., and Borrmann, S.: Investigation of gaseous and particulate emissions from various marine vessel types measured on the banks of the Elbe in Northern Germany, Atmos. Chem. Phys., 13, 3603–3618, https://doi.org/10.5194/acp-13-3603-2013, 2013.

Ditas, J., Ma, N., Zhang, Y., Assmann, D., Neumaier, M., Riede, H., Karu, E., Williams, J., Scharffe, D., Wang, Q., Saturno, J., Schwarz, J. P., Katich, J. M., McMeeking, G. R., Zahn, A., Hermann, M., Brenninkmeijer, C. A. M., Andreae, M. O., Pöschl, U., Su, H., and Cheng, Y.: Strong impact of

wildfires on the abundance and aging of black carbon in the lowermost stratosphere, Proc. Natl. Acad. Sci., 115, E11595–E11603, https://doi.org/10.1073/pnas.1806868115, 2018.

Droplet-Measurement-Technologies: PSI Toolkit Single Particle Soot Photometer (SP2) Operator Manual DOC-0359 Revision B Tool Kit v4.116, https://www.dropletmeasurement.com/manual/software-manual-sp2-psi-toolkit/, 2022a.

Droplet-Measurement-Technologies: Single Particle Soot Photometer (SP2) Software Manual DOC-0092 Rev G Version 4 Software, 2022b.

Dubovik, O. and King, M. D.: A flexible inversion algorithm for retrieval of aerosol optical properties from Sun and sky radiance measurements, J. Geophys. Res.: Atmos., 105, 20673–20696, https://doi.org/10.1029/2000jd900282, 2000.

Fierce, L., Riemer, N., and Bond, T. C.: Explaining variance in black carbon's aging timescale, Atmos. Chem. Phys., 15, 3173–3191, https://doi.org/10.5194/acp-15-3173-2015, 2015.

Fierce, L., Onasch, T. B., Cappa, C. D., Mazzoleni, C., China, S., Bhandari, J., Davidovits, P., Fischer, D. A., Helgestad, T., Lambe, A. T., Sedlacek, A. J., Smith, G. D., and Wolff, L.: Radiative absorption enhancements by black carbon controlled by particle-to-particle heterogeneity in composition, Proc. Natl. Acad. Sci., 117, 5196–5203, https://doi.org/10.1073/pnas.1919723117, 2020.

Fossum, K. N., Ovadnevaite, J., Liu, D., Flynn, M., O'Dowd, C., and Ceburnis, D.: Background levels of black carbon over remote marine locations, Atmos. Res., 271, 106119, https://doi.org/10.1016/j.atmosres.2022.106119, 2022.

Fuller, K. A., Malm, W. C., and Kreidenweis, S. M.: Effects of mixing on extinction by carbonaceous particles, J. Geophys. Res.: Atmos., 104, 15941–15954, https://doi.org/10.1029/1998jd100069, 1999.

Gao, R. S., Schwarz, J. P., Kelly, K. K., Fahey, D. W., Watts, L. A., Thompson, T. L., Spackman, J. R., Slowik, J. G., Cross, E. S., Han, J.-H., Davidovits, P., Onasch, T. B., and Worsnop, D. R.: A Novel Method for Estimating Light-Scattering Properties of Soot Aerosols Using a Modified Single-Particle Soot Photometer, Aerosol Sci. Technol., 41, 125–135, https://doi.org/10.1080/02786820601118398, 2007.

(GMTDS), G. M. T. D. S.: Global Maritime Traffic Density Data, 2024.

Gong, X., Zhang, C., Chen, H., Nizkorodov, S. A., Chen, J., and Yang, X.: Size distribution and mixing state of black carbon particles during a heavy air pollution episode in Shanghai, Atmos. Chem. Phys., 16, 5399–5411, https://doi.org/10.5194/acp-16-5399-2016, 2016.

Gysel, M., Laborde, M., Olfert, J. S., Subramanian, R., and Gröhn, A. J.: Effective density of Aquadag and fullerene soot black carbon reference materials used for SP2 calibration, Atmos. Meas. Tech., 4, 2851–2858, https://doi.org/10.5194/amt-4-2851-2011, 2011.

Hadley, O. L., Ramanathan, V., Carmichael, G. R., Tang, Y., Corrigan, C. E., Roberts, G. C., and Mauger, G. S.: Trans-Pacific transport of black carbon and fine aerosols (D < 2.5 μm) into North America, J. Geophys. Res.: Atmos., 112, https://doi.org/10.1029/2006jd007632, 2007.

He, C., Liou, K.-N., Takano, Y., Zhang, R., Zamora, M. L., Yang, P., Li, Q., and Leung, L. R.: Variation of the radiative properties during black carbon aging: theoretical and experimental intercomparison, Atmos. Chem. Phys., 15, 11967–11980, https://doi.org/10.5194/acp-15-11967-2015, 2015.

Holanda, B. A., Pöhlker, M. L., Walter, D., Saturno, J., Sörgel, M., Ditas, J., Ditas, F., Schulz, C., Franco, M. A., Wang, Q., Donth, T., Artaxo, P., Barbosa, H. M. J., Borrmann, S., Braga, R., Brito, J., Cheng, Y., Dollner, M., Kaiser, J. W., Klimach, T., Knote, C., Krüger, O. O., Fütterer, D., Lavrič, J. V., Ma, N., Machado, L. A. T., Ming, J., Morais, F. G., Paulsen, H., Sauer, D., Schlager, H., Schneider, J., Su, H., Weinzierl, B., Walser, A., Wendisch, M., Ziereis, H., Zöger, M., Pöschl, U., Andreae, M. O., and Pöhlker, C.: Influx of African biomass burning aerosol during the Amazonian dry season through layered transatlantic transport of black carbon-rich smoke, Atmos. Chem. Phys., 20, 4757–4785, https://doi.org/10.5194/acp-20-4757-2020, 2020.

Holben, B. N., Tanré, D., Smirnov, A., Eck, T. F., Slutsker, I., Abuhassan, N., Newcomb, W. W., Schafer, J. S., Chatenet, B., Lavenu, F., Kaufman, Y. J., Castle, J. V., Setzer, A., Markham, B., Clark, D., Frouin, R., Halthore, R., Karneli, A., O'Neill, N. T., Pietras, C., Pinker, R. T., Voss, K., and Zibordi, G.: An emerging ground-based aerosol climatology: Aerosol optical depth from AERONET, J. Geophys. Res.: Atmos., 106, 12067–12097, https://doi.org/10.1029/2001jd900014, 2001.

IPCC: Climate Change 2013 – The Physical Science Basis, 2014.

IPCC: Climate Change 2021 – The Physical Science Basis, 2023.

Jacobson, M. Z.: Strong radiative heating due to the mixing state of black carbon in atmospheric aerosols, Nature, 409, 695–697, https://doi.org/10.1038/35055518, 2001.

Janssen, N. A. H., Hoek, G., Simic-Lawson, M., Fischer, P., Bree, L. van, Brink, H. ten, Keuken, M., Atkinson, R. W., Anderson, H. R., Brunekreef, B., and Cassee, F. R.: Black Carbon as an Additional Indicator of the Adverse Health Effects of Airborne Particles Compared with PM10 and PM2.5, Environ. Heal. Perspect., 119, 1691–1699, https://doi.org/10.1289/ehp.1003369, 2011.

Jurányi, Z., Zanatta, M., Lund, M. T., Samset, B. H., Skeie, R. B., Sharma, S., Wendisch, M., and Herber, A.: Atmospheric concentrations of black carbon are substantially higher in spring than

summer in the Arctic, Commun. Earth Environ., 4, 91, https://doi.org/10.1038/s43247-023-00749-x, 2023.

Kaiser, J. W., Heil, A., Andreae, M. O., Benedetti, A., Chubarova, N., Jones, L., Morcrette, J.-J., Razinger, M., Schultz, M. G., Suttie, M., and Werf, G. R. van der: Biomass burning emissions estimated with a global fire assimilation system based on observed fire radiative power, Biogeosciences, 9, 527–554, https://doi.org/10.5194/bg-9-527-2012, 2012.

Kärcher, B.: Formation and radiative forcing of contrail cirrus, Nat. Commun., 9, 1824, https://doi.org/10.1038/s41467-018-04068-0, 2018.

Katich, J. M., Samset, B. H., Bui, T. P., Dollner, M., Froyd, K. D., Campuzano-Jost, P., Nault, B. A., Schroder, J. C., Weinzierl, B., and Schwarz, J. P.: Strong Contrast in Remote Black Carbon Aerosol Loadings Between the Atlantic and Pacific Basins, J. Geophys. Res.: Atmos., 123, 13,386-13,395, https://doi.org/10.1029/2018jd029206, 2018.

Khaykin, S., Legras, B., Bucci, S., Sellitto, P., Isaksen, L., Tencé, F., Bekki, S., Bourassa, A., Rieger, L., Zawada, D., Jumelet, J., and Godin-Beekmann, S.: The 2019/20 Australian wildfires generated a persistent smoke-charged vortex rising up to 35 km altitude, Commun. Earth Environ., 1, 22, https://doi.org/10.1038/s43247-020-00022-5, 2020.

Kirrane, E. F., Luben, T. J., Benson, A., Owens, E. O., Sacks, J. D., Dutton, S. J., Madden, M., and Nichols, J. L.: A systematic review of cardiovascular responses associated with ambient black carbon and fine particulate matter, Environ. Int., 127, 305–316, https://doi.org/10.1016/j.envint.2019.02.027, 2019.

Klimont, Z., Kupiainen, K., Heyes, C., Purohit, P., Cofala, J., Rafaj, P., Borken-Kleefeld, J., and Schöpp, W.: Global anthropogenic emissions of particulate matter including black carbon, Atmos. Chem. Phys., 17, 8681–8723, https://doi.org/10.5194/acp-17-8681-2017, 2017.

Ko, J., Krasowsky, T., and Ban-Weiss, G.: Measurements to determine the mixing state of black carbon emitted from the 2017–2018 California wildfires and urban Los Angeles, Atmos. Chem. Phys., 20, 15635–15664, https://doi.org/10.5194/acp-20-15635-2020, 2020.

Koch, D. and Genio, A. D. D.: Black carbon semi-direct effects on cloud cover: review and synthesis, Atmos. Chem. Phys., 10, 7685–7696, https://doi.org/10.5194/acp-10-7685-2010, 2010.

Laborde, M., Mertes, P., Zieger, P., Dommen, J., Baltensperger, U., and Gysel, M.: Sensitivity of the Single Particle Soot Photometer to different black carbon types, Atmos. Meas. Tech., 5, 1031–1043, https://doi.org/10.5194/amt-5-1031-2012, 2012.

Laborde, M., Crippa, M., Tritscher, T., Jurányi, Z., Decarlo, P. F., Temime-Roussel, B., Marchand, N., Eckhardt, S., Stohl, A., Baltensperger, U., Prévôt, A. S. H., Weingartner, E., and Gysel, M.:

Black carbon physical properties and mixing state in the European megacity Paris, Atmos. Chem. Phys., 13, 5831–5856, https://doi.org/10.5194/acp-13-5831-2013, 2013.

Lack, D. A. and Cappa, C. D.: Impact of brown and clear carbon on light absorption enhancement, single scatter albedo and absorption wavelength dependence of black carbon, Atmos. Chem. Phys., 10, 4207–4220, https://doi.org/10.5194/acp-10-4207-2010, 2010.

Lack, D. A., Moosmüller, H., McMeeking, G. R., Chakrabarty, R. K., and Baumgardner, D.: Characterizing elemental, equivalent black, and refractory black carbon aerosol particles: a review of techniques, their limitations and uncertainties, Anal. Bioanal. Chem., 406, 99–122, https://doi.org/10.1007/s00216-013-7402-3, 2014.

Laskin, A., Laskin, J., and Nizkorodov, S. A.: Chemistry of Atmospheric Brown Carbon, Chem. Rev., 115, 4335–4382, https://doi.org/10.1021/cr5006167, 2015.

Li, J., Carlson, B. E., Yung, Y. L., Lv, D., Hansen, J., Penner, J. E., Liao, H., Ramaswamy, V., Kahn, R. A., Zhang, P., Dubovik, O., Ding, A., Lacis, A. A., Zhang, L., and Dong, Y.: Scattering and absorbing aerosols in the climate system, Nat. Rev. Earth Environ., 3, 363–379, https://doi.org/10.1038/s43017-022-00296-7, 2022.

Liu, D., Allan, J. D., Young, D. E., Coe, H., Beddows, D., Fleming, Z. L., Flynn, M. J., Gallagher, M. W., Harrison, R. M., Lee, J., Prevot, A. S. H., Taylor, J. W., Yin, J., Williams, P. I., and Zotter, P.: Size distribution, mixing state and source apportionment of black carbon aerosol in London during wintertime, Atmos. Chem. Phys., 14, 10061–10084, https://doi.org/10.5194/acp-14-10061-2014, 2014.

Liu, D., Whitehead, J., Alfarra, M. R., Reyes-Villegas, E., Spracklen, D. V., Reddington, C. L., Kong, S., Williams, P. I., Ting, Y.-C., Haslett, S., Taylor, J. W., Flynn, M. J., Morgan, W. T., McFiggans, G., Coe, H., and Allan, J. D.: Black-carbon absorption enhancement in the atmosphere determined by particle mixing state, Nat. Geosci., 10, 184–188, https://doi.org/10.1038/ngeo2901, 2017.

Liu, D., Joshi, R., Wang, J., Yu, C., Allan, J. D., Coe, H., Flynn, M. J., Xie, C., Lee, J., Squires, F., Kotthaus, S., Grimmond, S., Ge, X., Sun, Y., and Fu, P.: Contrasting physical properties of black carbon in urban Beijing between winter and summer, Atmos. Chem. Phys., 19, 6749–6769, https://doi.org/10.5194/acp-19-6749-2019, 2019.

Liu, D., He, C., Schwarz, J. P., and Wang, X.: Lifecycle of light-absorbing carbonaceous aerosols in the atmosphere, npj Clim. Atmos. Sci., 3, 40, https://doi.org/10.1038/s41612-020-00145-8, 2020.

Liu, F. and Snelling, D. R.: The unsteady-state energy conservation equation for a small spherical particle in LII modeling, Appl. Phys. B, 89, 115–121, https://doi.org/10.1007/s00340-007-2761-0, 2007.

Ma, C., Ni, R., Su, H., and Cheng, Y.: Enhancing Global Simulation of Smoke Injection Height for Intense Pyro-Convection Through Coupling an Improved One-Dimensional Plume Rise Model in CAM-chem, J. Adv. Model. Earth Syst., 16, https://doi.org/10.1029/2023ms004127, 2024.

Matsui, H., Hamilton, D. S., and Mahowald, N. M.: Black carbon radiative effects highly sensitive to emitted particle size when resolving mixing-state diversity, Nat. Commun., 9, 3446, https://doi.org/10.1038/s41467-018-05635-1, 2018.

Melton, L. A.: Soot diagnostics based on laser heating, Appl. Opt., 23, 2201, https://doi.org/10.1364/ao.23.002201, 1984.

Metcalf, A. R., Craven, J. S., Ensberg, J. J., Brioude, J., Angevine, W., Sorooshian, A., Duong, H. T., Jonsson, H. H., Flagan, R. C., and Seinfeld, J. H.: Black carbon aerosol over the Los Angeles Basin during CalNex, J. Geophys. Res.: Atmos., 117, https://doi.org/10.1029/2011jd017255, 2012.

Michelsen, H. A., Liu, F., Kock, B. F., Bladh, H., Boiarciuc, A., Charwath, M., Dreier, T., Hadef, R., Hofmann, M., Reimann, J., Will, S., Bengtsson, P.-E., Bockhorn, H., Foucher, F., Geigle, K.-P., Mounaïm-Rousselle, C., Schulz, C., Stirn, R., Tribalet, B., and Suntz, R.: Modeling laser-induced incandescence of soot: a summary and comparison of LII models, Appl. Phys. B, 87, 503–521, https://doi.org/10.1007/s00340-007-2619-5, 2007.

Michelsen, H. A., Schulz, C., Smallwood, G. J., and Will, S.: Laser-induced incandescence: Particulate diagnostics for combustion, atmospheric, and industrial applications, Prog. Energy Combust. Sci., 51, 2–48, https://doi.org/10.1016/j.pecs.2015.07.001, 2015.

Moteki, N.: Climate-relevant properties of black carbon aerosols revealed by in situ measurements: a review, Prog. Earth Planet. Sci., 10, 12, https://doi.org/10.1186/s40645-023-00544-4, 2023.

Moteki, N. and Kondo, Y.: Effects of Mixing State on Black Carbon Measurements by Laser-Induced Incandescence, Aerosol Sci. Technol., 41, 398–417, https://doi.org/10.1080/02786820701199728, 2007.

Moteki, N. and Kondo, Y.: Method to measure time-dependent scattering cross sections of particles evaporating in a laser beam, J. Aerosol Sci., 39, 348–364, https://doi.org/10.1016/j.jaerosci.2007.12.002, 2008.

Moteki, N. and Kondo, Y.: Dependence of Laser-Induced Incandescence on Physical Properties of Black Carbon Aerosols: Measurements and Theoretical Interpretation, Aerosol Sci. Technol., 44, 663–675, https://doi.org/10.1080/02786826.2010.484450, 2010.

Moteki, N., Kondo, Y., and Nakamura, S.: Method to measure refractive indices of small nonspherical particles: Application to black carbon particles, J. Aerosol Sci., 41, 513–521, https://doi.org/10.1016/j.jaerosci.2010.02.013, 2010.

Moteki, N., Kondo, Y., and Adachi, K.: Identification by single-particle soot photometer of black carbon particles attached to other particles: Laboratory experiments and ground observations in Tokyo, J. Geophys. Res.: Atmos., 119, 1031–1043, https://doi.org/10.1002/2013jd020655, 2014.

Naseri, A., Corbin, J. C., and Olfert, J. S.: Comparison of the LEO and CPMA-SP2 techniques for black-carbon mixing-state measurements, Atmos. Meas. Tech., 17, 3719–3738, https://doi.org/10.5194/amt-17-3719-2024, 2024.

Ni, R., Su, H., Burnett, R. T., Guo, Y., and Cheng, Y.: Long-term exposure to PM2.5 has significant adverse effects on childhood and adult asthma: A global meta-analysis and health impact assessment, One Earth, 7, 1953–1969, https://doi.org/10.1016/j.oneear.2024.09.022, 2024.

Pagels, J., Khalizov, A. F., McMurry, P. H., and Zhang, R. Y.: Processing of Soot by Controlled Sulphuric Acid and Water Condensation—Mass and Mobility Relationship, Aerosol Sci. Technol., 43, 629–640, https://doi.org/10.1080/02786820902810685, 2009.

Peng, J., Hu, M., Guo, S., Du, Z., Zheng, J., Shang, D., Zamora, M. L., Zeng, L., Shao, M., Wu, Y.-S., Zheng, J., Wang, Y., Glen, C. R., Collins, D. R., Molina, M. J., and Zhang, R.: Markedly enhanced absorption and direct radiative forcing of black carbon under polluted urban environments, Proc. Natl. Acad. Sci., 113, 4266–4271, https://doi.org/10.1073/pnas.1602310113, 2016.

Peterson, D. A., Campbell, J. R., Hyer, E. J., Fromm, M. D., Kablick, G. P., Cossuth, J. H., and DeLand, M. T.: Wildfire-driven thunderstorms cause a volcano-like stratospheric injection of smoke, npj Clim. Atmos. Sci., 1, 30, https://doi.org/10.1038/s41612-018-0039-3, 2018.

Petters, M. D. and Kreidenweis, S. M.: A single parameter representation of hygroscopic growth and cloud condensation nucleus activity, Atmos. Chem. Phys., 7, 1961–1971, https://doi.org/10.5194/acp-7-1961-2007, 2007.

Petzold, A., Ogren, J. A., Fiebig, M., Laj, P., Li, S.-M., Baltensperger, U., Holzer-Popp, T., Kinne, S., Pappalardo, G., Sugimoto, N., Wehrli, C., Wiedensohler, A., and Zhang, X.-Y.: Recommendations for reporting “black carbon” measurements, Atmos. Chem. Phys., 13, 8365–8379, https://doi.org/10.5194/acp-13-8365-2013, 2013.

Pöschl, U.: Atmospheric Aerosols: Composition, Transformation, Climate and Health Effects, Angew. Chem. Int. Ed., 44, 7520–7540, https://doi.org/10.1002/anie.200501122, 2005.

Räisänen, P., Merikanto, J., Makkonen, R., Savolahti, M., Kirkevåg, A., Sand, M., Seland, Ø., and Partanen, A.-I.: Mapping the dependence of black carbon radiative forcing on emission region and season, Atmos. Chem. Phys., 22, 11579–11602, https://doi.org/10.5194/acp-22-11579-2022, 2022.

Ramanathan, V. and Carmichael, G.: Global and regional climate changes due to black carbon, Nat. Geosci., 1, 221–227, https://doi.org/10.1038/ngeo156, 2008.

Riemer, N., West, M., Zaveri, R., and Easter, R.: Estimating black carbon aging time-scales with a particle-resolved aerosol model, J. Aerosol Sci., 41, 143–158, https://doi.org/10.1016/j.jaerosci.2009.08.009, 2010.

Riemer, N., Ault, A. P., West, M., Craig, R. L., and Curtis, J. H.: Aerosol Mixing State: Measurements, Modeling, and Impacts, Rev. Geophys., 57, 187–249, https://doi.org/10.1029/2018rg000615, 2019.

Samset, B. H. and Myhre, G.: Vertical dependence of black carbon, sulphate and biomass burning aerosol radiative forcing, Geophys. Res. Lett., 38, n/a-n/a, https://doi.org/10.1029/2011gl049697, 2011.

Samset, B. H., Myhre, G., Herber, A., Kondo, Y., Li, S.-M., Moteki, N., Koike, M., Oshima, N., Schwarz, J. P., Balkanski, Y., Bauer, S. E., Bellouin, N., Berntsen, T. K., Bian, H., Chin, M., Diehl, T., Easter, R. C., Ghan, S. J., Iversen, T., Kirkevåg, A., Lamarque, J.-F., Lin, G., Liu, X., Penner, J. E., Schulz, M., Seland, Ø., Skeie, R. B., Stier, P., Takemura, T., Tsigaridis, K., and Zhang, K.: Modelled black carbon radiative forcing and atmospheric lifetime in AeroCom Phase II constrained by aircraft observations, Atmos. Chem. Phys., 14, 12465–12477, https://doi.org/10.5194/acp-14-12465-2014, 2014.

Schiebel, R., Aardema, H. M., Calleja, M. Ll., Dragoneas, A., Heins, L., Angelis, I. H. de, Pöhlker, C., Slagter, H., Vonhof, H., Walter, D., Arns, A. I., Adolphs, N., Auderset, A., Basic, S., Bieler, A., Brüwer, J. D., Chaabane, S., Cheng, Y., Chiliński, M. T., Cybulski, J. D., Disper, T., Duprey, N., Eichele, G., Fiedler, B., Fischer, A., Foreman, A. D., Fuchs, B. M., Galer, S., Härri, J., Jochum, K. P., Jost, A., Jung, J., Kleta, H., Lammel, G., Larink, O., Leibold, P., Martínez-García, A., Moretti, S., Müller, J., Nillius, B., Pan, X., Raj, S. S., Repschläger, J., Rodrigues, E., Ruff, S. E., Schmitt, M., Schmitter, J. L., Lara, A. S., Silva, P., Smart, S. M., Sörgel, M., Stoll, B., Su, H., Vogt, M., Wald, T., Weber, B., Weber, J., Weis, U., Amann, R., Arístegui, J., Dittmar, T., González, M., O'Dea, A., Pöschl, U., and Haug, G. H.: Preface: Special Issue on Probing the Open Ocean With the Research Sailing Yacht Eugen Seibold for Climate Geochemistry, J. Geophys. Res.: Atmos., 129, https://doi.org/10.1029/2023jd040581, 2024.

Schulz, C., Kock, B. F., Hofmann, M., Michelsen, H., Will, S., Bougie, B., Suntz, R., and Smallwood, G.: Laser-induced incandescence: recent trends and current questions, Appl. Phys. B, 83, 333, https://doi.org/10.1007/s00340-006-2260-8, 2006a.

Schulz, H., Zanatta, M., Bozem, H., Leaitch, W. R., Herber, A. B., Burkart, J., Willis, M. D., Kunkel, D., Hoor, P. M., Abbatt, J. P. D., and Gerdes, R.: High Arctic aircraft measurements characterising black carbon vertical variability in spring and summer, Atmos. Chem. Phys., 19, 2361–2384, https://doi.org/10.5194/acp-19-2361-2019, 2019.

Schulz, M., Textor, C., Kinne, S., Balkanski, Y., Bauer, S., Berntsen, T., Berglen, T., Boucher, O., Dentener, F., Guibert, S., Isaksen, I. S. A., Iversen, T., Koch, D., Kirkevåg, A., Liu, X., Montanaro, V., Myhre, G., Penner, J. E., Pitari, G., Reddy, S., Seland, Ø., Stier, P., and Takemura, T.: Radiative forcing by aerosols as derived from the AeroCom present-day and pre-industrial simulations, Atmos. Chem. Phys., 6, 5225–5246, https://doi.org/10.5194/acp-6-5225-2006, 2006b.

Schwarz, J. P., Gao, R. S., Fahey, D. W., Thomson, D. S., Watts, L. A., Wilson, J. C., Reeves, J. M., Darbeheshti, M., Baumgardner, D. G., Kok, G. L., Chung, S. H., Schulz, M., Hendricks, J., Lauer, A., Kärcher, B., Slowik, J. G., Rosenlof, K. H., Thompson, T. L., Langford, A. O., Loewenstein, M., and Aikin, K. C.: Single-particle measurements of midlatitude black carbon and light-scattering aerosols from the boundary layer to the lower stratosphere, J. Geophys. Res.: Atmos., 111, https://doi.org/10.1029/2006jd007076, 2006.

Schwarz, J. P., Gao, R. S., Spackman, J. R., Watts, L. A., Thomson, D. S., Fahey, D. W., Ryerson, T. B., Peischl, J., Holloway, J. S., Trainer, M., Frost, G. J., Baynard, T., Lack, D. A., Gouw, J. A. de, Warneke, C., and Negro, L. A. D.: Measurement of the mixing state, mass, and optical size of individual black carbon particles in urban and biomass burning emissions, Geophys. Res. Lett., 35, https://doi.org/10.1029/2008gl033968, 2008.

Schwarz, J. P., Perring, A. E., Markovic, M. Z., Gao, R. S., Ohata, S., Langridge, J., Law, D., McLaughlin, R., and Fahey, D. W.: Technique and theoretical approach for quantifying the hygroscopicity of black-carbon-containing aerosol using a single particle soot photometer, J. Aerosol Sci., 81, 110–126, https://doi.org/10.1016/j.jaerosci.2014.11.009, 2015.

Schwarz, J. P., Weinzierl, B., Samset, B. H., Dollner, M., Heimerl, K., Markovic, M. Z., Perring, A. E., and Ziemba, L.: Aircraft measurements of black carbon vertical profiles show upper tropospheric variability and stability, Geophys. Res. Lett., 44, 1132–1140, https://doi.org/10.1002/2016gl071241, 2017.

Schwarz, Joshua. P., Katich, J. M., Lee, S. L., Thomson, D. S., and Watts, L. A.: “Invisible bias” in the single particle soot photometer due to trigger deadtime, Aerosol Sci. Technol., 56, 623–635, https://doi.org/10.1080/02786826.2022.2064265, 2022.

Sedlacek, A. J., Lewis, E. R., Kleinman, L., Xu, J., and Zhang, Q.: Determination of and evidence for non-core-shell structure of particles containing black carbon using the Single-Particle Soot Photometer (SP2), Geophys. Res. Lett., 39, n/a-n/a, https://doi.org/10.1029/2012gl050905, 2012.

Sedlacek, A. J., Lewis, E. R., Onasch, T. B., Lambe, A. T., and Davidovits, P.: Investigation of Refractory Black Carbon-Containing Particle Morphologies Using the Single-Particle Soot Photometer (SP2), Aerosol Sci. Technol., 49, 872–885, https://doi.org/10.1080/02786826.2015.1074978, 2015.

Seinfeld, J. H. and Pandis, S. N.: ATMOSPHERIC CHEMISTRY AND PHYSICS, 2006.

Stephens, M., Turner, N., and Sandberg, J.: Particle identification by laser-induced incandescence in a solid-state laser cavity, Appl. Opt., 42, 3726, https://doi.org/10.1364/ao.42.003726, 2003.

Subramanian, R., Kok, G. L., Baumgardner, D., Clarke, A., Shinozuka, Y., Campos, T. L., Heizer, C. G., Stephens, B. B., Foy, B. de, Voss, P. B., and Zaveri, R. A.: Black carbon over Mexico: the effect of atmospheric transport on mixing state, mass absorption cross-section, and BC/CO ratios, Atmos. Chem. Phys., 10, 219–237, https://doi.org/10.5194/acp-10-219-2010, 2010.

Taketani, F., Miyakawa, T., Takashima, H., Komazaki, Y., Pan, X., Kanaya, Y., and Inoue, J.: Shipborne observations of atmospheric black carbon aerosol particles over the Arctic Ocean, Bering Sea, and North Pacific Ocean during September 2014, J. Geophys. Res.: Atmos., 121, 1914–1921, https://doi.org/10.1002/2015jd023648, 2016.

Torres, O., Bhartia, P. K., Taha, G., Jethva, H., Das, S., Colarco, P., Krotkov, N., Omar, A., and Ahn, C.: Stratospheric Injection of Massive Smoke Plume From Canadian Boreal Fires in 2017 as Seen by DSCOVR-EPIC, CALIOP, and OMPS-LP Observations, J. Geophys. Res.: Atmos., 125, https://doi.org/10.1029/2020jd032579, 2020.

Virtanen, P., Gommers, R., Oliphant, T. E., Haberland, M., Reddy, T., Cournapeau, D., Burovski, E., Peterson, P., Weckesser, W., Bright, J., Walt, S. J. van der, Brett, M., Wilson, J., Millman, K. J., Mayorov, N., Nelson, A. R. J., Jones, E., Kern, R., Larson, E., Carey, C. J., Polat, İ., Feng, Y., Moore, E. W., VanderPlas, J., Laxalde, D., Perktold, J., Cimrman, R., Henriksen, I., Quintero, E. A., Harris, C. R., Archibald, A. M., Ribeiro, A. H., Pedregosa, F., Mulbregt, P. van, Contributors, S. 1 0, Vijaykumar, A., Bardelli, A. P., Rothberg, A., Hilboll, A., Kloeckner, A., Scopatz, A., Lee, A., Rokem, A., Woods, C. N., Fulton, C., Masson, C., Häggström, C., Fitzgerald, C., Nicholson, D. A., Hagen, D. R., Pasechnik, D. V., Olivetti, E., Martin, E., Wieser, E., Silva, F., Lenders, F., Wilhelm, F., Young, G., Price, G. A., Ingold, G.-L., Allen, G. E., Lee, G. R., Audren, H., Probst, I., Dietrich, J. P., Silterra, J., Webber, J. T., Slavič, J., Nothman, J., Buchner, J., Kulick, J., Schönberger, J. L., Cardoso, J. V. de M., Reimer, J., Harrington, J., Rodríguez, J. L. C., Nunez-Iglesias, J., Kuczynski, J., Tritz, K., Thoma, M., Newville, M., Kümmerer, M., Bolingbroke, M., Tartre, M., Pak, M., Smith, N. J., Nowaczyk, N., Shebanov, N., Pavlyk, O., Brodtkorb, P. A., Lee, P., McGibbon, R. T., Feldbauer, R., Lewis, S., Tygier, S., Sievert, S., Vigna, S., Peterson, S., More, S., et al.: SciPy 1.0: fundamental algorithms for scientific computing in Python, Nat. Methods, 17, 261–272, https://doi.org/10.1038/s41592-019-0686-2, 2020.

Wang, J., Su, H., Wei, C., Zheng, G., Wang, J., Su, T., Li, C., Liu, C., Pleim, J. E., Li, Z., Ding, A., Andreae, M. O., Pöschl, U., and Cheng, Y.: Black-carbon-induced regime transition of boundary layer development strongly amplifies severe haze, One Earth, 6, 751–759, https://doi.org/10.1016/j.oneear.2023.05.010, 2023a.

Wang, J., Wang, J., Cai, R., Liu, C., Jiang, J., Nie, W., Wang, J., Moteki, N., Zaveri, R. A., Huang, X., Ma, N., Chen, G., Wang, Z., Jin, Y., Cai, J., Zhang, Y., Chi, X., Holanda, B. A., Xing, J., Liu, T., Qi, X., Wang, Q., Pöhlker, C., Su, H., Cheng, Y., Wang, S., Hao, J., Andreae, M. O., and Ding, A.: Unified

theoretical framework for black carbon mixing state allows greater accuracy of climate effect estimation, Nat. Commun., 14, 2703, https://doi.org/10.1038/s41467-023-38330-x, 2023b.

Wang, Q., Schwarz, J. P., Cao, J., Gao, R., Fahey, D. W., Hu, T., Huang, R.-J., Han, Y., and Shen, Z.: Black carbon aerosol characterization in a remote area of Qinghai–Tibetan Plateau, western China, Sci. Total Environ., 479, 151–158, https://doi.org/10.1016/j.scitotenv.2014.01.098, 2014a.

Wang, Q., Jacob, D. J., Spackman, J. R., Perring, A. E., Schwarz, J. P., Moteki, N., Marais, E. A., Ge, C., Wang, J., and Barrett, S. R. H.: Global budget and radiative forcing of black carbon aerosol: Constraints from pole-to-pole (HIPPO) observations across the Pacific, J. Geophys. Res.: Atmos., 119, 195–206, https://doi.org/10.1002/2013jd020824, 2014b.

Weiden, S.-L. von der, Drewnick, F., and Borrmann, S.: Particle Loss Calculator – a new software tool for the assessment of the performance of aerosol inlet systems, Atmos. Meas. Tech., 2, 479–494, https://doi.org/10.5194/amt-2-479-2009, 2009.

Yang, Z., Ma, N., Wang, Q., Li, G., Pan, X., Dong, W., Zhu, S., Zhang, S., Gao, W., He, Y., Xie, L., Zhang, Y., Kuhn, U., Xu, W., Kuang, Y., Tao, J., Hong, J., Zhou, G., Sun, Y., Su, H., and Cheng, Y.: Characteristics and source apportionment of black carbon aerosol in the North China Plain, Atmos. Res., 276, 106246, https://doi.org/10.1016/j.atmosres.2022.106246, 2022.

Yu, P., Toon, O. B., Bardeen, C. G., Zhu, Y., Rosenlof, K. H., Portmann, R. W., Thornberry, T. D., Gao, R.-S., Davis, S. M., Wolf, E. T., Gouw, J. de, Peterson, D. A., Fromm, M. D., and Robock, A.: Black carbon lofts wildfire smoke high into the stratosphere to form a persistent plume, Science, 365, 587–590, https://doi.org/10.1126/science.aax1748, 2019.

Yuan, J., Modini, R. L., Zanatta, M., Herber, A. B., Müller, T., Wehner, B., Poulain, L., Tuch, T., Baltensperger, U., and Gysel-Beer, M.: Variability in the mass absorption cross section of black carbon (BC) aerosols is driven by BC internal mixing state at a central European background site (Melpitz, Germany) in winter, Atmos. Chem. Phys., 21, 635–655, https://doi.org/10.5194/acp-21-635-2021, 2020.

Zanatta, M., Laj, P., Gysel, M., Baltensperger, U., Vratolis, S., Eleftheriadis, K., Kondo, Y., Dubuisson, P., Winiarek, V., Kazadzis, S., Tunved, P., and Jacobi, H.-W.: Effects of mixing state on optical and radiative properties of black carbon in the European Arctic, Atmos. Chem. Phys., 18, 14037–14057, https://doi.org/10.5194/acp-18-14037-2018, 2018.

Zhang, R., Khalizov, A. F., Pagels, J., Zhang, D., Xue, H., and McMurry, P. H.: Variability in morphology, hygroscopicity, and optical properties of soot aerosols during atmospheric processing, Proc. Natl. Acad. Sci., 105, 10291–10296, https://doi.org/10.1073/pnas.0804860105, 2008.

Zhang, Y., Zhang, Q., Cheng, Y., Su, H., Kecorius, S., Wang, Z., Wu, Z., Hu, M., Zhu, T., Wiedensohler, A., and He, K.: Measuring the morphology and density of internally mixed black carbon with SP2 and VTDMA: new insight into the absorption enhancement of black carbon in the atmosphere, Atmos. Meas. Tech., 9, 1833–1843, https://doi.org/10.5194/amt-9-1833-2016, 2016.

Zhang, Y., Zhang, Q., Cheng, Y., Su, H., Li, H., Li, M., Zhang, X., Ding, A., and He, K.: Amplification of light absorption of black carbon associated with air pollution, Atmos. Chem. Phys., 18, 9879–9896, https://doi.org/10.5194/acp-18-9879-2018, 2018a.

Zhang, Y., Su, H., Ma, N., Li, G., Kecorius, S., Wang, Z., Hu, M., Zhu, T., He, K., Wiedensohler, A., Zhang, Q., and Cheng, Y.: Sizing of Ambient Particles From a Single-Particle Soot Photometer Measurement to Retrieve Mixing State of Black Carbon at a Regional Site of the North China Plain, J. Geophys. Res.: Atmos., 123, 12,778-12,795, https://doi.org/10.1029/2018jd028810, 2018b.

Zhang, Y., Zhang, Q., Yao, Z., and Li, H.: Particle Size and Mixing State of Freshly Emitted Black Carbon from Different Combustion Sources in China, Environ. Sci. Technol., 54, 7766–7774, https://doi.org/10.1021/acs.est.9b07373, 2020.

Zhang, Y., Su, H., Kecorius, S., Ma, N., Wang, Z., Sun, Y., Zhang, Q., Pöschl, U., Wiedensohler, A., Andreae, M. O., and Cheng, Y.: Extremely low-volatility organic coating leads to underestimation of black carbon climate impact, One Earth, 6, 158–166, https://doi.org/10.1016/j.oneear.2023.01.009, 2023.

Zhang, Y., Wang, J., Wu, N., Ouyang, X., Li, G., Cheng, Y., Zhang, Q., Ding, A., and Su, H.: The Contribution of Black Carbon-Containing Particles to PM2.5: Variability, Drivers, and Impacts, Environ. Sci. Technol., 59, 5155–5163, https://doi.org/10.1021/acs.est.5c00675, 2025.

Curriculum Vitae